Rotary Fast Tool Servo Component Design

by

David Anthony Chargin

Bachelor of Science in Mechanical Engineering
& Materials Science
University of California, Davis (1997)

Submitted to the Department of Mechanical Engineering
in partial fulfillment of the requirements for the degree of

Master of Science in Mechanical Engineering

at the

MASSACHUSETTS INSTITUTE OF TECHNOLOGY

June 1999

Author .....
Department of Mechanical Engineering
May 18, 1999

Certified by .....
David L. Trumper
Associate Professor of Mechanical Engineering
Thesis Supervisor

Accepted by .....
Ain A. Sonin
Chairman, Department Committee on Graduate Students

Rotary Fast Tool Servo Component Design

by

David Anthony Chargin

Submitted to the Department of Mechanical Engineering
on May 18, 1999, in partial fulfillment of the
requirements for the degree of
Master of Science in Mechanical Engineering

Abstract

This thesis covers the design and implementation of the components of a novel rotary fast tool servo (RFTS). The RFTS enables diamond turning of rotationally asymmetric optics, with an emphasis on eyeglass lenses. These components include the rotary arm which supports the cutting tool, a high resolution angular sensor for position feedback, and a labyrinth seal system to protect the rotary axis bearings.

The design of the toolarm meets several conflicting challenges, including maintaining low rotational inertia and high stiffness while providing an integrated tool height adjustment mechanism. A new, novel "double-diaphragm" actuator is developed, which provides sub-micrometer level tool height adjustment. This actuator enables the toolarm to be constructed with little additional material, meeting the low inertia goals without compromising stiffness.

The high resolution angular feedback sensor selected for the machine is a diffractive laser design. It was successfully interfaced into the machine, both mechanically and electrically, to provide $\sim$ 10 nanometer resolution in cutting tool location. This was essential in enabling the RFTS to turn lenses with micrometer accuracy.

Finally, a new possibility of developing rotational damping with a labyrinth bearing seal is explored. Rotational damping is created by exploiting the shear forces developed between a viscous fluid and a labyrinth with a fine gap size. This provides excellent sealing as well as rotational damping.

Thesis Supervisor: David L. Trumper
Title: Associate Professor of Mechanical Engineering

Acknowledgments

Many people have been instrumental in helping me finish this work, and I cannot give them enough thanks. My thesis advisor, Professor David Trumper, has given me the guidance I needed on this project. His seemingly endless knowledge of precision engineering and creative ideas put me on the right track and enriched my MIT experience beyond measure. I am proud to have worked with him. Professor Alex Slocum also contributed his advice on the toolarm, and his enthusiasm for engineering was inspirational.

I have had the good fortune to work with several great students on this project. This diamond turning machine is really Stephen Ludwick's baby, not just his doctoral thesis work, and he deserves all the accolades for it. I never realized how great Pittsburgh was until I worked with Steve. David Ma and Joseph Calzaretta were always ready to lend not just their professional support, but also their friendship.

Several companies graciously donated their time and resources to make this project a success. I am indebted to MicroE for providing the laser diffractive encoder and technical support. DEKA Research & Development did essential wire EDM machine work for the construction of the new toolarm, while Moore Special Tool Co. contributed the surface plate which formed the foundation of the machine.

My fellow members of the Precision Motion Control laboratory provided many stimulating discussions and a great atmosphere in which to work. Michael Liebman, Ming-chih Weng, Robin Ritter, Pradeep Subrahmanyan, and Paul Konkola, thanks for sharing your time with me. I have never worked with a more talented group of people.

The support of the staff of LMP has been excellent. Maureen Lynch and David Rodriguerra are a great asset to the PMC group, and were always ready to help. In the machine shop, Mark Belanger and Gerry Wentworth deserve much credit for helping me with the fabrication of many parts, and for having patience when I broke their equipment! Mark also machined a prototype piece when we needed things done quickly.

I'm not certain I would have attended MIT without the sage advice of Daniel Thompson. Thanks for helping me choose MIT over many competing institutions; I know I made the right choice.

I cannot imagine life at MIT without the support of my friends. Pankaj Lad always had an ear to listen when I needed to vent, and together we trekked accross the greater Cambridge-Somerville area on foot. Poonsaeng "Kung" Visudhiphan has been my most dear and understanding friend, and could always brighten my day with a smile. Thank you both. I'll always cherish the memories.

Finally, I thank my family for their unending love and support. My parents, Tony and Carol, instilled me with the values and provided the direction that make me who I am today. My sister, Emily, was always there with an encouraging pep talk when I needed it the most. I could not have finished this journey without you all.

Contents

List of Figures

List of Tables

Chapter 1

Introduction

1.1 Overview

This work focuses on the design of components for a new, high-performance machine tool for the manufacture of ophthalmic lenses. Under the direction of Professor Trumper, a project to build this machine tool started in January 1996 in the Precision Motion Control Laboratory at MIT. The project centered on creating a machine which would improve upon the standards of accuracy and finish in the generation of a plastic eyeglass lens surface. The improvement in lens quality is great enough that the secondary finishing operations of lens manufacture, such as lapping, can be eliminated.

The enabling technology of this machine tool is the rotary fast tool servo (RFTS). Diamond turning has been a documented technology for producing workpieces of exceptional accuracy and surface finish, but the rotationally asymmetric nature of ophthalmic lenses prevented lens production with this process. The rotational asymmetry of the ophthalmic lens requires a tool to move in and out of the workpiece at a large amplitude with each revolution of the spindle. Conventional linear axis machines do not have the nearly 100 g acceleration required to follow such a toolpath. The RFTS is a new machine configuration which places the diamond tool on the end of a rotary arm. The low inertia of such a configuration allows it to be directly coupled to an actuator for extremely high accelerations which enable rotationally asymmetric

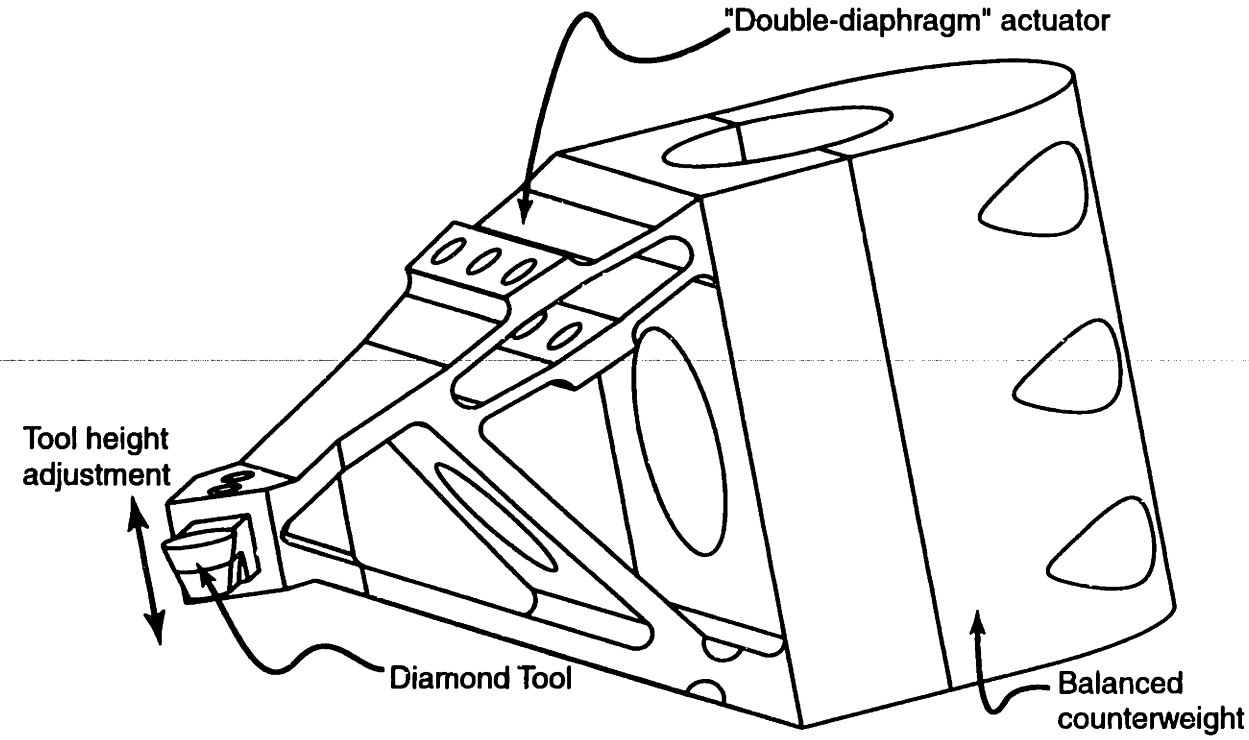

Figure 1-1: "Double-diaphragm" toolarm allows sub-micron tool height adjustment.

cutting.

The RFTS presented many new design challenges, several of which are covered in this thesis. Central to a RFTS is a rotary arm to carry the tool. This arm must be simultaneously of high stiffness and low inertia. Adding to the complexity, however, is the necessity of incorporating a mechanism to adjust the tool height, an essential process in any turning machine. For a machine of this accuracy level, the tool height needs to be adjusted with sub-micrometer-level precision. These conflicting requirements have been met with a novel actuator design, illustrated in Figure 1-1. This arm uses a "double-diaphragm" actuator to provide high stiffness and sub-micron-resolution tool height adjustment while adding little additional mass. This system can also be adapted to provide two back-to-back toolarms, in a "double-ended" configuration. This enables automatic tool changing to occur between a roughing tool and a high-quality finishing tool.

Another component needed for RFTS operation is a high resolution rotary position sensor. The RFTS, unlike conventional cutting machines, does not benefit from a

transmission to reduce the output of its actuator for higher precision. In fact, the rotary arm, which magnifies the acceleration at the tool, also magnifies any error in the motion of the actuator. Thus a rotational measurement system of exceptional resolution is necessary for feedback to the control system, if the desired machine accuracy is to be met. Conventional rotary encoders do not come close to meeting this requirement. A new diffractive laser encoder[18], providing an incredible 63,201,280 counts per revolution, was selected and integrated into the machine.

The final part of this thesis is the design and manufacture of bearing seals. Rotational systems are much easier to seal than linear slides. However, the sequence of machine integration leads to the need for a seal which can be split around the shaft, eliminating many conventional sealing systems. I designed a labyrinth seal to meet this requirement. I also investigated using these seals to add beneficial viscous damping to the rotating system.

Of course the complete machine has been the work of many people. Stephen Ludwick, a Ph.D. candidate, developed the RFTS concept with Prof. Trumper and has made it his Doctoral thesis[12], working on the project since its inception. He has been involved with all aspects of the machine design and construction, but has focused especially on the development of new repetitive control theory which has produced much higher performance from the RFTS system. David Ma completed his Master's thesis[17] in 1998 on the selection of the actuator and bearings for RFTS, as well as on the design of the casting which supports the axis. Joseph Calzaretta, another Ph.D. student, began work in September 1998 on the calibration of the nonconventional RFTS geometry in order to obtain the desired accuracy.

The remainder of this thesis is organized as follows:

- The rest of this chapter details the issues of ophthalmic lens production and provides an overview of the RFTS machine.
- Chapter 2 covers the selection and implementation of the high resolution rotary position sensor.
- Chapter 3 describes the design of the bearing seals for the precision bearings

on the RFTS axis. The intriguing possibility of damping the tool motion with the bearing seals is evaluated.

- Chapter 4 lists the process for the design of the toolarm, and develops the challenging requirements the toolarm must meet in detail.
- Chapter 5 presents a number of conceptual solutions to the toolarm requirements.
- Chapter 6 investigates the "building-block" concepts needed to design the toolarm, so that the conceptual designs can be evaluated and chosen. This chapter presents a good overview of many precision mechanical design techniques.
- Chapter 7 develops several of the conceptual designs. The most promising were prototyped, and then the final arm configuration was chosen and implemented. This chapter captures this evaluation in detail.
- Finally, Chapter 8 presents the conclusions developed over the course of this work.

Note that this thesis focuses on the manufacture of plastic spectacle lenses, which represent the majority of the domestic (United States) market; the difficulties in producing glass lenses are not addressed here.

1.2 Ophthalmic Lenses and Manufacturing

Ophthalmic lenses are designed to correct for error in the lens or cornea of the human eye. For many people, only the focal length of the cornea needs to be corrected, and a spherical lens will suffice. These lenses correct the traditional "near-sightedness" or "far-sightedness" and can be manufactured on a traditional high precision lathe. The more interesting class of errors in the cornea, which lens manufacturers also need to be able to correct, are those which produce *astigmatism.*

A person who suffers from astigmatism has a rotationally asymmetric cornea. The correction for such errors is currently approximated by a toric lens, which has two

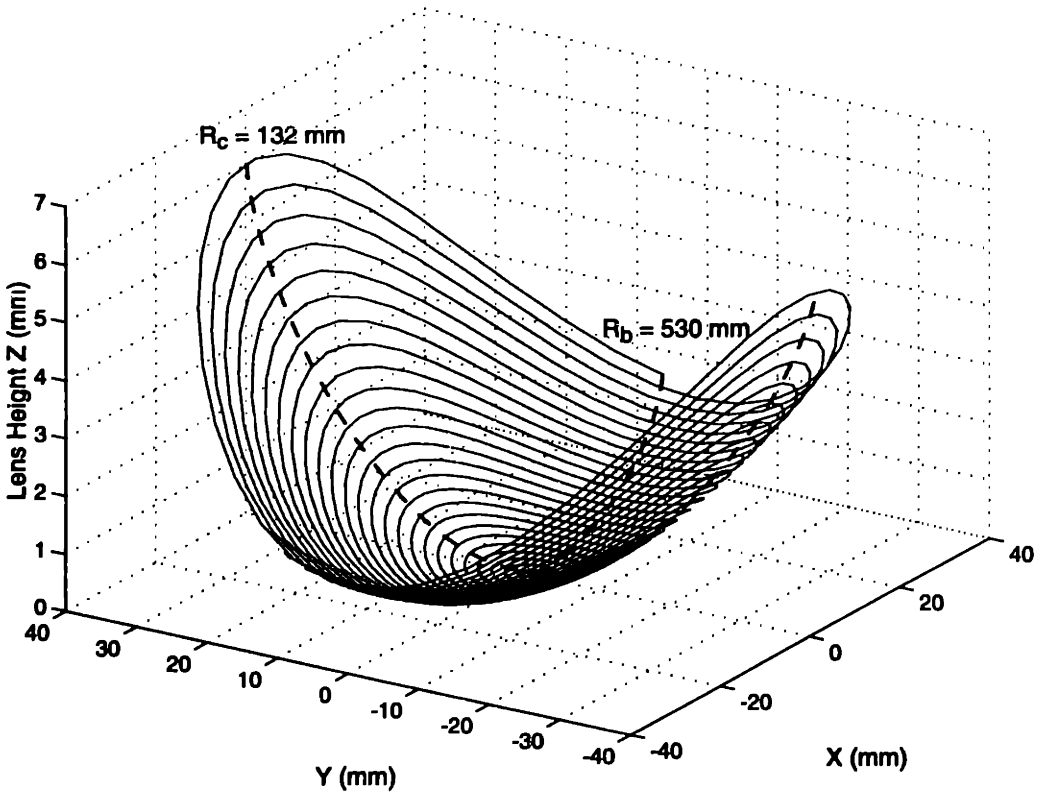

Figure 1-2: Surface of a toric lens. Base curve radius is $R_b = 530$ mm. Cross-curve radius is $R_c = 132$ mm.

radius of curvatures, a large "base curve" radius and a smaller "cross curve" radius. This is illustrated in Figure 1-2. The equation of this surface is then given in Cartesian coordinates by[17]

$$z(x,y) = R_b - \sqrt{[R_b - R_c + \sqrt{(R_c^2 - y^2)}]^2 - x^2} \tag{1.1}$$

where the x,y coordinates form the plane of the lens and z is the height of the lens above this plane, as shown in Figure 1-2. With the radii of curvature typically found in eyeglass lenses, this feature height variation can range to greater than 1 cm peak-to-peak at the periphery of the lens. It is this variation in feature height which prevents the lens from being machined on a conventional lathe, and necessitates fast tool motion. This large amplitude also puts it far outside the range of other fast tool servo systems[12].

The current manufacturing process for these lenses relys on a multi-step process.

First, the surface is roughed out on a "surface generator," a machine which is either a rotating cutter, ball-endmill type milling machine or a turning machine with an inaccurate fast tool servo. In both cases the machine only produces a basic, inaccurate, shape with poor surface finish (relative to the required optical surface). Accuracy is then achieved by an abrasive process, where the lens is lapped against a hard master shape coated with abrasive. Successively finer abrasives allow an optical surface finish to be obtained.

This process has several undesirable properties. First, a hard master lap is required for every lens that needs to be produced. With several thousand possible prescriptions, maintenence and storage of such an inventory of laps is difficult and costly. Even though the laps are much harder than the lenses, they are still subject to wear, and need to be periodically checked for accuracy. Furthermore, the lapping process, as an abrasive material removal method, is inexact. There are only a few relative paths between the lap and lens on which motion can be maintained, and deviation in the movement of the lap can cause errors in the lens. Lapped lenses measured by Ma[17] exhibited errors with magnitudes up to 15-20 μm over the surface. Finally, the lapping process itself is an additional manufacturing operation, which adds to the fabrication cost of a lens.

Lens prescriptions are based on the inverse of the focal length of the lens surface, also known as the lens "power" measured in diopters $\left(\frac{1}{m}\right)$. The total power of a given lens is simply given by the addition of the powers front and back surfaces of the lens, for lenses in which the thickness is thin enough to be neglected. To meet a given prescription, the manufacturer chooses a lens blank with a premolded front surface, available in several different powers. The back surface is then cut and lapped to meet the desired overall prescription for the lens.

The radii which need to be cut on the surface still need to be determined from the optical power. The opthalmic industry developed a standard[1] to determine the radius of curvature using only the desired optical power of the lens. This relationship

[1] ANSI standard Z80.1-1995

is given by

$$R = \frac{530}{P} \tag{1.2}$$

where R is in millimeters and P is the optical power. The standard assumes a given index of refraction, $N = 1.530$, in order to define this relation.

1.3 Prototype Machine

Our new surfacing machine has been designed to produce lenses of such accuracy and surface finish that the secondary lapping process no longer needs to be employed. Instead, the surface may be brought to final optical clarity by either a coating (which often have additional purposes, such as providing shielding against ultraviolet light), or by a conformal polishing process. The conformal polish should remove so little material that a hard master shape is not needed. Instead, this abrasive process simply improves the surface finish, not the lens accuracy, and needs only a shape which adapts to the previously cut surface.

To meet these goals, our machine is designed to perform to the following specifications:

- Cut lens blanks up to 100 mm in diameter and 30 mm thick.
- Form a toric surface described by Equation 1.1.
- Maintain a form accuracy of 1 μm over a 10 mm section of the surface.
- Achieve a surface roughness of $R_q = 0.2$ to 0.3 μm.
- Cut these blanks in less than one minute.

The prototype turning machine is illustrated in cross-section in Figure 1-3. A photograph appears in Figure 1-4. These figures show the nonconventional layout of the machine. The spindle sits on a cross slide axis driven by a linear motor, as in the conventional "T-base" lathe configuration. However, instead of a linear axis

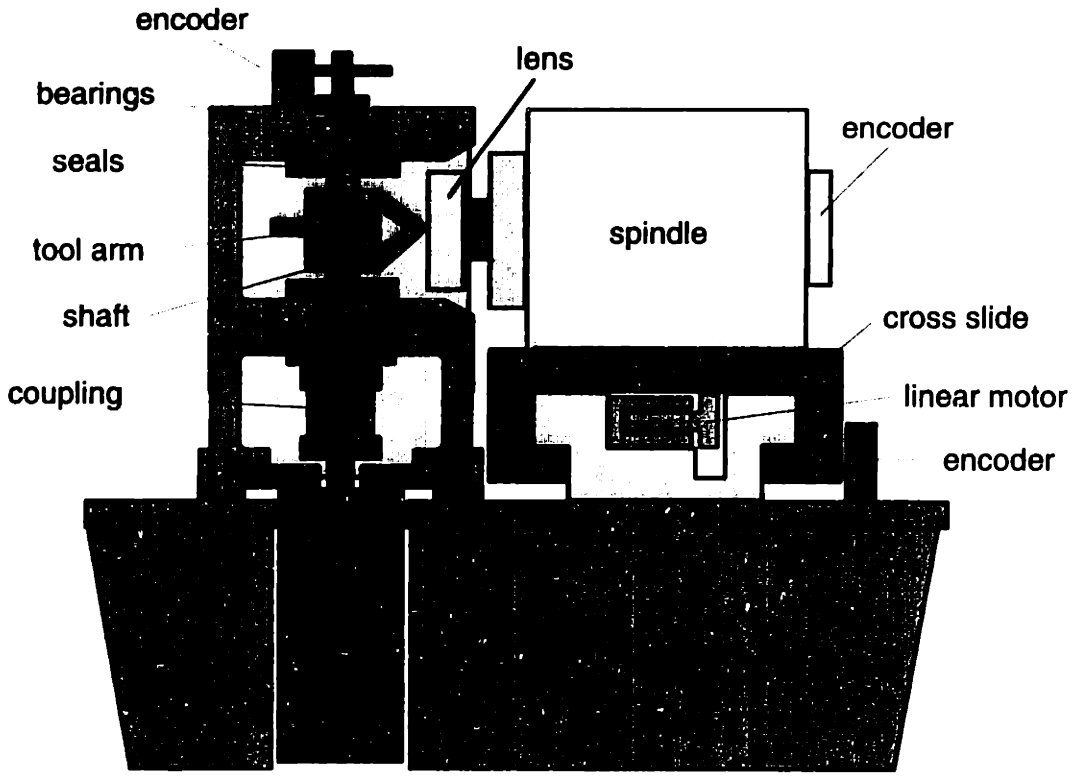

Figure 1-3: Schematic cross-sectional view of the turning machine showing major components. From Ludwick[12]

perpendicular to the cross slide, the tool is carried on a rotary arm; this is the RFTS axis.

The lens blank is chucked into the spindle, which is a Professional Instruments[25] Model 4R "Twin Mount" air-bearing spindle driven by an integral brushless DC motor. This spindle also has a 10000 count encoder to provide the control electronics with the angular position of the lens, as well as enabling control of the spindle speed. This spindle is one of the highest accuracy spindles available, with radial and axial error motions of under 1 μinch ($\sim$ 25 nm). Such accuracy is essential for the direct machining of optical surfaces, since any error motions in the spindle will degrade the surface finish of the workpiece. The cross slide is also an air bearing device, and the linear position is measured with a glass scale encoder that has 0.1 μm resolution.

Most of the development work has centered on the novel RFTS axis. The toolarm rides on a pair of duplex ABEC-9 ball bearings, which are the highest grade rolling element bearing available. These provide precision motion for the tool. The motor is

ratio of the rotary inertias, due to the radius squared present in the rotational inertia formulation (A point mass m at a radius r has a rotational inertia $J = mr^2$). A typical linear system may have a ratio of base to moving element inertia ratio of 10^2:1, while the rotational system here has a rotational inertia ratio of 10^5:1.

Finally, the kinematic motion of the RFTS does provide challenges in generating the toolpath, as detailed by Ludwick[12]. However, despite the coupled motion of the RFTS in X-Y Cartesian space, motion of the RFTS does not require the cross slide to move back and forth. The cross slide can still be a relatively low performance axis, simply maintaining a constant velocity. The high performance RFTS can then be synchronized with cross slide and spindle position, so any error in these axes does not produce an error in the cut lens.

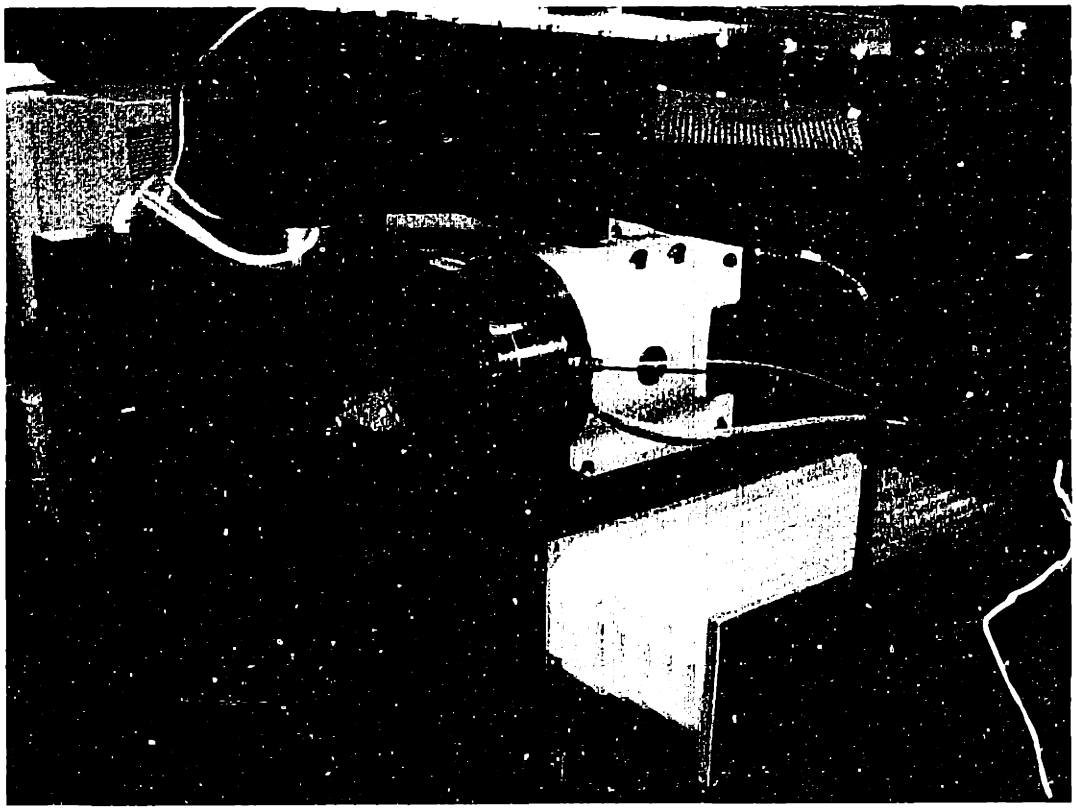

Figure 1-4: Photograph of the prototype lens surfacing machine

connected to the shaft through a torsionally stiff, yet translationally flexible coupling, so that the errors in motor bearings are not transmitted to the shaft. The motor is a brushless DC unit providing 3 horsepower and 9 N-m of continuous torque. Angular position is measured by the encoder at the top of the shaft. The selection and integration of this sensor is documented in detail in this thesis.

Note in particular the large mass of the base relative to the moving RFTS. Not only is the mass large, but is distributed well away from the tool axis, providing more rotational inertia. It is the large rotational inertia of the base relative to the moving axis which helps makes this design so successful. Since the toolarm is designed to be balanced about the center of rotation, only disturbance torques are transmitted to the base. The much greater rotational inertia of the base ensures that the torques which provide great acceleration on the RFTS promote negligible motion on base, minimizing vibration. This is one great advantage of the rotational system; linear tool motion relys simply on the ratio of the masses, which is much smaller than the

Chapter 2

Position Sensor

The RFTS axis requires a position sensor with an angular resolution several orders of magnitude higher than most conventional encoders used for servomotor control. Typical incremental rotary optical encoders only provide a resolution of about 4000 counts/rev, which translates to roughly 126 μm of linear motion at the tool tip in this direct drive machine. Our goal is to have better than 10 nm resolution at the tool tip. We thus need an encoder providing on the order of 50 million counts/rev. This chapter focuses on the selection and implementation of a state of the art high resolution rotary encoder for the RFTS axis to meet this requirement.

2.1 Sensor Requirements

- Angular accuracy of $\sim 10\mu$rad, to provide positioning accuracy of 1 μm.
- Angular resolution one order of magnitude greater than the accuracy, $\sim 1\mu$rad.
- Operating speeds of $\sim$ 350 RPM.
- Low rotational inertia.

The accuracy requirement for the sensor is derived from the specified form error for the production of lenses. To achieve the desired form error of 1 μm over 10 mm the lens surface, an 80 mm long arm requires 12.5 μrad rotational accuracy. Longer arms

require more angular resolution for a given tip position resolution. However, if the sensor does not meet this requirement for intrinsic accuracy, but does have the necessary resolution and repeatability, the sensor may be "error mapped" against a known reference sensor to achieve the desired accuracy. This can, however, considerably increase the effort needed to calibrate the machine.

The resolution requirement is a general "rule of thumb" for any motion control system. By providing a resolution that is one order of magnitude greater than the desired accuracy, smooth transitions can be made across surfaces. This will help decrease the waviness and improve the surface finish of the lens, which are both higher frequency errors than the form error. This resolution is also essential to achieve high position bandwidth in the actuator. High bandwidth control systems may require high gains based on velocity in the control, and often the position signal is differentiated (lead filtered) to attain a velocity feedback term (necessary for damping). The high gain, combined with the inaccuracy and noise of numerical differentiation, can lead to limit-cycling about the position setpoint if the sensor resolution is too coarse.

The velocity limit of any position feedback sensor will be determined by its inherent technology and its interface electronics. Analog devices generally easily meet velocity requirements, since they are essentially only limited by the speed of the sampling device, which is presumably fast enough for the control system (Although note that some sampling devices, while of high accuracy and high bandwidth, have an unacceptably long latency for control purposes. Such devices must be chosen carefully). Only low pass filters, perhaps present to suppress higher frequency noise, could limit the velocity response of an analog position sensor. In contrast, discrete sensors, such as optical encoders, often have more stringent velocity limits. These devices frequently produce incremental electrical pulses as position changes, which need to be accurately counted to determine the correct position. With high resolution devices, high velocity will lead to high data rate, and the consequent possibility of a missed pulse and inaccurate count if the interface electronics are inadequate.

The required rotational velocity limit of the sensor can be estimated from the gradient of the lens surface and the rotational velocity of the spindle. Section 4.3.2

details the derivation of the lens gradient. In that section, I note that the actual lenses that can be cut will be limited by the clearance angle on the tool. Since the clearance angle on the selected tooling is $\theta = 24.5°$, this number can be used to determine the maximum velocity of the tool, which will occur at the outermost edge of the lens blank. The maximum RFTS velocity ω is then given by

$$\omega = \frac{\Omega D \tan\theta}{2L} \tag{2.1}$$

where Ω is the rotational speed of the spindle in rad/sec, D is the diameter of the lens blank in meters, L is the length of the toolarm in meters, and θ is the slope of the lens in radians. For $\Omega = 1200$ RPM, $D = 100$ mm, $L = 80$ mm, and $\theta = 24.5°$, this evaluates to $\omega = 342$ RPM. Thus, while our RFTS axis provides very high acceleration, the rotational velocity is moderate.

In his thesis, Ma [17] cataloged several commercially available sensors, including laser encoders and Inductosyns. These are presented in Table 2.1. Unfortunately, these all seem to be inadequate, with all of them having low maximum speeds, and several having high rotational inertia (which can be roughly inferred from the diameter of the sensor). Ma also describes alternative custom-built sensors, such as rotational capacitive sensors. These are likely to require considerable development to function correctly. Nevertheless, a sensor needs to be chosen to replace the JDK Controls servopotentiometer used on the RFTS testbed (See Ma[17]). This device is essentially a variable resistor with 0.1% linearity. Unfortunately, when sampled with the 16-bit analog-to-digital converter (A/D) present in the control electronics (See Ludwick[12] for details), this provides a resolution of only ~ 100 μrad. Sensor noise of about 7 counts limits this further (The 16-bit sample provides 65536 counts/rev). The resolution could be improved by adjusting the reference voltages so that the full scale range of the A/D is a more limited angle, and thus allowing each bit to represent a smaller portion of the angle. However, this device may still not meet the desired resolution of the system, since it relys on a "wiper" riding on the resistive material. Such a wiper is subject to deflection and "stick-slip" effects from friction

Manufacturer: Product	Diameter (mm)	Resolution (μrad)	Max. Speed (RPM)	Cost ($)
MicroE: R5TW16	37	0.04	289	3000
Heidenhain: RON 800	200	0.89	67	5900
HP: E1710A	NA	0.016	212	5346
Canon: X-1M	36	7	180	19000
Farrand: Inductosyn	300	5	360	7000

Table 2.1: High resolution rotary measurement devices from Ma[17]. All are laser encoders, except the last, which uses "Inductosyn" technology.

with the surface, limiting its effective resolution. It is also subject to wear and thus unacceptable in a production environment.

2.2 MicroE Laser Diffractive Encoder

Conventional optical encoders are limited in resolution for a given size, because as the scale lines decrease in width, diffraction effects increase and prevent accurate reading of the signal. Laser diffractive encoders, in contrast, exploit this effect to increase the resolution of the sensor, and are increasingly being used for high resolution position feedback. These devices use a collimated laser beam which is passed through a diffraction grating to stationary photosensors. The photosensors are positioned to receive the first order interference patterns from the grating. The grating is mounted to the object to be measured, and as the relative position of the grating and photosensors changes, the intensity of the interference patterns at the photosensors changes. This technology can be applied to both rotational and linear position measurement systems. Slocum[29] examines rotational devices in detail, and derives the intensity of the interference pattern from the first-order waves as

$$I(\theta) = 2[1 + \cos(2N\theta)] \tag{2.2}$$

where θ is the angular position and N is the number of slits in the rotational grating. Thus one rotation of the grating will generate $2N$ cycles of a cosine signal. Optical means can be use to generate a sine signal 90° out of phase with this signal, and

then angular position can be determined by counting signal cycles and examining the phase relationship of the signals to determine the direction of motion.

MicroE, Inc.[18], a manufacturer of linear and rotational laser diffractive encoders, graciously offered to donate an encoder system for this machine, and we were fortunate for their support. MicroE provides gratings, sensors, and signal processing electronics for a complete position measurement system. After examining their product offerings, their DSP Interpolator card was selected for the interface electronics. This board provides a dedicated DSP for the position sensor. Two A/D converters sample the sine and cosine signals. The DSP then counts cycles of the cosine signals, and uses the A/D converters to interpolate or sub-resolve the signal to provide $\times 4096$ more counts. Interpolation is achieved by examining the magnitudes of the sine and cosine signals, which will determine how far a given cycle has progressed. There are several possible algorithms for implementing this, including a simple arctangent function, but note that where the cosine wave has poor interpolation resolution (in the vicinity of $0, 2\pi, \ldots$, where the signal slope is small), the sine wave has high resolution, and vice versa. The DSP calculates the interpolated position from the sampled data, and then outputs the position as a 32 bit word. The 20 most significant bits (MSBs) represent optical cycle counting, and the 12 least significant bits (LSBs) represent the interpolated data.

An appropriate sensor and encoder grating can be selected by attempting to match the available products with the velocity and resolution requirements. It soon becomes apparent that with the MicroE gratings, the resolution requirement is easily met, but the velocity requirement is more difficult. MicroE rates the DSP interpolation board at 200,000 $\frac{\text{cycles}}{\text{sec}}$ of cycle counting. The accuracy of the interpolated values may decrease before this limit, due to the low-pass filtering of the signal for the interpolation electronics, but the accuracy should be restored once the velocity is lowered. The velocity limit for a given grating is then simply this cycle rate divided by the number of cycles per revolution, or

$$\omega_{max} = \frac{1}{2} R_{max} \frac{p}{\pi d} \tag{2.3}$$

where R_{max} is the maximum rate of cycle counting, p is the pitch of the grating, and d is the optical diameter of the grating. Note there are 2 optical cycles for each line on the grating, hence the multiplication factor. For example, the standard R5TW16 grating delivered by MicroE has a 5 μm grating pitch and a 33 mm optical diameter, allowing a maximum rotational speed of 289 RPM, slower than the maximum velocity the RFTS may attain. The resolution requirement is easily met with this grating, however, since the 41,470 $\frac{cts}{rev}$, combined with the $\times$4096 interpolation, yields a 0.04 μrad angular resolution, or the equivalent of about 3 nm resolution at the tip of an 80 mm arm.

Finding an appropriate grating was somewhat problematic, because most of the MicroE line is based on 5 μm pitch gratings. Larger diameter gratings than the R5TW16 do not meet the velocity requirement. Smaller gratings are difficult to mount mechanically to the shaft, although they are not beyond possibility. The solution lies in the limited line of larger pitch gratings produced by MicroE, which have a 20 μm grating pitch. This will allow the lines per revolution to be reduced, increasing the velocity limit of the encoder. The 20T25 grating has a 49.12 mm optical diameter, which provides a 778 RPM velocity limit, well exceeding our velocity requirement. Although the fundamental resolution provided by the 15,430 $\frac{cts}{rev}$ seems rather coarse for this application, the $\times$4096 interpolation increases this to 63,201,280 $\frac{cts}{rev}$, providing an angular resolution of 0.1 μrad, which meets the angular resolution requirement and gives a tip position resolution of 8 nm. MicroE does not specify the accuracy of this particular encoder, but error mapping should function well if testing demonstrates an encoder related accuracy problem. Relying heavily on the interpolation for the desired resolution also raises the possibility of reduced accuracy at higher velocities, as noted above, but this could again be error mapped.

2.3 Mechanical Interface

MicroE supplies the 20T25 grating on a glass disk, with a thickness of 0.090 in., a 1.000 in. inner hole, and an outer diameter of 1.934 in. This disk must be mounted

to the toolshaft securely, so that there is no movement or slipping of the disk under high rotational accelerations. Yet the mounting method must be compliant enough to avoid crushing and failure of the brittle glass substrate which supports the grating. In addition, the grating must be accurately centered in the axis of rotation of the toolshaft, in order to accurately measure the angular rotation.

The effect of misalignment between the center of the grating and the axis of rotation is illustrated in Figure 2-1. The misalignment shifts the position of a feature at a given radius on the disk in a sinusoidal fashion, reaching its maximum value at the greatest deviation perpendicular to the desired radial orientation[19]. This results in an angular error of the feature reaching

$$\theta_{max} = \arcsin\left(\frac{d}{R}\right) \tag{2.4}$$

where d is the radial deviation of the center axis and R is the radius of the feature. Since the available centering methods, described below, are likely to only center the disk to within 5 μm, the angular error could be as high as 200 μrad! This effect could be alleviated somewhat without detailed error mapping, by determining the two points of maximum error. The toolarm could then be mounted so the operating point is roughly oriented with one of these points. Although the toolarm would then be operating in the region of maximum error, if it is calibrated at this point, the variation at small angular changes actually produces the least error, as it is operating at the peak of a sinusoid. Ma[17] noted 0.8 μm of radial error motion in the RFTS axis due to error motion in the bearings, which was also a once per revolution error. This could cause 30 μrad of angular error by itself; it seems unlikely, but not impossible, that both errors would be in phase. In either case, note that although this maximum angular error exceeds the specifications for the machine, it may not be a problem given the limited angular travel of the RFTS noted earlier. If the toolarm operates at $\pm 20^\circ$ around the point of maximum error, the differential error is only 3 μrad! Note that Equation 2.4 only strictly applies to a point on the disk, and how this translates into actual error is uncertain without more in-depth knowledge of how the encoder

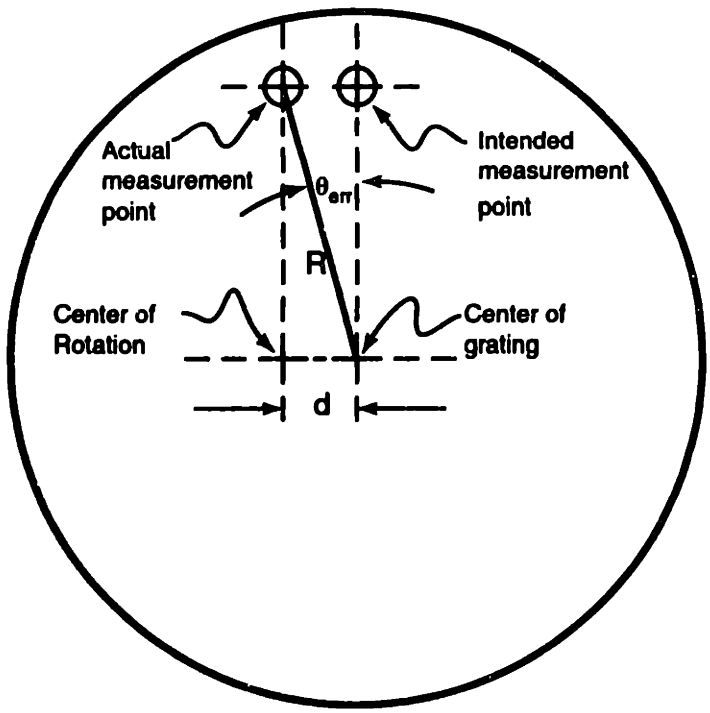

Figure 2-1: Measurement error from centering misalignment.

generates its signals. MicroE claims that the alignment tolerances of their encoders are "an order of magnitude more relaxed" than competing technologies. Equation 2.4 should provide a good estimate of the maximum error. This topic bears further research before undertaking the design of a second generation machine.

The large inner diameter of the 20T25 grating makes integration with the toolshaft easier. To mount the grating, I designed a mild steel "hat" which is mounted on the end of the toolshaft, as illustrated in Figure 2-2. The hat is secured to the toolshaft by a slight interference fit with shaft, as well as with a #10-32 clamping screw through the end of the shaft. This screw also eases assembly, since the hat can be pulled over the interference without the need of a press. A separate mounting piece is necessary, rather than directly machining the end of the shaft, because the required support diameter would be larger than the inner diameter of the bearings which also need to be pressed over the shaft. If disassembly is necessary, that can also be easily accomplished with a $\frac{1}{4}$-20 "jacking" screw. The hole for the clamping screw has a $\frac{1}{4}$-20 thread, which not only allows the #10-32 screw to pass through easily and provide clamping force, but allows a larger $\frac{1}{4}$-20 screw to engage the thread, then push the hat

Angular Error from 5 µm Radial Misalignment	
Optical Diameter of Encoder (mm)	Angular Error (µrad)
20	500
25	400
30	333
35	286
40	250
45	222
50	200
55	182
60	167
65	154

Angular Error in 50 mm Diameter Encoder	
Radial Misalignment Error (µm)	Angular Error (µrad)
1	40
2	80
3	120
4	160
5	200
6	240
7	280
8	320
9	360
10	400

Table 2.2: Estimate of measurement error from centering misalignment. Approximation based on shifting of points on disk, independent of measurement device.

off the end of the shaft. During unmounting, a $\frac{3}{16}$ in. diameter ball can be dropped in the hole to prevent the $\frac{1}{4}$-20 screw from marring the #10-32 threads in the shaft.

The mounting surface of the grating needs the best possible orthogonality with the shaft axis. Machining the inner shaft mounting surface and the grating mounting surface in the same lathe setup helps achieve this goal. After machining, the mounting surface was stoned with Professional Instruments[25] precision flatstones. This improved the surface finish, and removed any raised burrs which could cause high local stresses and fracture of the grating disk. The edge where the mounting surface meets the cylindrical surface of the hat was also undercut, to prevent the grating from resting on the radius formed by the edge of the cutting tool.

The grating needs to be clamped to the mounting surface with a compliant force bearing device. A stiff steel clamp, for instance, is unlikely to be successful, as any less than perfect alignment between the clamp and mounting surface will lead to high local stresses and fracture of the glass disk. A more compliant restraint is necessary. In this case, a plastic end cap was mounted on the hat to press the against the disk through a compliant rubber gasket. Three #4-40 screws provide force to the plastic cap. The presence of the rubber gasket is less than ideal, since it could allow the shifting of the disk from the center position over time. To prevent this, a circumferential groove was machined into the mounting surface. Epoxy can be injected into this grove with a

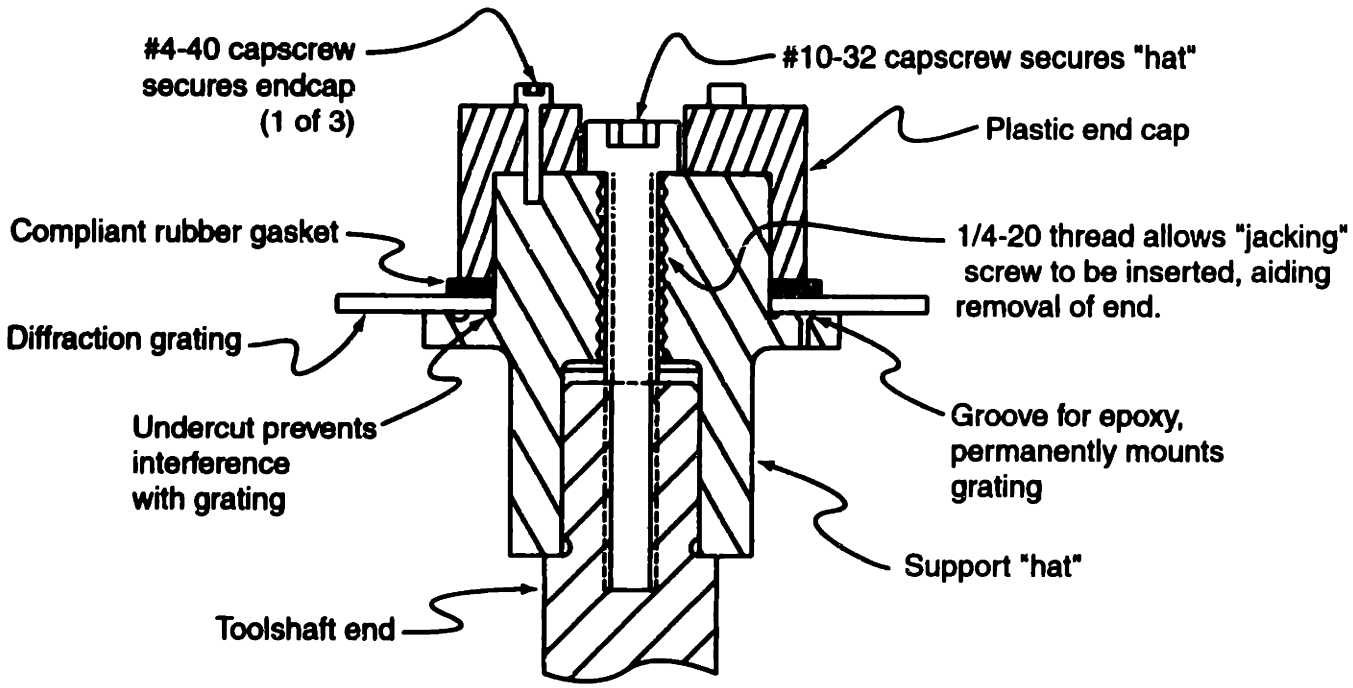

Figure 2-2: Cross-section of the mechanical mounting of the diffraction grating. Important features include the smooth mounting surface perpendicular to the rotation axis, and a compliant clamping mechanism.

syringe through three small holes in the mounting plate. This will secure the position of the grating for long term use, but it has not been done at this time. Even without the epoxy, this mounting method has proven to be stable.

Centering of the disk was accomplished by examining the grating with a 100× Bausch & Lomb stereomicroscope, using reflected light. The actual centering of the grating can then be determined optically, independent of how the grating is centered on the glass disk substrate. A micrometer was used to "bump" the disk into the correct position, by noting the runout of the grating as the shaft was spun on its bearings. Unfortunately, the rubber gasket made this somewhat difficult, since the grating was adjusted under a slight preload from the cap. The gasket allowed the grating to move elastically in many cases, so that the grating would return to its original position. If the preload was removed completely, however, the grating would shift when the cap was tightened to secure the grating. The preload minimized this problem. Eventually, the grating was centered to a runout of < 10 μm. As this is based on the diameter of the grating, this corresponds to a radial error of < 5 μm.

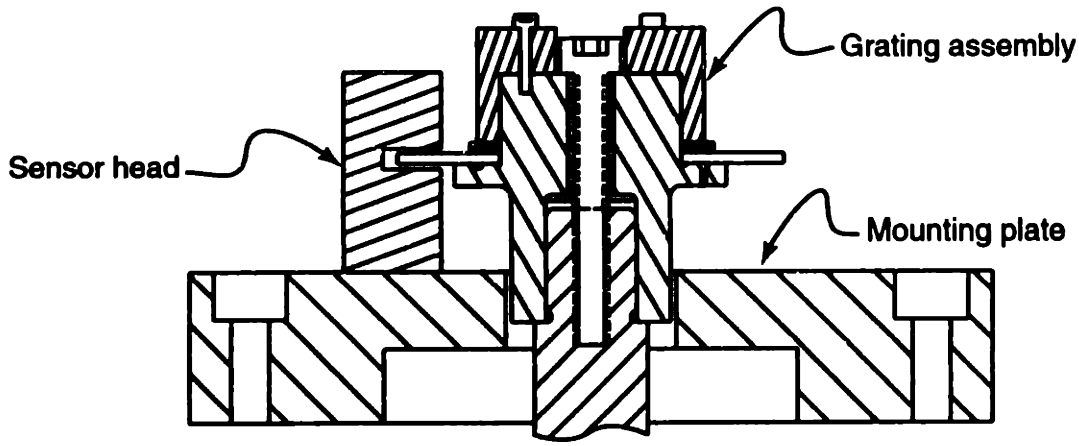

Figure 2-3: Cross-section of encoder and sensor.

Further improvement was limited by the resolving power of the microscope.

The sensor also needs to be aligned with the grating. A mounting plate was fabricated with mounting holes to locate the sensor in the correct location, which is secured with two #2-56 screws. Final alignment of the sensor is performed by sliding it around until the largest magnitude sine and cosine signals are obtained, which can be observed with an oscilloscope at one of the interface boards provided by MicroE. Once the strongest position is secured, the interface board provides potentiometers to adjust the sine and cosine signals to equal magnitude and offset. A diagram and photo of the mounted encoder are shown in Figures 2-3 and 2-4

2.4 Electronic Interface

The position sensor also needs to be interfaced electronically to the control system for it to be useful. The control system hardware is well documented by Ludwick[12]. Real time control calculations are performed by a Tiger31/IP digital signal processing board by DSP Research[7], which utilizes a 48 MHz Texas Instruments C31 processor. This board is mounted in a 486/DX2 PC host computer, which handles non-time critical tasks, including the graphical user interface and toolpath generation. External signals can then be interfaced to the DSP by four *Industry Pack* slots on the Tiger31/IP board. One interface card is mounted in each slot, including one 4 channel analog to digital interface, one 4 channel digital to analog interface, one 4 channel

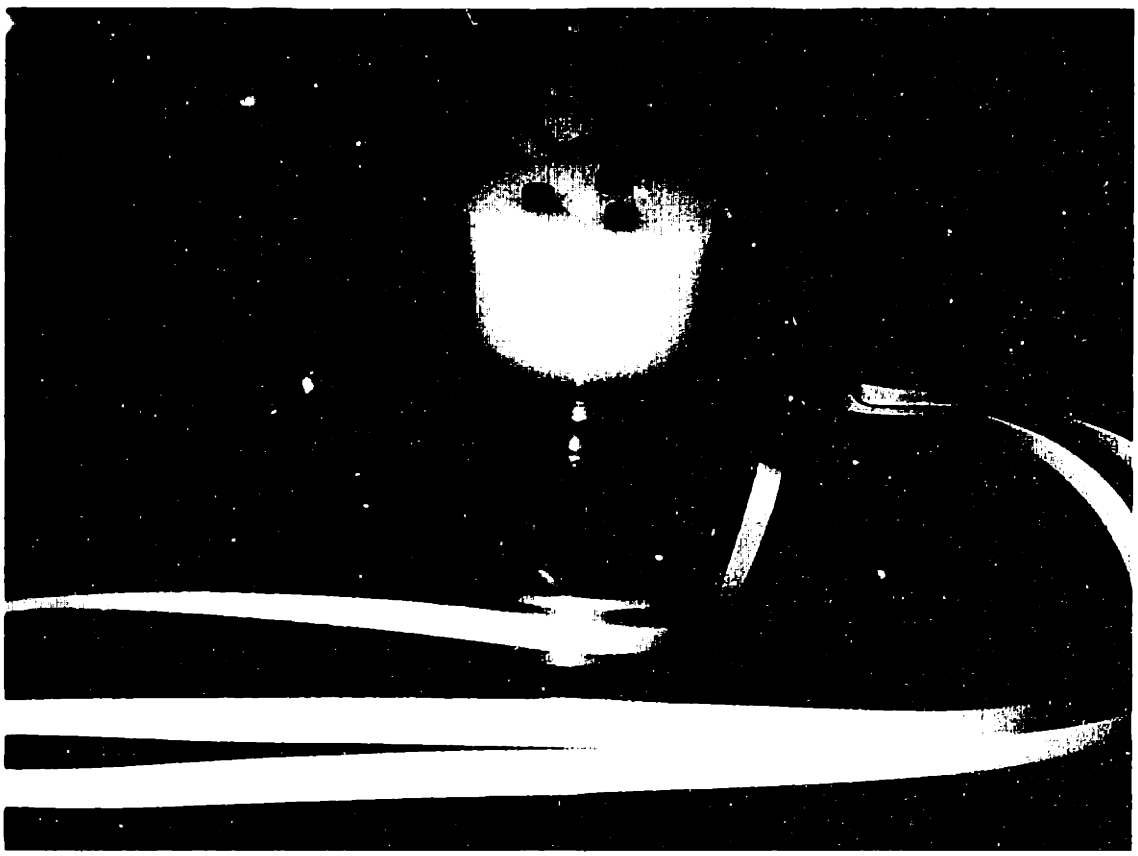

Figure 2-4: Photograph of the mounted encoder assembly

quadrature encoder card, and one 24 channel digital input-output(I/O) interface.

The MicroE DSP Interpolator board outputs the encoder position with a 32 bit word. Unfortunately, only 24 channels of digital I/O are available on our Tiger 31 control DSP, and some of these need to be used for hardware handshaking purposes. One strategy would be to use only several LSBs of the output word, so that maximum resolution could be obtained while limiting the maximum travel. However, even if 22 LSBs were used, the travel would be restricted to $\sim 24°$; such is the resolution of this encoder! Instead, an interface board was constructed to multiplex the encoder output into two 16 bit words.

Multiplexing multiple signals is central to the idea of the "bus" systems found in most computers, which enable several devices to be connected through one interface. Instead of having dedicated wires for each device, all devices share the same connection. In this bus system, all devices may receive data over the bus, but only one device may assert data or signals to the bus. Control logic must specify which device is allowed to assert data. Since bus systems are so widely used, and 32 bit and 16 bit data structures are so common, it was hoped that one or two integrated circuits (ICs) could be used to interface the encoder. However, searches of product catalogs, application guides, and Internet-based databases failed to reveal any such IC's. The common multiplexing ICs are often analog and used to switch several signals into one input; for instance, to multiplex several different channels to one analog to digital converter. Multibit digital multiplexers did not seem to be available, and are likely built into the application specific integrated circuits of most computer components. Instead, a bus system was developed from discrete ICs.

Three-state logic is often used to develop bus systems[11]. In fact, this logic was first developed by National Semiconductor Corporation for this purpose, and was trademarked by them under the TRI-STATE name. With three-state logic, there are not three output voltages, but rather a third output state, that of an open circuit. A three-state logic device typically has an *enable* input, which determines whether the outputs of the device produce active high or low signals, or instead are disconnected from the circuit. Many devices, including logic gates, counters, registers,

etc., are available with three-state outputs. These devices are very useful for building electronic bus systems, since when disabled, they allow another device to drive the circuit.

To interface the DSP Interpolator board to the Tiger31/IP, simply regard 16 digital inputs on the Tiger board as an interface bus. The 16 MSBs and 16 LSBs can then be selected to be read over the bus. Three-state buffers or transceivers can be used to determine which 16 bits of the input are read. Buffer IC's simply take the input data and replicate it on their output pins, unless the outputs are not enabled, in which case their outputs are tied to open circuits. Transceiver ICs are similar, except the data can be transmitted in both directions; that is, they do not have dedicated inputs and outputs, but instead can take the data on bus A and output it on bus B, or vice-versa, depending on the state of another input pin. In this case, only one direction would be used.

The MC74HCT245 Octal three-state bus transceiver was chosen as the bus management IC. These chips are from the "HCT" family of devices, which are CMOS (Complementary Metal-Oxide-Semiconductor) integrated circuits. However, the logic threshold on the HCT family is designed to be lower, at the same level as the TTL (Transistor-Transistor Logic) signal standard. This enables the HCT family to maintain maximum compatibility with other devices, so that either TTL or CMOS signals could be used. This does compromise some noise immunity, however, since the higher logic threshold of pure CMOS filters out some noise. These devices also have a fast switching speed, so that little delay will be needed on the control DSP in order to read each word.

As each MC74HCT245 device handles 8 bits, 4 are needed for the 32 bit output word of the DSP Interpolator. These are wired in pairs, so that either the 16 MSBs are read or the 16 LSBs. The 16 bit word to be read is selected through one of the 8 remaining digital I/O ports, with an inverted signal being sent to one pair. Care should be taken, however, to prevent the bus transceivers from trying to assert data at the same time, resulting in "bus contention". Simple inversion of the signal could lead to such a condition, as there is some propagation delay through the inverter. While

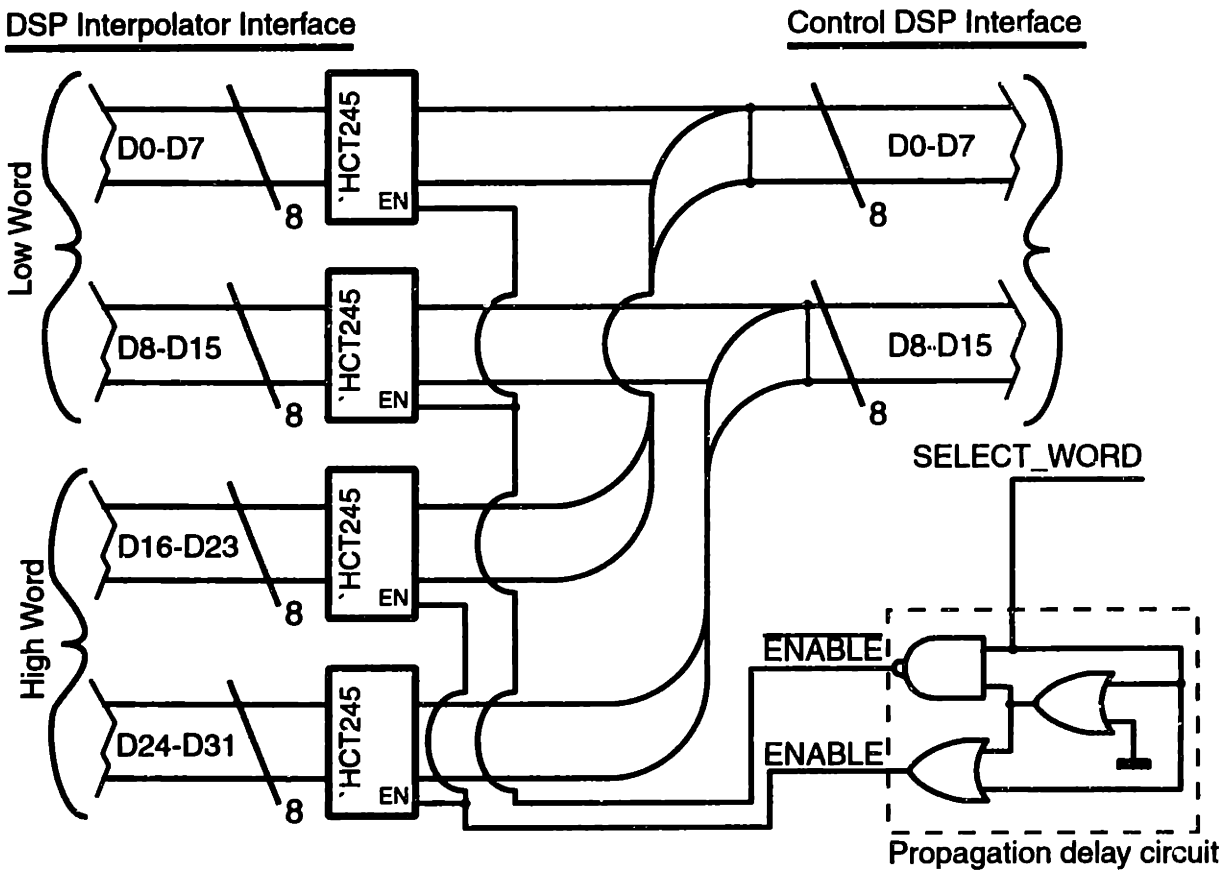

Figure 2-5: Schematic of interface circuit. SELECT_WORD determines if the 16 MSBs or 16LSBs are read, by enabling the three-state logic on the appropriate ICs.

the time period of this interference is very short, on the order of tens of nanoseconds, and is unlikely to exist by the time the data is actually read on the lines, there is no reason to allow it if it can be avoided in the design. A schematic of the circuit is shown in Figure 2-5.

The circuit in Figure 2-6 was designed to prevent any bus contention. Examining a truth table of the logic, it would appear that the circuit really does not do anything more than provide an inverted signal, which could be provided by a simple inverting gate. However, this circuit utilizes the propagation delay of the devices to prevent the ENABLE and $\overline{\text{ENABLE}}$ signals from being active simultaneously. The SN74LS32 OR gates used have a propagation delay of 14 ns, while the SN74LS00 NAND gates have a propagation delay of 9 ns[20]. Figure 2-7 illustrates the actual signals produced by the circuit.

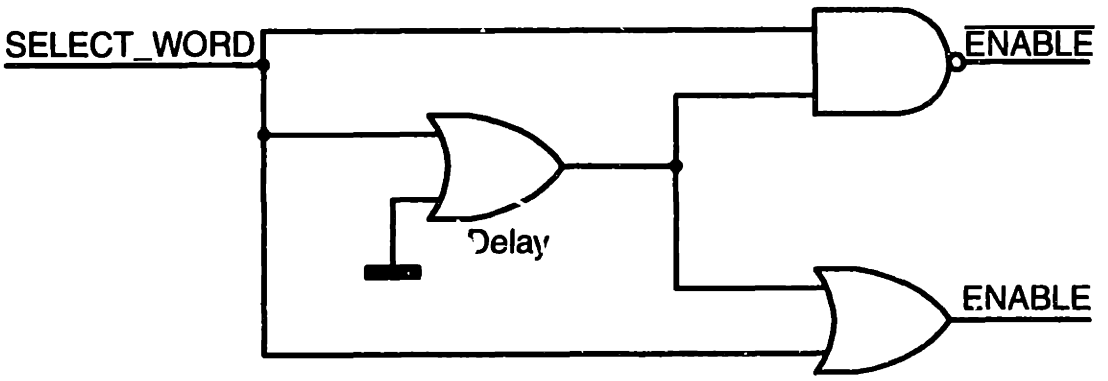

Figure 2-6: Circuit relys on propagation delay to prevent simultaneous activity on the bus. See signal diagram, Figure 2-7

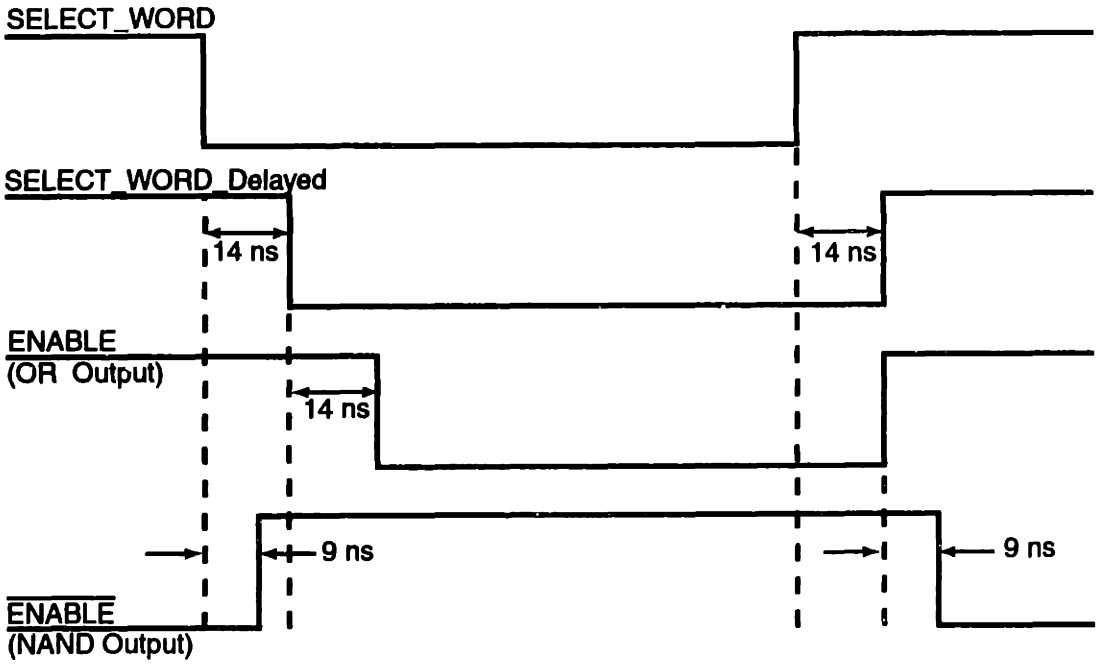

Figure 2-7: Signals from propagation delay circuit. ENABLE and $\overline{\text{ENABLE}}$ are not simultaneously active. Note LOW state is enabled.

Several other signals on the DSP Interpolator should also be interfaced with the control DSP. An error signal is provided, to indicate any possible problems with the DSP Interpolator or encoder, and should be read by the control DSP. The "ENABLE" input (On the DSP Interpolator, not the bus interface ICs) was hardwired to activate the encoder, while the "SYSTEM-RESET" input was wired to a digital I/O for control by the main DSP. A "HOLD" input is provided on the Interpolator, which prevents the values on the output from changing while the output word is read (the position is still updated internally, however.) This input should be set before and released after the output word is read, to ensure the stability of the signals being read. A "RESET" function is also provided to initialize the internal position to zero.

The RESET function of the DSP Interpolator is important because the 20T25 grating, unlike many conventional encoders, does *not* include an index pulse. Thus some other means is needed to determine an absolute reference for the encoder. The precision and repeatability of this reference is also important, as this will determine if the calibrated positions for the tool axis can be maintained after a power cycle. The Aerotech BM1400 brushless DC motor[1], which drives the RFTS, came equipped with a 1000 line encoder which is unused by our controller (The motor is commutated by the amplifier using Hall-effect sensors). This encoder does have an index pulse, which is used for the reference. The index pulse has a fast, nanosecond order rise time, which helps make for a repeatable initialization. The repeatability of the initiation of this pulse with position, however, is more uncertain. Initial tests, where the arm is rotated to touch a fixed reference, seem to indicate that it does provide sub-micron repeatability.

The index pulse of the Aerotech encoder is powered by a different power supply than the rest of the interface electronics, and travels through many feet of wire to reach the interface. This could lead to problems with electrical noise or ground loops being formed if the pulse is directly wired into the interface circuit. To avoid these problems, this signal is coupled to the interface with an HP-2201 optocoupler. This device contains a tiny light emitting diode and detector, which forms an optical coupling to the interface. Since the index pulse and interface are electrically isolated,

no ground loop currents or noise can be passed to the rest of the interface electronics.

The isolated index pulse should still not be directly connected to the RESET input on the DSP Interpolator, however. If there is any repeatability problem with the index, direct connection could be disastrous if the motor operates about that location, since the encoder would report sudden positional changes which do not actually occur. Instead, the index pulse is connected to one input of an AND gate (formed by two NAND gates from the SN74LS00 chip), while the other input is connected to a digital I/O line from the control DSP. The AND output is connected to the RESET input on the DSP Interpolator. In this fashion, the control DSP can perform a RESET-Enable function, so that the MicroE encoder position is only initialized when the control DSP enables the reset, and the index pulse from the Aerotech encoder is received.

Implementation of the actual circuits proved more problematic than the design. Initial construction went quite well. The circuits were made by mounting Wire-Wrap (a registered trademark of Gardner-Denver) type IC sockets and ribbon cable connectors on a 4.5×6.0 in. piece of gridded perfboard. Instead of soldering, Wire-Wrap connections are made by wrapping an inch of bare wire around each connecting post, which are ~ 0.6 in. long. Kynar insulated, 30 gauge wire was used. This type of connection enables many connections to be made more quickly than soldering. Discrete components, such as decoupling capacitors and resistors (needed for the optoisolator) are soldered to pins which have a Wire-Wrap post projecting through the board. It is important to wire-wrap to these posts, and not directly to the components, because the posts have a square cross-section. Secure connections are formed when the wire is drawn tightly around these corners, forming many gas-tight cold welds[11]. Figures 2-8 and 2-9 show the top and bottom surfaces of the interface board, respectively.

Despite the correct assembly of the circuits *as described*, the interface board did not function properly. Performance was extremely erratic. Rotating the tool axis by hand, the control DSP would ocassionally read an incrementing position value; but more often, the DSP Interpolator would appear to "lock up" and deliver a fixed

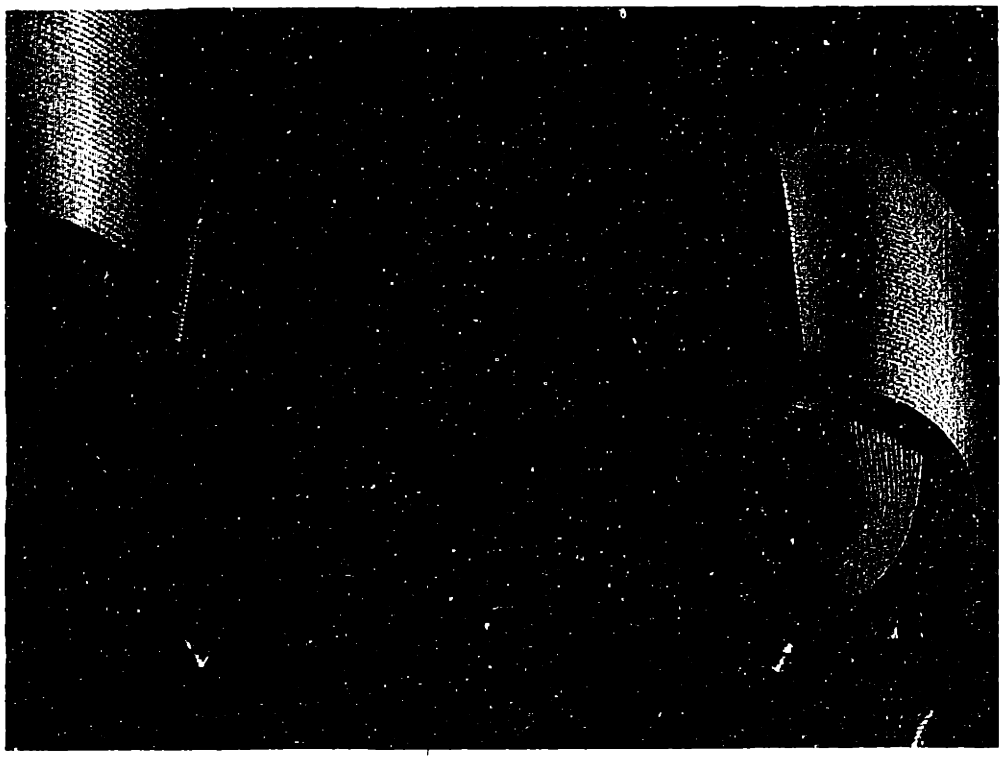

Figure 2-8: Top surface of interface board. MC74HCT245 bus interface ICs are shown in the back, with control logic in the front.

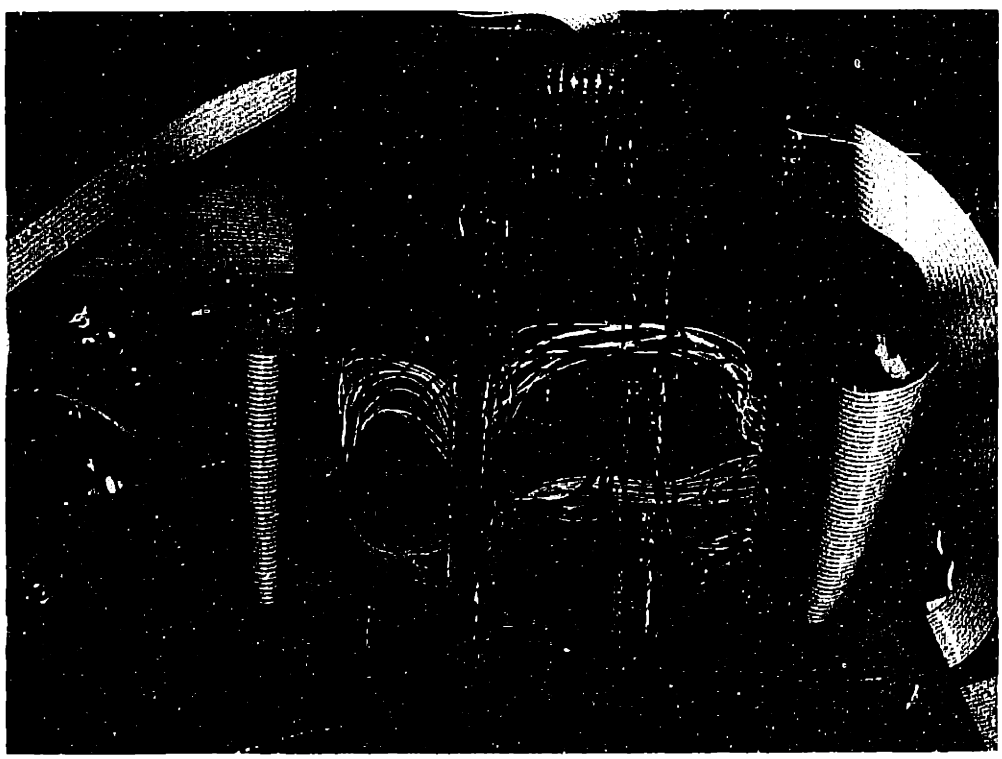

Figure 2-9: Underside of interface board. Wire-Wrap connections are visible.

output. Testing revealed that the DSP Interpolator functioned perfectly when it was disconnected from the interface, but malfunctioned when connected.

This frustrating problem was traced to spurious signals on the SYSTEM-RESET input to the DSP Interpolator. Such signals continuously reset the board, leading to the "locked up" state. But where would such signals originate? The SYSTEM-RESET input was nominally under control from a digital I/O port, but when the DSP Interpolator is activated, it should be held to the ground value. Further testing revealed that the spurious signals were present on all of the ground pins, a condition known as "ground bounce."

There is a tendency when building circuits for designers to consider the ground as an absolute reference through which any amount of current may pass. In reality, the implementation of the ground is subject to the same laws of physics as any other electrical device. "Ground bounce" can be seen in power electronics, when large currents are returned through a length of wire to the source. The voltage at one end of the "ground" wire will be different than at the other, due to the voltage drop of a large current passing through the small, but measurable, resistance of the wire as well as the stray inductance of the connection.

Digital logic IC's do not require large currents, so the current magnitude is not a problem. The frequency, however, often can be. The high switching speeds of digital circuits can demand high frequency currents from the power and ground lines, since the circuits require a pulse of current to change state. The inductance of a current source and sink then become an issue, since the inductance will resist high frequency currents. It is for this reason that "decoupling" capacitors, usually of 0.1 μF, are placed across the power terminals of an IC. The capacitors provide a local source of energy to minimize the demands on the power and ground lines.

Although every IC on the interface board was decoupled with a 0.1 μF capacitor, and an additional 33 μF electrolytic capacitor was placed at the across the supply terminals on the board, this proved inadequate for the high frequency switched currents. The best circuit board design uses a ground "plane" across one entire side of the board. The large flat area of the plane makes an extremely low inductance

connection to any point where it is tapped. Alternately, ground connections can be made to a large, flat conductors placed around the board (See EDN[8], for a more detailed discussion of this effect and solutions). Unfortunately, neither of these design guidelines was followed, resulting in the malfunction of the board. The long, 30 gauge Kynar ground wires were insufficient to the task of carrying the high frequency currents.

In hindsight, this condition might have been recognized sooner by examining the nature of the malfunctions. At one point, the encoder would operate reliably when the position was a positive integer, but "lock up" when the position scrolled to a negative number. With the "2's complement" representation of signed integers used by the DSP Interpolator, the change from zero to negative one corresponds to a binary change from 32 zeros to 32 ones; the maximum possible number of state changes, and hence the change from minimum to maximum current. This led to the "ground bounce" which reset the board, as the high impedance of the ground wires led to a voltage rise at the ground connections when the fast change in current was demanded. Since the output of the digital I/O wired to the SYSTEM-RESET input was connected to ground, this voltage rise was seen by the DSP Interpolator.

Solving this problem, once identified, was not difficult, and the board was not reconstructed. Instead, wires were connected between every ground point on the interface board, creating a grid of wires on the bottom of the board. This ground grid can be nearly as effective as a solid plane, with closer spacing of the grid points providing better protection[8]. In this board, simply connecting all of the ground points together, with the same 30 gauge Kynar wire, proved effective enough at reducing the inductance of the ground. The ground bounce, although still visible on an oscilloscope, was not of a large enough magnitude to affect the operation of the DSP Interpolator board. In future revisions, a board with a ground plane should be used to prevent this problem.

2.5 Sensor Results

Once the electronic interface issues were resolved, the encoder functioned perfectly. The encoder output was stable even down at the smallest bit. Thus the analog electronics and converters must have a minimal amount of noise, since the output is so stable. The resolution 63,201,280 $\frac{\text{cts}}{\text{rev}}$ is amazing, and allowed the signal to be directly differentiated for a velocity signal. With lower resolution encoders, this often proves to be a noisy operation which reduces control performance, but no problem was encountered here.

Integration of the MicroE laser encoder into the RFTS provided an immediate and dramatic improvement in RFTS performance. High-bandwidth controllers designed for the axis were previously of limited functionality, since the high frequency gain primarily amplified sensor noise. Installation of the encoder immediately lowered the high frequency tool motion, through a combination of high resolution and low noise, even without any other modification to the controller parameters. The MicroE encoder combined the best of both the analog and discrete measurement realms – the high resolution typically obtainable through amplifying analog sensors, and the non-existent noise characteristic of a discrete measurement sensor.

This performance improvement was clearly evident in the cut lenses. Previously, the naked eye could easily observe unwanted tool motion with the cut lenses, in the form of gouges where the tool plunged into the cut surfaces. After installation, there were essentially no such defects. As of yet, there have been no known problems with the accuracy of the encoder. Currently, however, accurate lenses have been obtained only by a "cut-measure-recut" method, where cut lenses are probed on a coordinate measuring machine (CMM) and the toolpath is then adjusted to compensate for the error. This would, of course, compensate for encoder error as well as any other sources of error. The accuracy of the encoder remains to be investigated in future work.

Chapter 3

Bearing Seals

Bearing surfaces invariably require a sealing mechanism to prevent the intrusion of harmful particles. For the large, sliding contact dovetail slides traditionally found on machine tools, the seal may consist of nothing more than a wiper to brush off metal chips. Smaller, abrasive grit particles can easily work past such a seal, but do not immediately degrade the performance of the bearing, instead resulting in accelerated wear and shorter bearing life. For high-precision rolling element bearings, however, the requirements are more stringent. The high preload forces and tight tolerances within the bearings do not allow the bearings to tolerate foreign particles, and such bearings can easily lock or exhibit difficult motion if small contaminants enter the bearings.

3.1 Seal Requirements

The toolshaft for the RFTS is supported by duplex ABEC-9 bearings mounted back-to-back inside the top and bottom bores of the casting (See Ma [17] for details on bearing design). Each set of bearings needs to be sealed on both sides. Figure 3-1 illustrates the final design configuration. Since the toolshaft terminates just past the bearings in the upper bore, the top surface is trivially sealed by using a cover to protect the position feedback sensor on the end of the toolshaft; this will also protect the bearings below. The lower surface on the underside of the upper bore will be more

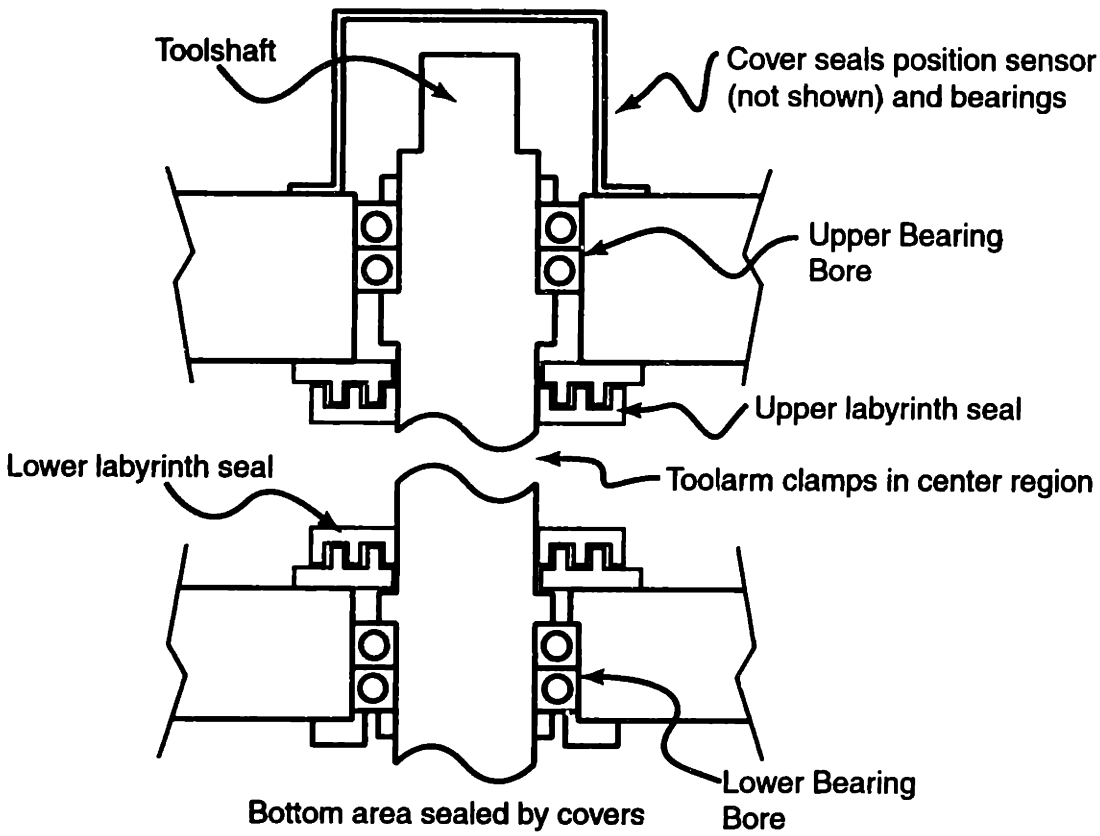

Figure 3-1: Bearing seal configuration in a cross-sectional view.

difficult, and needs a seal which accommodates the rotational motion of the toolshaft. For the lower bore, the situation is reversed; the upper surface requires a seal, while the lower surface is easily sealed by covers on the support casting. Unfortunately, these vulnerable surfaces are also those most exposed to chips and contaminants from the cutting process.

The seals for the bearings need to meet these functional requirements:

- Accommodate the rotational motion between the toolshaft and casting.
- Minimize static friction.
- Seal effectively against small contaminants.
- Incorporate a split design to allow installation around previously mounted bearings.

The rotational motion between the toolshaft and casting not only makes the seal

more complicated than a simple cover, but can also allow the seal to produce a resistance torque to the toolshaft from static friction. For high-precision, direct drive machines, such static friction can wreak havoc on the control system if it is significant enough to cause a measurable nonlinearity in the axis behavior. This "stick-slip" behavior can be difficult to overcome with a simple classical control system. Therefore, the static friction of the system needs to be minimized. Note, however, that viscous friction is beneficial to the RFTS, as it will add damping to the system.

The cast RFTS support structure arrived at MIT after post-machining with the bearings and toolshaft already mounted in the structure. Since there are interference fits involved with the mounting of the high-precision bearings, they were mounted at the machine shop which produced the precision bores, as we do not have the experience or equipment to mount such bearings here. This preassembly requires that the bearing seals be split to allow them to be installed around the previously mounted shaft and bearings; there is no possible access for completely circular parts to be slipped onto the toolshaft. Unfortunately, the surfaces in the casting to which seals were intended to be mounted were not machined, nor were the mounting holes tapped. The mounting holes were specified as tapped holes in the design drawings, but the machine shop did not produce them correctly.

3.2 Seal Design and Implementation

Rotational seals for machinery have been used for quite some time, and many excellent designs are commercially available. The *SKF Bearing Maintenance Handbook* [28] lists many possibilities in its section on sealing, including radial and axial lip seals, o-rings, packing boxes, and grease filled gap seals. Most of these are most commonly found in complete circular assemblies, and would require some effort to modify into a split design. The most intriguing designs noted there are radial and axial labyrinth seals, as depicted in Figure 3-2. With these seals, one section can clamp to the shaft and rotate freely, while the other is fixed to the support casting.

Labyrinth seals are commercially available as circular units, but the split design

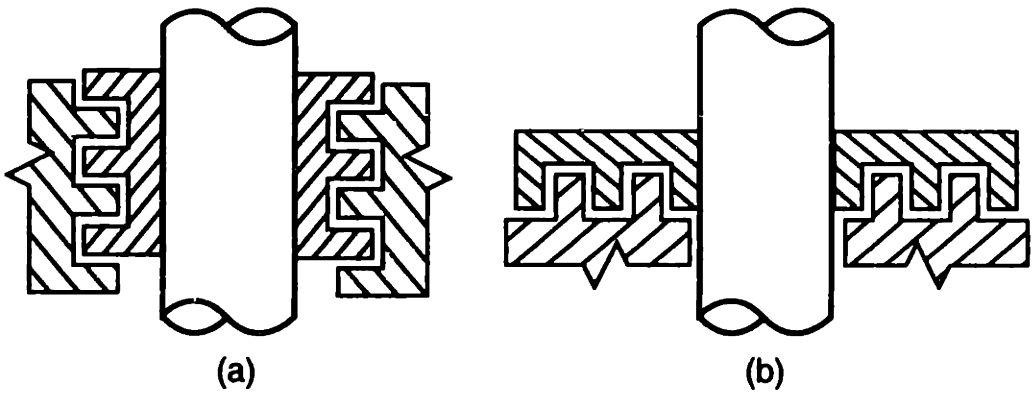

Figure 3-2: Labyrinth Seals: (a) radial, (b) axial

needed here can be easily manufactured in a conventional machine shop. Labyrinth designs are inherently non-contact, with zero static friction. Typically, they are most often used in relatively clean environments in applications where the lack of friction is essential. In our machine, however, they can be easily adapted to deal with the small chips produced in the cutting process.

Radial labyrinth seals require considerably more area on the toolshaft than axial seals, which would significantly constrain the design of the toolarm which mounts to the shaft. For this reason, the axial labyrinth seal is preferred. In addition, the vertical shaft allows the axial labyrinth seals to exploit gravity, so that even if contaminants were to intrude past one set of ridges, they would need to climb against gravity over successive sets of ridges to reach the bearings. This will be one key in ensuring a good seal against the micron level contaminants produced in lens cutting.

The integrity of the seal will be further enhanced by filling the labyrinth with grease, which should trap any particles which manage to intrude into the labyrinth. It seems unlikely that any contaminant could work through the grease, and over the ridges of the labyrinth to reach the bearings. The grease will prevent the seal from being purely non-contact, but can provide advantageous damping, as detailed in Section 3.3. Applying pressurized air into the labyrinth, which would result in a steady flow out of the seal and prevent particle intrusion, was considered as an alternative to maintain a non-contact seal. Air would also flow *into* the bearing, however, possibly blowing out the bearing lubricant, and this concept was discarded

for that reason.

The *SKF Bearing Maintenance Handbook* [28] lists recommended gaps for labyrinth bearings. For shafts of 20-30 mm, the desired gap ranges from 100 μm to 250 μm, depending on the rigidity and alignment of the bearings and structure. Other references, such as NSK [15], specify larger gaps, from 250-400 μm for a shaft diameter under 50 mm. Error motions in the shaft also need to be considered in specifying the gap. Although the bearings provide the toolshaft with an *axis of rotation* which is consistent to better than 2 μm, as detailed by Ma [17], the shaft surface *itself* exhibits a measured runout of $\pm$12.5 μm. Thus even a perfectly manufactured seal could have interference problems when clamped on the shaft if the gaps are too small to accommodate the runout.

This raises another consideration in specifying the gap; the accuracy of the manufacturing process. Although the circular labyrinth is perhaps best made on a lathe, adequate tooling did not exist for making such deep, narrow grooves on the available CNC lathe. Instead, the seals were made on a 3-axis CNC mill, a Bridgeport EZ-Track. This machine has a resolution of 0.0005 in. and is felt to be accurate to almost $\pm$0.001 in. This manufacturing consideration, along with the recommendations listed earlier, led to the specification of a 0.005 in. gap, or about 127 μm. The axial gap is less critical, as it can be adjusted by sliding the section clamped to the toolshaft up or down. Note that all of these gaps can be affected by thermal expansion. The upper set of bearings, in fact, "floats" in the bore, and is designed to move axially to accommodate thermal expansion and contraction. This will limit the minimum axial gap size.

The seals were manufactured out of aluminum; a prototype is shown in Figures 3-3 and 3-4. Each half is assembled from two identical pieces, and each piece has a #4-40 screw and 0.125 in. diameter dowel pin at one end, and a reamed hole and tapped hole at the other, so that the two identical pieces can be mated together. The two pieces were clamped together prior to the machining of the labyrinth itself, so that a matched pair could be produced. The labyrinth consists of three raised 0.125 in. wide rings on each side, spaced at appropriate radii so that the raised rings

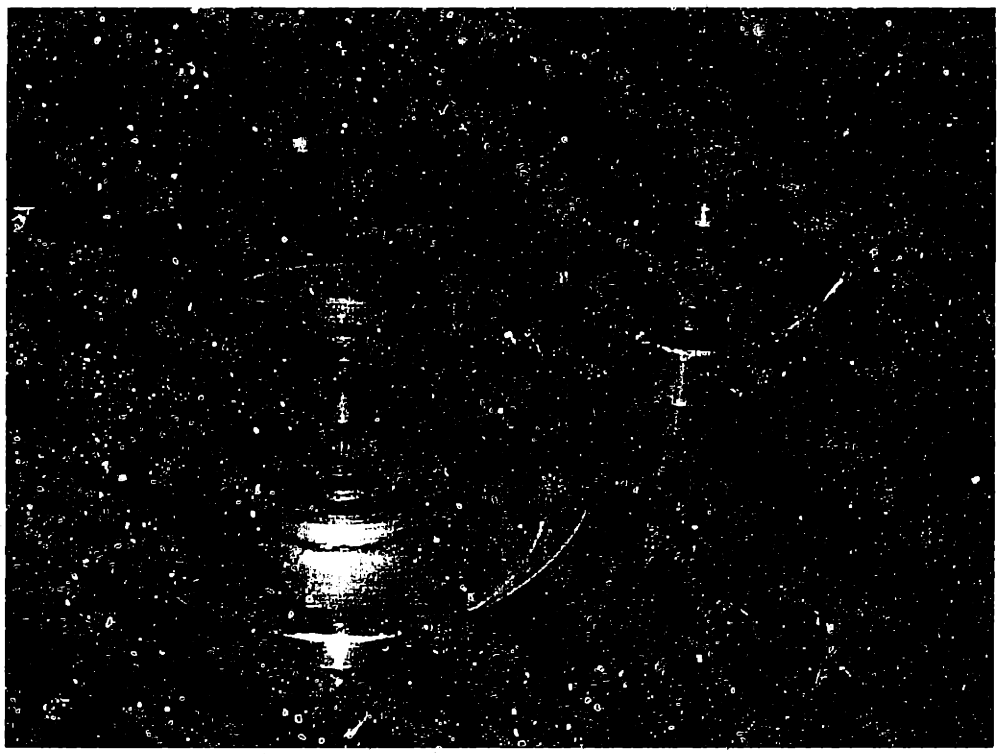

Figure 3-3: Upper and lower halves of prototype seal.

on one side fit into the valleys on the other side. The selection of this width of ring enabled the pieces to be machined with a common 0.125 in. endmill, to a depth of 0.25 in. Top and bottom halves of a seal were then matched to each other by lapping with an abrasive compound.

Mounting the seals was not trivial, since the mounting surface had not been properly finish machined, as noted earlier. It was necessary to form a new mounting surface, by replicating the bottom seal surface with DWH 311 [6]. DWH 311 is a metal-filled epoxy utilizing a low shrinkage polymer. By coating the bottom of the seal with mold release, securing the seal in the correct position, and filling the gap with DWH 311, the correct mounting surface is replicated in the epoxy. The seal was mounted in the correct position by adjusting 3 setscrews mounted 120° apart around the outer diameter of the seal. The position was initially adjusted radially and axially by mounting a dial indicator on the shaft and minimizing the variation in these directions. As a final check, the shaft seal section was mounted, and checked for interference with the other half. The DWH 311 was then used to fill the gap between

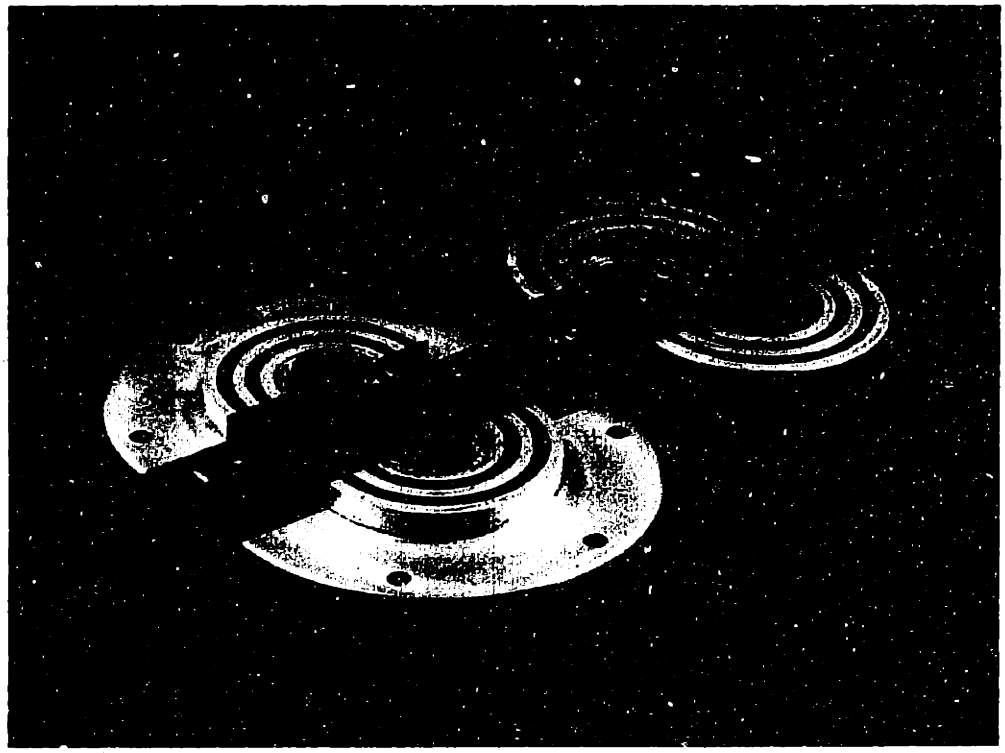

Figure 3-4: Upper and lower halves of prototype seal, split.

the seal and casting.

Prior to final mounting of the seals, the bearings were flushed extensively with solvents, including isopropyl alcohol and acetone, then filled with the lubricant recommended by the bearing manufacturer, Krytox[14] grease. Note that care must be taken with the solvents used in flushing the bearings, as there are polymer components within them which might be damaged by exposure to certain solvents. The bearing seal sections were then centered axially on their surfaces and secured with "5-minute" epoxy. This enables them to be removed with a sharp impact, should that be necessary. As an additional precaution, the perimeter of these sections were sealed against the casting with a common silicone sealant. The bearing seal halves were then filled with the same Krytox grease as used in the bearings, and the shaft sections clamped into place.

3.3 Damping

One additional interesting application of using grease-filled labyrinth seals is to develop damping for the toolshaft. Torsional resonance between the servomotor and toolshaft, through the flexible coupling, is one control issue, as noted in Chapter 4. Any damping of this resonance is certain to be beneficial, and could enable a higher bandwidth control loop. The seals could also be used to provide axial damping to the shaft, should this become a problem. Even though cutting forces are applied in the axial direction, this is less likely to be a problem, however, given the stiffness of the structure.

The flow of a viscous fluid in the labyrinth can be modeled as flow between two parallel plates, separated by a gap h, as shown in Figure 3-5. This approximation can be made since the magnitude of the gap h is much less than the radius of curvature, R, of the seal. This type of flow is known as *plane Couette flow*, and is well documented in texts such as White [37]. A shear stress τ acts on the top plate, with an equal and opposite shear stress acting on the lower plate. This stress is given by

$$\tau = \mu \frac{V}{h} \tag{3.1}$$

where μ is the viscosity of the fluid and V is the velocity of the plate. For the circular rings of the labyrinth, this becomes

$$\tau = \mu \frac{\Omega R}{h} \tag{3.2}$$

where Ω is the angular velocity of the shaft, and R is the radius of the ring.

By multiplying this shear stress by the area of the ring, and then again by R, the length of the "lever arm" from the ring to the shaft, the resistance torque or damping of the ring can be calculated (depending on whether the velocity is included or factored out). The contributions of each ring interface can then be summed together to find the total value. Note that only the radial interfaces are considered, since the axial gap is likely to be much larger. Converting the radii to diameters, this gives the damping

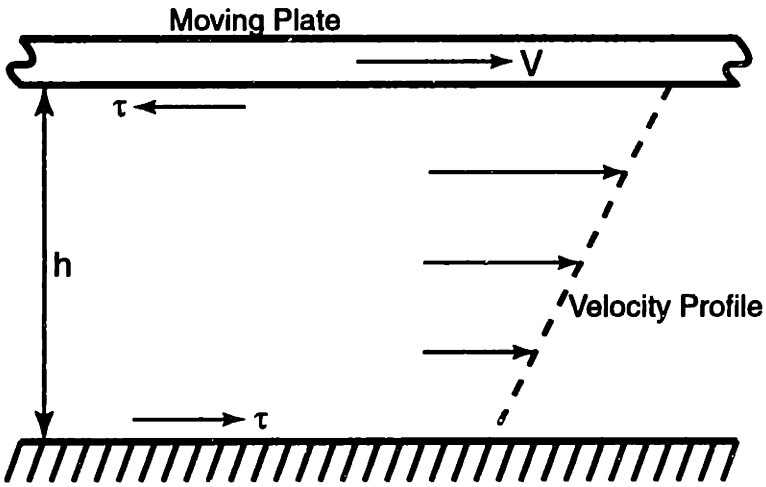

Figure 3-5: Plane Couette flow between parallel plates. No-slip conditions are assumed at the top and bottom plates.

as

$$b = \frac{\mu \pi t}{4h} \sum_{i=1}^{n} D_i^3 \tag{3.3}$$

where D_i are the diameters of the rings and t is the depth or height of each ring.

The Krytox 240AB grease used in the bearings was also used to pack the seals. Grease consists of a base oil mixed with a thickener, which in this case is polytetrafluorethylene. To estimate the viscosity of the grease, the viscosity of the base oil is used. Krytox 240AB base oil is specified to have a kinematic viscosity ν of 230 cSt@20°C and 85 cSt@38°C, with a density of 1.92 $\frac{g}{ml}$. Converting this to absolute viscosity, $\mu = 0.4416$ to 0.1632 Pa-s, depending on temperature.

Evaluating Equation 3.3 for one seal, the damping ranges from $8.5 \cdot 10^{-3}$ to $3.14 \cdot 10^{-3}$ N-m-s. Is this significant *additional* damping? It is difficult to say, since the amount of intrinsic damping of the system without the seals is difficult to estimate and quantify. Instead, it is easier to examine how the dynamic model of the system responds to variation. A dynamic model of the RFTS system is developed later, in Section 4.4. By adding a damping term to Equation 4.19, the effect of damping variation on the magnitude of the system resonance can be examined. The addition of

the damping term results in the system transfer function

$$\frac{\theta_2}{T} = \frac{K/(J_t J_m)}{s^4 + \frac{b}{J_t}s^3 + \frac{K(J_m+J_t)}{J_m J_t}s^2 + \frac{Kb}{J_t J_m}} \tag{3.4}$$

where K is the stiffness of the coupling between the motor and toolshaft, and J_m and J_t are the values of the rotational inertia of the motor and toolshaft, respectively.

Estimating the values of stiffness and inertia from Ma [17], $K \approx 10000 \frac{\text{N-m}}{\text{rad}}$ and $J_t \approx J_m \approx 5.6 \cdot 10^{-4}$ kg-m^2. Evaluating this model at the lower temperature range, it is found that the addition of the second seal causes a 5 dB reduction in the magnitude of the resonance. If the damping could be doubled yet again, a similar reduction could take place. While a large resonance is still present, a 5 dB reduction can result in a useful increase in control bandwidth. Thus the seal damping could be significant for control purposes. Unfortunately, the actual damping provided may be quite a bit lower, as manufacturing tolerances seem to have created larger than desired gaps. In particular, the circular pieces were clamped between a flat and V-block during machining. Use of a completely circular clamp could have produced better results.

Further design work could also optimize these seals to provide axial and radial damping. The small gaps present in the axial and radial directions can produce "squeeze film" damping as the viscous fluid is forced from the gap. These effects can be quite significant for small gap sizes, as noted by Ludwick for a fine positioning stage in [31]. I have not attempted to analyze such effects here, however.

Chapter 4

Functional Requirements and Design Parameters for a Rotary Toolarm

4.1 Design Process

In the design of components with conflicting design requirements, it is often necessary to adopt a formalized framework or design philosophy to achieve a satisfactory and optimal solution. In many instances, there is a tendency for the designer to jump straight to conceptual designs without carefully considering the requirements that need to be satisfied. This not only prevents a good analysis of which of the presented concepts is the most satisfactory, but also may prevent the most optimal solution from being developed and considered. Several methods have been developed which attempt to regulate and structure the design process in such a way that the optimal solution is achieved. Among these are the Axiomatic Design process, developed by Suh[32], and the Analytic Hierarchy Process, developed by Saaty[26]. Such methods are well suited and invaluable for the development of complex systems, where the amount of information and interaction in the design is quite large. However, for a singular component of reduced complexity, a good design can be achieved with a more

simple formal process.

In the design of the toolarm for this rotary fast tool servo, a basic framework was developed, consisting of designating the desired Functional Requirements (FRs) and associated Design Parameters (DPs). The Functional Requirements are a list clearly specifying each of the design goals of the component, while the Design Parameters are the lists of design variables corresponding to each item in the list of Functional Requirements. Ideally, the FRs should all be decoupled from one another; that is, a design variable should not appear on a list of DPs for more than one FR. Unfortunately, for this toolarm, several of the FRs are coupled. For large systems, the utility of the formalized design methodologies now becomes obvious, as they are specifically tailored to resolving these conflicts. The reduced complexity of this component, however, will allow us to rely only on the framework developed here, as the design tradeoffs are relatively few in number. This framework aids the designer in exploring many possible design concepts and to avoid being channeled into a particular concept too early. Hence it performs a very important role in the early development and evaluation of a design.

The following list presents the major functional requirements of the toolarm for the rotary fast tool servo. These items will each be explored in later sections:

- Toolholding
- Geometric Compatibility
- Inertia Minimization
- Stiffness Maximization
- Tool Height Adjustment

4.2 Toolholding

The principal functional requirement of the toolarm is to hold a cutting tool at the desired location with respect to the rotary axis. The specific cutting process utilized

in this machine is known as Single Point Turning (SPT), due to the fact that only one small region of the cutting edge of the tool is in contact with the surface being cut at any given time. Since this point of contact changes only slowly on the tool over the surface being cut, very smooth and consistent surfaces can be obtained. This stands in contrast to multiple point of contact tools, such as multiflute endmills, where the cut surface is marred by multiple contacts with the tool, each of which likely cuts into the surface at different depths with different finishes. Typically, the tools used for SPT are of zero degree rake angle with a constant radius, but on occasion different rake angles are utilized to obtain the best surface finishes or minimize tool wear when cutting a particular material. However, toolpath planning may then be more complex if highly accurate surfaces are desired, since often such tools are formed by tilting constant radius tools. If the tool has a constant radius in the plane normal to the cutting velocity, toolpath calculations are relatively simple since the tool profile is a constant radius. If it is then tilted out of this plane to achieve a different rake angle, its cutting profile then becomes parabolic, and hence the toolpath calculations become more complicated.

The functional requirement may now be understood as holding a constant radius, zero degree rake angle tool in a plane normal to the cutting velocity provided by the spindle. Several design parameters may now be associated with this requirement. First, the material from which the cutting tool is formed needs to be determined. Next, a method for fixturing the tool is required. Finally, the tool radius needs to be specified.

4.2.1 Tool Material

Several different cutting tool materials are commonly used for turning, depending on the particular application. In the metal cutting industry, High Speed Steel (HSS), Tungsten Carbide (WC), and Cubic Boron Nitride (CBN) tools are often used. The first is usually used to directly form the cutting tool assembly, while the latter two are usually available as small inserts which are supported by a toolholder. These materials are listed above in order of increasing hardness, as hardness is one of the

most desirable qualities in a cutting tool material. High hardness corresponds to a high local yield strength, which allows a cutting tool to maintain a sharp edge over many cuts. But there is no need to restrict ourselves to those materials used in metal cutting. Diamond is perhaps the ultimate cutting tool material, as it has the highest known hardness and modulus of elasticity, as well excellent thermal conductivity and extremely low friction coefficient. It is not used often in the metal cutting industry due to cost, brittleness, and problems with cutting ferrous materials. Often, if used to cut ferrous materials, the carbon from which the diamond is formed diffuses into the ferrous material, causing a chemical breakdown of the tool edge, as well as the conventional breakdown from cutting stresses. Since our machine is designed for cutting lenses formed from plastic materials, there should be no material incompatibility with diamond.

Diamond cutting tools are available in two forms, polycrystalline diamond and single crystal diamond. Polycrystalline diamond, as the name suggests, is formed from many individual synthetic diamond crystals, often through a film deposition technique over a substrate. Single crystal diamond, in contrast, is formed from a uniform lattice of carbon atoms with no grain boundaries. Such diamonds may be found naturally, or grown synthetically, but the creation of a large single crystal is difficult and expensive, and hence this places a limitation on the combination of the maximum radius of a cutting tool and its included cutting angle. The single crystal nature of these tools provides a tremendous advantage in the ability to generate smooth surfaces. Since there are no grain boundaries or other defects in the crystal, the tool edge can be made extremely sharp with no roughness, allowing the tool to impart an extremely smooth surface in the material being cut. In addition, this trait is responsible for the single crystal tools being commonly available with tightly toleranced radii, so called controlled-wave tools. Contour Fine Tooling[5], for instance, produces tools with a waviness on the tool radius of 0.25 μm as standard parts, and with 0.05 μm available as an option. This tight tolerance on the radius allows form error in the cut workpiece to be minimized. Other tool materials, such as the tungsten carbide and polycrystalline diamond tools, are not available with such tightly controlled radii.

4.2.2 Tool Fixturing

Any cutting tool that is held by the toolarm needs to be fixtured securely. In the metal cutting industry, replaceable cutting inserts are often held into a matching recess by a differential screw. The recess provides a positive tool location as well as a large support surface, and the differential screw provides a large amount of force to keep the cutting tool in place in the recess. The high preload forces of the screw help ensure adequate seating of the tool for high stiffness, which in turn prevents tool chatter as well retaining the tool in the presence of cutting forces. There are two positive benefits of using insert tooling. First, the mass of the tool is kept to a minimum. Only the sharp cutting edge of the tool is needed, and the recess needed to hold a small insert in place can easily be removed from the support structure. The other main benefit is that the positive tool location provided by the recess can help to minimize the machine calibration necessary after a tool change. However, given the high accuracy requirements of our machine, and the typical tolerances on manufactured tooling, it seems unlikely that the tool location would be repeatable enough to eliminate the requirement of calibration after a tool change.

The other main alternative to insert based tooling is to use cutting tools brazed onto metal shanks. The brazed interface of the tool and shank is stiff and solidly supports the cutting tool. This bonded interface is generally much more reliable than that of insert tooling, where small particles between the tool and recess, or some manufacturing error, can cause a geometric incompatibility between the tool and seat, resulting in a loss of stiffness. This method of fixturing is also the most flexible, since almost any kind of tooling can be brazed to a shank. Single crystal diamond tools, for example, are not as commonly available in insert form. Other useful items, such as metrology devices, may be fixtured to the toolarm by a shank based holder as well. Unfortunately, the mass of the shank needs to be carried by a toolarm as well. In addition, the unsupported length of the shank needs to be carefully checked to minimize any loss of stiffness due to the cantilever beam action of the shank.

4.2.3 Tool Radius

The tool radius is another design parameter that needs to be specified. Larger tool radii have several advantages over smaller radii, but larger radii tools may be difficult to manufacture, especially in the case of tools made from single crystal diamond. The larger radius helps to minimize interference problems of the toolarm with the workpiece being cut, since it pushes the toolarm structure farther away from the lens. In contrast, a smaller radius tool will pull the support structure closer to the lens, increasing the possibility of destructive interference. The tool radius R_t will also have an important effect on the process time; that is, the time required to manufacture one lens. This is because the tool radius combined with the cross-feed have a direct effect on the theoretical surface finish, which is formed by "scallops" of radius R_t spaced apart by the cross-feed distance f. Figure 4-1 illustrates the model. This theoretical finish simply assumes the workpiece conforms exactly to the shape of the tool edge as it passes underneath. As the tool radius R_t becomes smaller, the cross-feed f also needs to be reduced in proportion to maintain the desired surface finish. It is unlikely that the spindle speed could then be increased to compensate, since it will be limited by the required accelerations on the fast tool servo. The exact relationship is noted by Ludwick[12], where h is the height of the "scallops" formed in the surface by the circular tool:

$$2R_t h = \left(\frac{f}{2}\right)^2 + h^2 \tag{4.1}$$

Since the surface finish of interest is quite small, $h \ll f$, thus giving validity to the approximation

$$h \approx \frac{f^2}{8R_t} \tag{4.2}$$

4.3 Geometric Compatibility

Geometric constraints on the toolarm arise from the need to avoid toolarm-lens interference during the cutting process, which would obviously be destructive to the lens

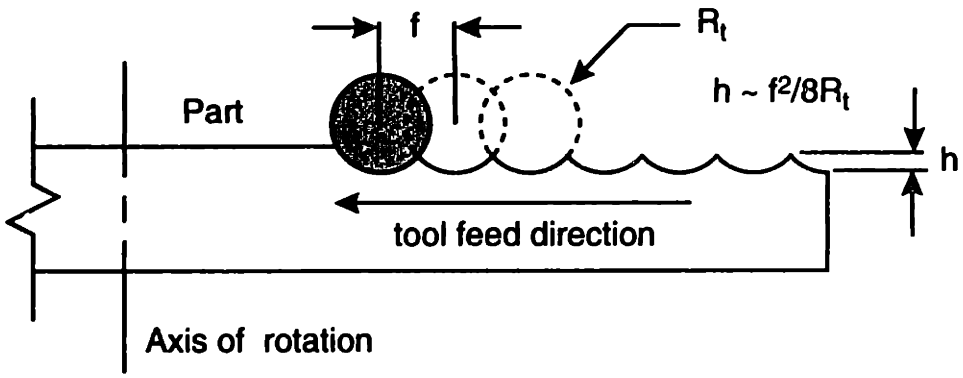

Figure 4-1: Illustration of theoretical surface finish model. From Ludwick[12].

surface. This problem is quite dependent on the kinematic configuration of the tool; the particular toolarm and cross slide positions necessary to cut a given surface on the lens. This kinematic configuration is dependent not only on the shape of the lens surface being cut, but also on the Z-location of the chuck and spindle. The Z-location of the spindle and chuck along the spindle axis relative to the Z-location of the rotation axis of the toolarm is a degree of freedom which can be set by the mounting of the spindle and chuck assembly. However, once set, it cannot easily be moved (In future machines, we may want to include a Z-slide to allow this adjustment to be made). Therefore some effort will first be used to determine the optimum placement of the spindle. The lens shapes which must be cut are dictated by customer requirements, but in any practical design we will need to specify the machine for a certain range of lenses. While the customer may desire that the machine produce any possible lens prescription, the extreme lens combinations are unlikely to be ordered, and will place more severe constraints on the machine configuration. Hence the sensitivity of the machine design parameters to both customer requirements and the spindle and chuck placement needs to be examined, and the ideal tradeoffs determined.

Once the spindle and chuck placement is specified, the exact geometric constraint on the toolarm for different lens prescriptions will be examined. The toric nature of the lens surface makes determining the acceptable volume for the toolarm to occupy

difficult, since the toolarm will be moving in and out as the toric lens rotates. At first glance, it may appear that by setting the toolarm to occupy the volume described by the smallest radius of curvature of the lens (the "cross curve "), one would guarantee that no lens interference exists. However, this is not the case, since as the toolarm rotates to cut the larger radius of curvature (the "base curve"), it must clearly depart from the volume of the cross curve. This may not appear to be a problem, since the clearance volume described by the base curve is much larger. The transition between the two curves does provide a possibility of interference, as the tool moves into the part. The possibility of interference can be directly associated with the slope on the lens. The geometric constraint can then be divided into two sections; the clearance volume described by the smallest cross curve, and the slope constraint determined by the maximum slope on the toric surfaces.

4.3.1 Optimal Kinematic Relationships

The kinematic configuration of the toolarm and spindle will factor into the acceleration requirements of the FTS, one basis for determining the "optimal" configuration. The FTS motion is intended to primarily move the tool along the spindle axis; the cross slide can then provide motion perpendicular to the spindle axis. However, if the toolarm is extended to a large angle in order to reach the spindle, movement of the arm does not provide a large component of motion in the desired direction. Large angular changes are therefore needed to move the tool away from the spindle, which consequently place larger acceleration requirements on the FTS. This effect can be modeled by considering the θ stroke necessary to produce a given feature height, as shown in Figure 4-2. Regardless of the prescription, production of lenses of a given thickness will result in the same final angle θ_2; therefore, the feature height h will be referenced against this angle θ_2, which, along with the length of the toolarm L, will set the kinematic configuration of the machine. The relationship between the feature height and toolarm angles is then given by

$$h = L(\sin\theta_2 - \sin\theta_1) \tag{4.3}$$

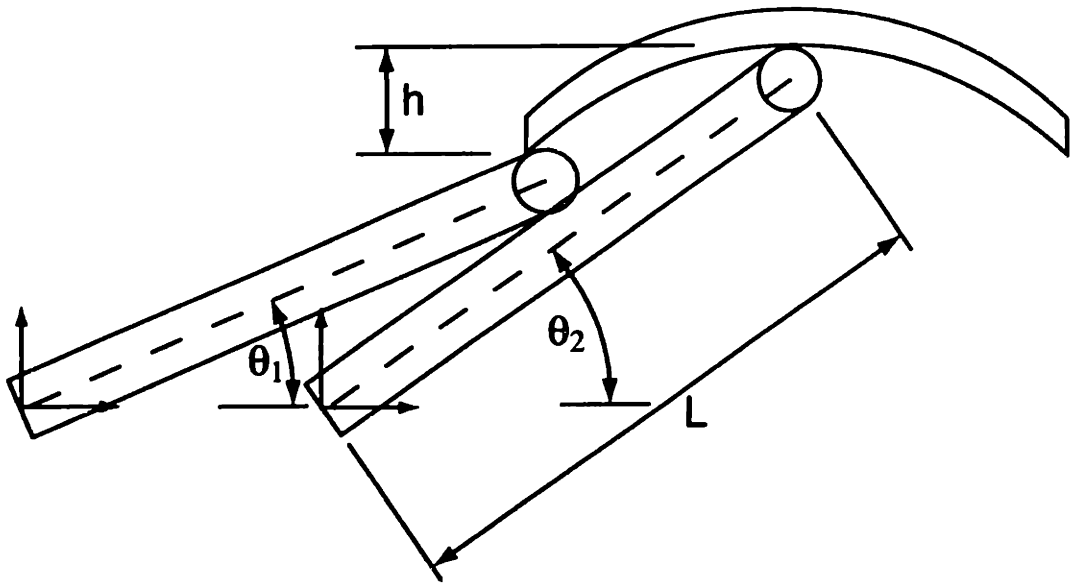

Figure 4-2: Schematic of toolarm relationships. The arm is pictured in its initial and final configurations. Note that these configurations are possible due to movement of the lens which is not shown. The axis of the arm remains fixed.

By noting that the stroke of the toolarm is given by $\theta_c = \theta_2 - \theta_1$, substitution and rearrangement produces

$$\theta_c = \theta_2 - \arcsin\left(\sin\theta_2 - \frac{h}{L}\right) \tag{4.4}$$

I then investigate the effect of the parameters in Equation 4.4 on the required stroke of the toolarm, and hence the effect on acceleration. Figure 4-3 shows a plot of the effect of toolarm length on the theta stroke necessary to produce a 2 cm change in height. Larger length arms seem beneficial to reducing the acceleration requirements on the FTS, but also allow cutting forces to produce larger torques against the FTS. This effect will scale linearly with toolarm length L, and could be of more importance if the final angles are kept to the "flat" portion of Figure 4-3. Note that there will also be an undesirable inertia increase which will scale with L^2. The casting structure of the FTS also places a constraint on the length of the toolarm. Ideally, the toolarm should be able to freely spin within the casting without contacting any portion of the supporting structure; this allows easy control development without worrying about

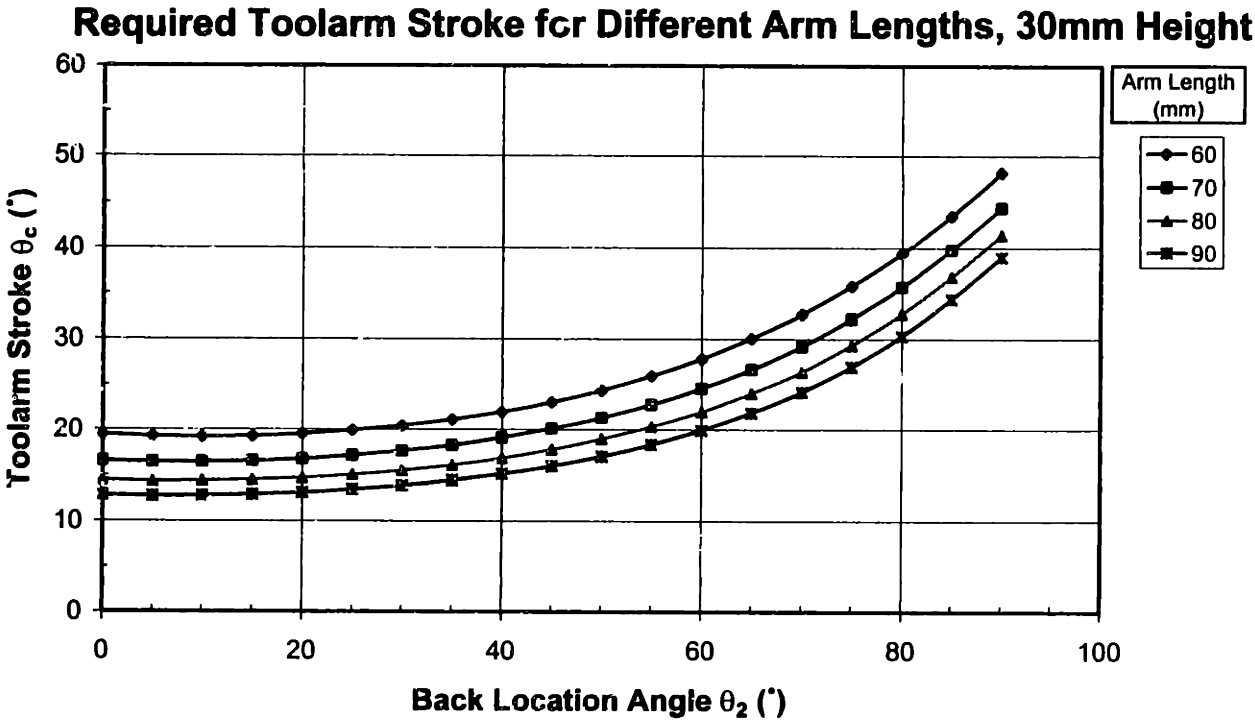

Figure 4-3: Required θ stroke for 20mm feature depth.

"crashing" the toolarm. To meet this ideal, the toolarm should be no longer than ~8.5 cm in length. Limiting the toolarm to a conservative 8 cm length, Figure 4-4 was developed. The effect of the back lens location, or final angle, on the required θ stroke is clearly illustrated.

Another basis for determining the "optimal" configuration of the toolarm and spindle is the amount of geometric constraint the configuration places on the toolarm. While the exact constraints are developed in the "clearance volume" and "slope constraint" sections mentioned earlier, an analytic treatment can be developed to more easily compare this basis with the previously determined effects on acceleration. The "amount" of geometric constraint on the toolarm can be classified by the maximum interference of a lens with a "straight-line" toolarm as illustrated in Figure 4-5. The "maximum interference" is taken as the largest perpendicular distance a point on the lens crosses over the straight-line toolarm. Referring to Figure 4-5, the location of the center of the tool $P_1(x_1, y_1)$ and the slope of the straight-line toolarm m_1 are given

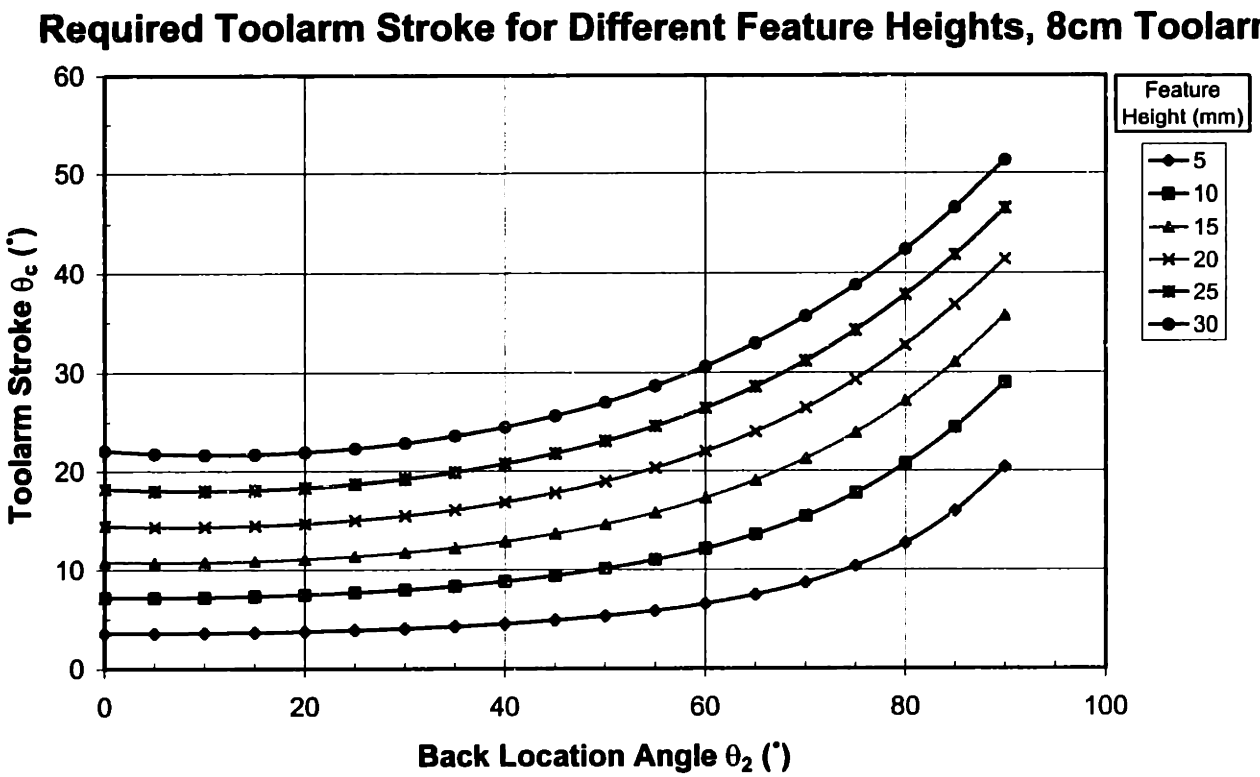

Figure 4-4: Required θ stroke for different lens back locations.

in the pictured coordinate system by

$$y_1 = (R_L - R_t)\cos\phi \tag{4.5}$$

$$x_1 = -(R_L - R_t)\sin\phi \tag{4.6}$$

$$m_1 = \tan\left(\arcsin\frac{y_1 + L\sin\theta_2 - R_L + R_t}{L}\right) \tag{4.7}$$

The location of the interference point $P_2(x_2, y_2)$ of the lens is given by

$$x_2 = -R_L\cos\alpha \tag{4.8}$$

$$y_2 = R_L\sin\alpha \tag{4.9}$$

Noting that the slope of the perpendicular distance must be $m_2 = -\frac{1}{m_1}$, and the general equation for a line $(y - y_0) = m(x - x_0)$, lines through P_1,P_2, and P_3 can be

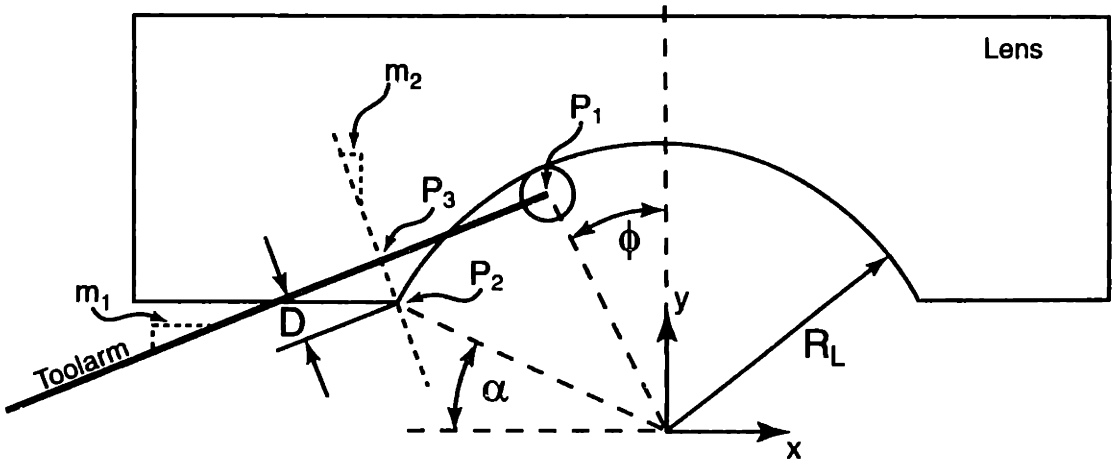

Figure 4-5: Schematic of "straight-line" toolarm interference with lens.

established, and the intersection point $P_3(x_3, y_3)$ determined as

$$x_3 = \frac{m_1}{m_1^2+1}\left(m_1 x_1 + \frac{1}{m_1}x_2 + y_2 - y_1\right) \tag{4.10}$$

$$y_3 = m_1(x_3 - x_1) + y_1 \tag{4.11}$$

The interference distance is then given by

$$D = \sqrt{(x_3 - x_2)^2 + (y_3 - y_2)^2} \tag{4.12}$$

By iterating Equation 4.12 for different configurations and lenses, their relationship with interference can be established. Since a stated objective of the project is to cut lenses of up to 100 mm diameter, and 20 diopter curvature, this can be used as a "worst-case" situation. R_L will then be 26.5 mm, while α will peak at 90°, since $R_L <$ maximum radius. This results in the plot shown in Figure 4-6.

It is clear from Figures 4-4 and 4-6 that as θ_2 increases, the interference problem is minimized while the required accelerations increase. Since the two requirements are in opposition, it should be possible to determine an ideal θ_2 by finding the minimum value of an index based on weighting the two requirements. At this point, large accelerations are no more undersirable than tool interference, so I simply normalize

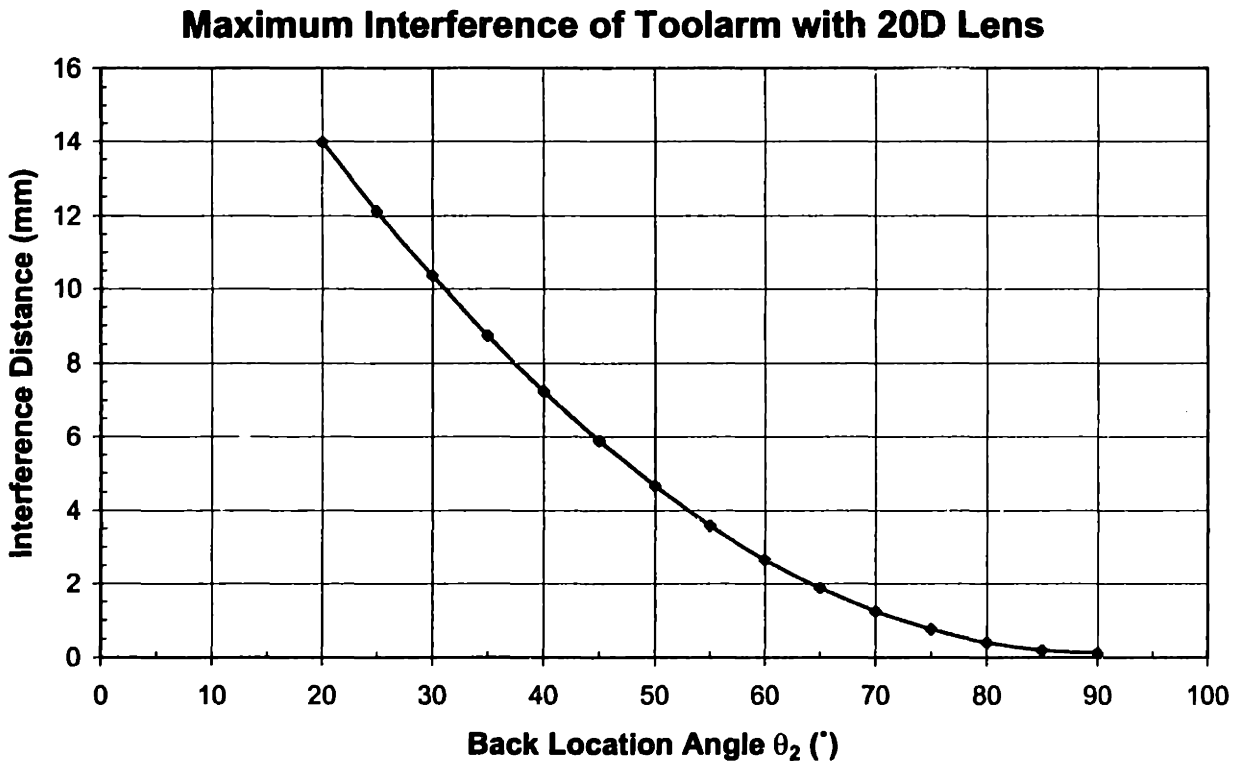

Figure 4-6: Interference of "straight-line" toolarm with 20D lens.

the results of each test for a 20D lens and then simply sum the normalized values. The index is thus $I = \theta_{cnorm} + D_{norm}$. These results are presented in Figure 4-7. From this plot, it appears that a value of $\theta_2 = 60°$ may be the most optimal choice, but one could change this by putting a premium on acceleration over interference, or vice-versa. Once further detailed design has taken place, these results can be examined again based on which problem appears more difficult to solve.

4.3.2 Slope Constraint

The slope constraint on the tool results from the in and out motion of the tool when cutting toric lenses. When cutting spherical or rotationally symmetric aspheric lenses, the RFTS will not move with each rotation of the spindle, and the workpiece surfaces will be perpendicular to the rake face of the tool (for a 0 degree rake tool). This conventional machining process is shown in Figure 4-8 (a). In any system where a fast tool servo is used for cutting toric lenses, the mechanics of the cutting change, and the tool will be cutting on a slope caused by the toric shape of the part. This

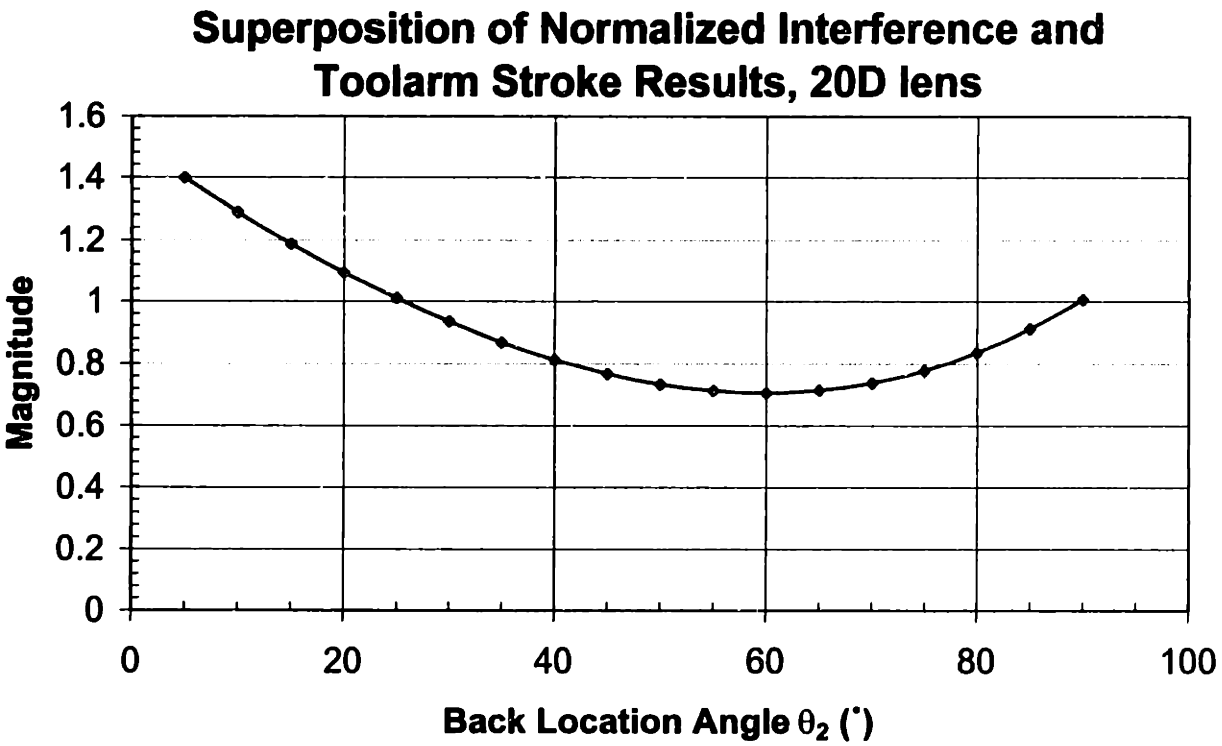

Figure 4-7: Unweighted summation of θ_2 effects on interference and toolarm stroke for a 20D lens.

slope will cause the rake and clearance angles, which are normally considered fixed in the SPT process, to change, as shown in Figure 4-8 (b).

The rake and clearance angles are normally considered important process parameters, which are optimized for cutting particular materials. Cutting toric lenses with the RFTS will unfortunately cause these to change with each revolution during the cutting process. Given a zero degree rake angle tool, the rake angle with respect to the local surface contact point will vary between the maximal $\pm$ slopes on the part. Of even greater concern is the clearance angle, which must always remain greater than zero degrees, or the tool clearance face will be dragged destructively across the finished surface of the lens. It is this property which gives rise to the slope constraint on the toolarm; the toolarm must follow the tool in maintaining the required clearance angle.

The maximum slope encountered during cutting will depend upon the particular lens being manufactured. This constraint can be examined in more detail by examining the maximum slope of different lenses. Since the slope is entirely dependent on the

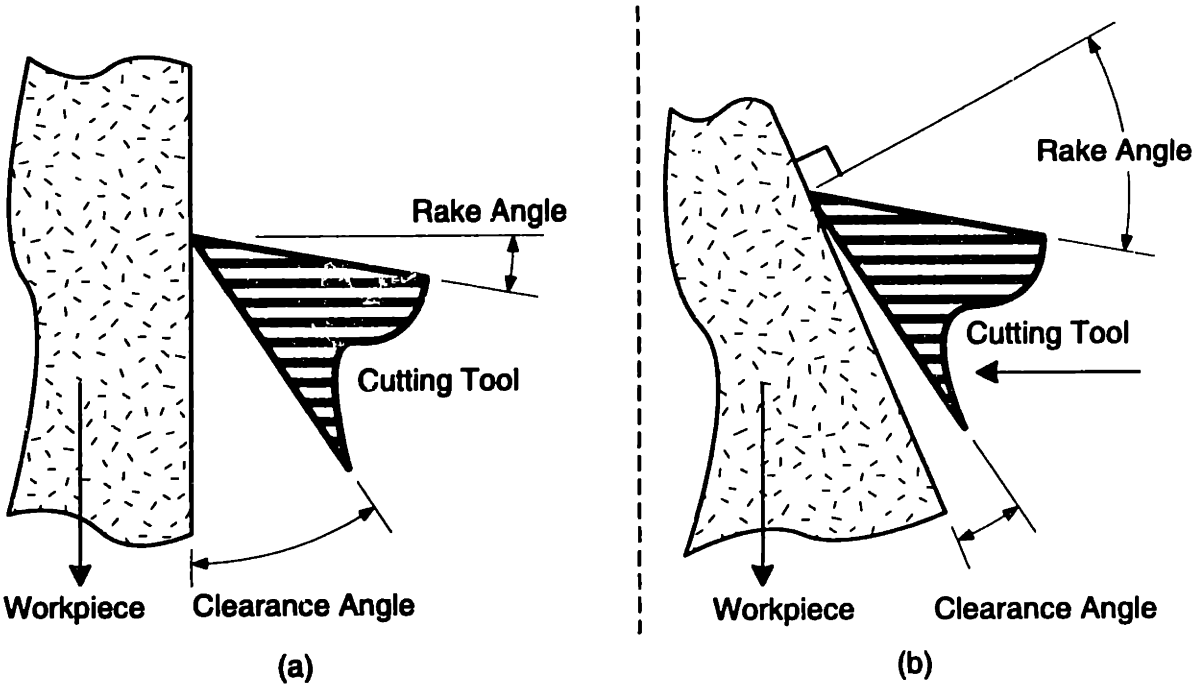

Figure 4-8: The Single Point Turning process: (a) conventional (b) with fast tool servo motion.

lens geometry, it can be determined by differentiating the equation for the toric lens given in Equation 1.1. The slope is given by $\frac{\partial z}{\partial s}$, where ∂s is the differential distance traveled for a given change in lens height. Since ∂s is dominated by the effect of the spindle velocity, $\partial s = r\partial\theta$, where r is the radius from the center of spindle rotation. Thus to begin, it is best to convert Equation 1.1 to cylindrical coordinates, where $x = r\cos\theta$ and $y = r\sin\theta$. This gives the equation as:

$$z(r,\theta) = R_b - \sqrt{(R_b - R_c + \sqrt{R_c^2 - r^2\sin^2\theta})^2 - r^2\cos^2\theta} \tag{4.13}$$

Differentiating with respect to θ and dividing both sides by r,

$$\frac{\partial z}{r\partial\theta} = \frac{r\sin\theta\cos\theta(R_b - R_c)}{\{(R_c^2 - r^2\sin^2\theta)[(R_b - R_c + \{R_c^2 - r^2\sin^2\theta\}^{\frac{1}{2}})^2 - r^2\cos^2\theta]\}^{\frac{1}{2}}} \tag{4.14}$$

This slope can then be converted to an angular form

$$Slope(radians) = \arctan\frac{\partial z}{r\partial\theta} \tag{4.15}$$

Figure 4-9 shows the slopes of a typical toric lens as calculated using the result above. As might be expected, the shape mimics that of the toric lens, with the maximum slope occuring spatially displaced by 45° from the surface peaks and valleys. The maximum value of the slope for different lenses is of more interest. By iterating Equation 4.14 for different lenses, the plots in Figures 4-10 and 4-11 are produced, with each figure representing the values at a different radius r. By combining intuition with some analysis of Equation 4.14, one may note that the maximum slope of some lenses will approach 90°, as the radius r of the tool from the spindle axis becomes much larger than the smallest radius of curvature on the lens. In fact, for many areas the maximum slope will be undefined; the toric surface simply does not exist at certain (r, θ) coordinates. One may imagine a cylindrical lens, with an infinite radius of curvature R_b and some finite radius R_c. At some radius $r \gg R_c$, the tool will come across an "edge" in this lens of nearly 90° and need to plunge in and out of the part at this angle. It is impossible to manufacture these lenses at that radius with any type of turning machine and FTS, since the slope of 90° cannot be achieved. For the plots in Figures 4-10 and 4-11, only lenses which were mathematically well defined were plotted. In both plots, only those lenses which have a "cross-curve" radius R_c less than the radius r are included.

It is apparent from these figures that some tradeoff must be made between the lenses that can be cut and the machine configuration. A typical commercial machine which utilizes the SPT process, the Coburn Lensmaker[10], has a clearance angle on its tools of 24.5°, thus limiting the lenses it can cut according to these figures. Note that the maximum slope encountered on the lens is a strong function of the radius r, as shown in Equation 4.14 and Figures 4-10 and 4-11. It is desirable to be able to cut most lenses out to the 45 mm radius, 90 mm diameter shown in Figure 4-10, as that would be consistent with the current production processes. However, the strong dependence of slope on radius may restrict extreme toric lenses to smaller diameter lenses only.

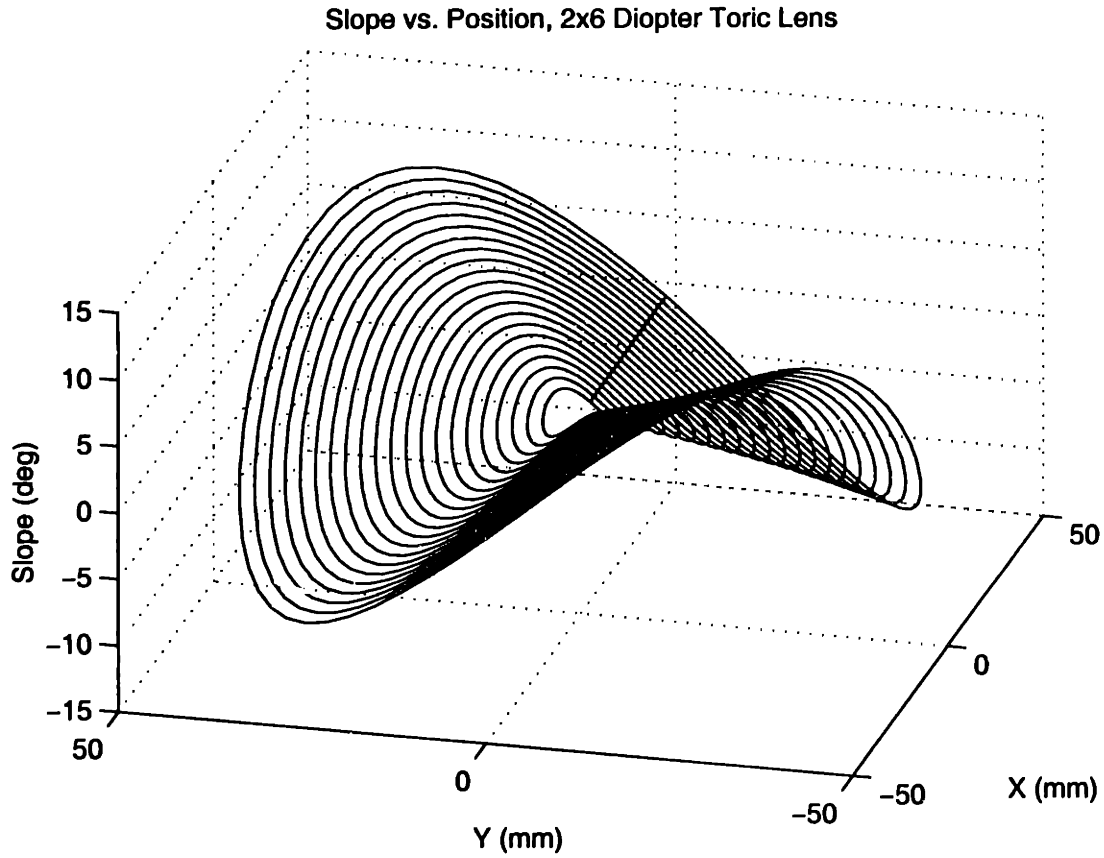

Figure 4-9: Slope profile of a typical toric lens.

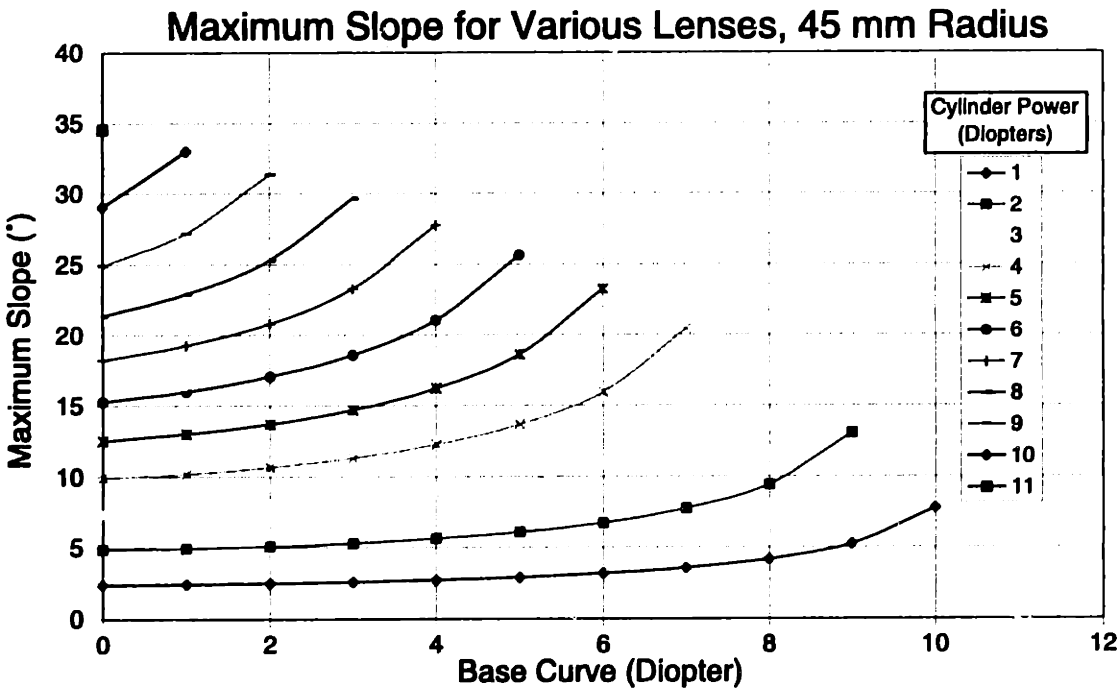

Figure 4-10: Maximum slopes of different lenses, 45mm radius.

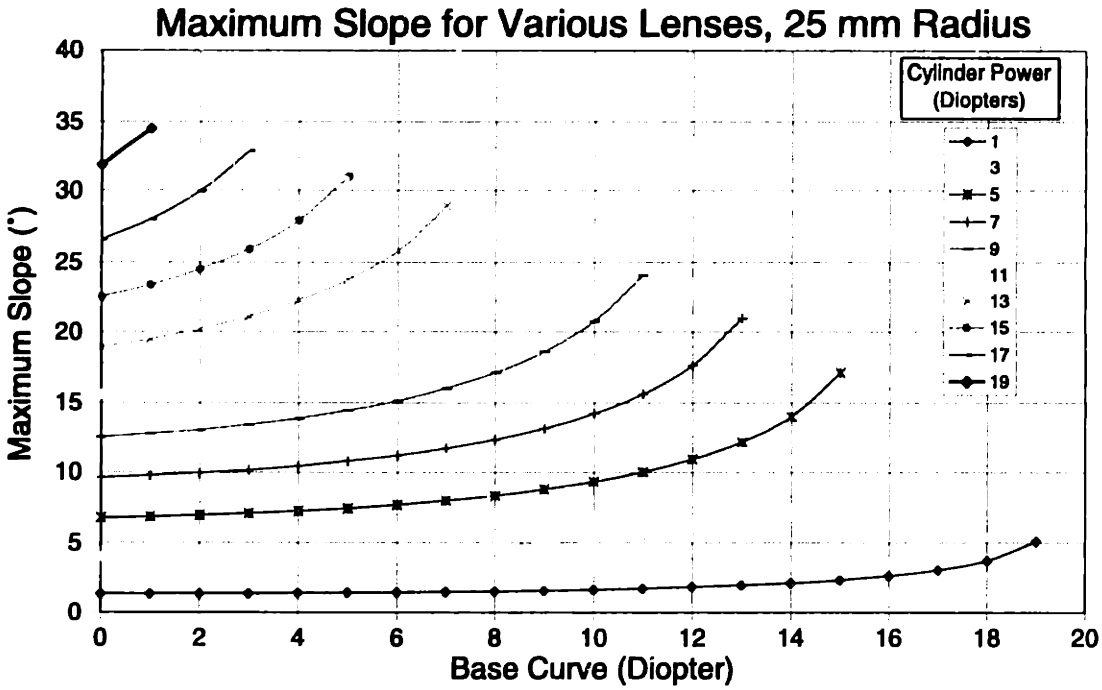

Figure 4-11: Maximum slopes of different lenses, 25mm radius.

4.3.3 Clearance Volume

The clearance volume available for the toolarm can be established by examining the possible lens interference for a variety of machine configurations. Ideally, a set of curves should be produced that form the boundary of the volume the toolarm can occupy. These curves can then be overlayed over the design of the toolarm, and the possibility of interference easily determined. The design can then be changed so that it never intersects these curves. It is important to realize that the interference of the lens and toolarm is determined by how the lens moves *relative* to the toolarm, not in absolute space. Note that both the lens and toolarm are moving.

An analytic approach could certainly be developed to describe the geometry of the lens, and how the toolarm must move relative to it. The possibility of interference could then be determined. A basic approach for this was performed in Section 4.3.1, which examined the maximum interference of the tool with one point. However, the material in Section 4.3.1 is not as useful for constraining the geometry of the toolarm, because the relationship between the toolarm and the lens is not well established

visually, preventing overlay curves of interference from being generated. Further effort could be expended to generate these curves analytically, but more direct methods are available.

Utilizing mechanical kinematics software, it is possible to easily generate the required curves. Pro/MECHANICA[1] is one such software package, containing software for mechanical and thermal finite element analysis, as well as motion simulation. Pro/MECHANICA allows the user to enter a three-dimensional model of the geometry and establish the kinematic relationships graphically. The program then produces the equations of motion as C-code, compiles them with a suitable compiler[2], and simulates the motion event. Interference curves can then be generated graphically in Pro/MECHANICA using a "pen and paper" approach. Points of interest on the lens, which are possible candidates of interference, such as the corners, can be selected as "pens". The "paper" can then be selected as the body representing the toolarm. As the motion simulation is performed, the "pens" will trace out curves in the coordinate frame of the toolarm. These are the desired interference curves. These graphics can then be saved as DXF or IGES files, and imported into most MCAD programs for overlay on the toolarm geometry to determine possible interference. Figure 4-12 illustrates a typical simulation.

By iterating this process for different lens configurations and toolarm-spindle relationships, a set of curves can be established for comparing the effect of the different kinematic arrangements on the toolarm interference. This is done in Figure 4-13, where the "initial offset" is the angular position of the toolarm when cutting the outermost edge of the lens, before the tool extends into the workpiece. By utilizing these curves in the initial toolarm design, decisions can be made regarding the tradeoffs between arm geometry and lens cutting capability.

[1]Available from Parametric Technology Corporation, Waltham, MA 02453 Tel: (781) 398-5000, http://www.ptc.com

[2]In this case, Microsoft Visual C++ ver. 5.0, Microsoft Corporation, Redmond, WA 98052 Tel: (425) 882-8080, http://www.microsoft.com

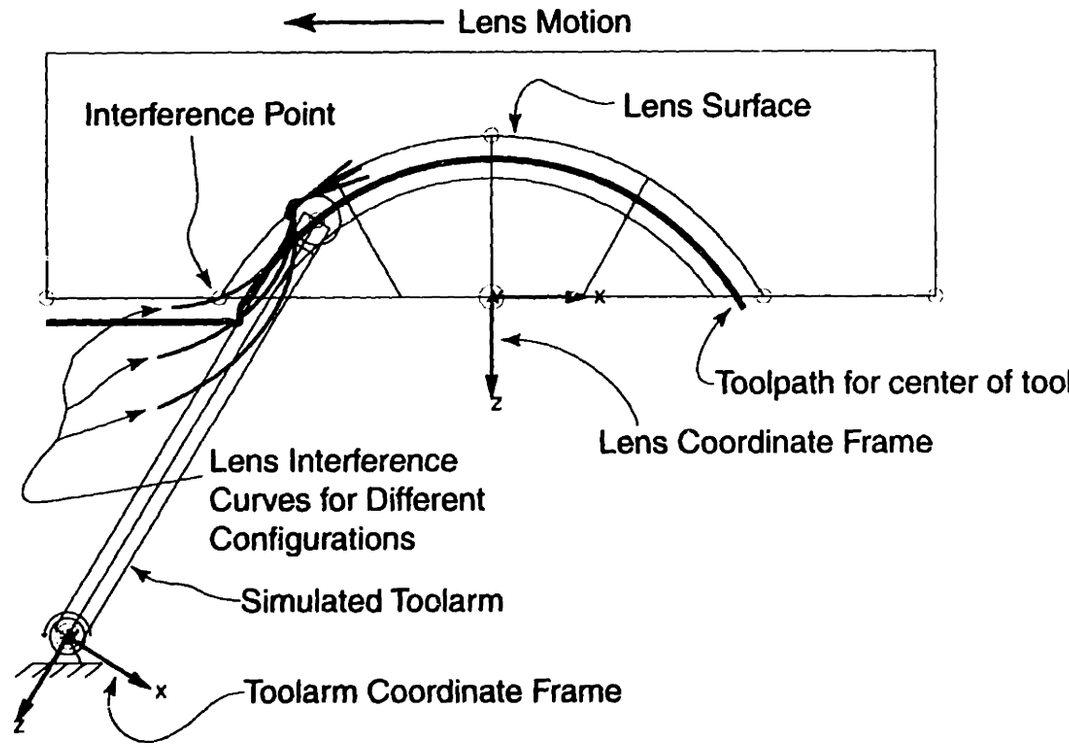

Figure 4-12: Typical Pro/MECHANICA simulation of toolarm-lens interference, 10 diopter lens.

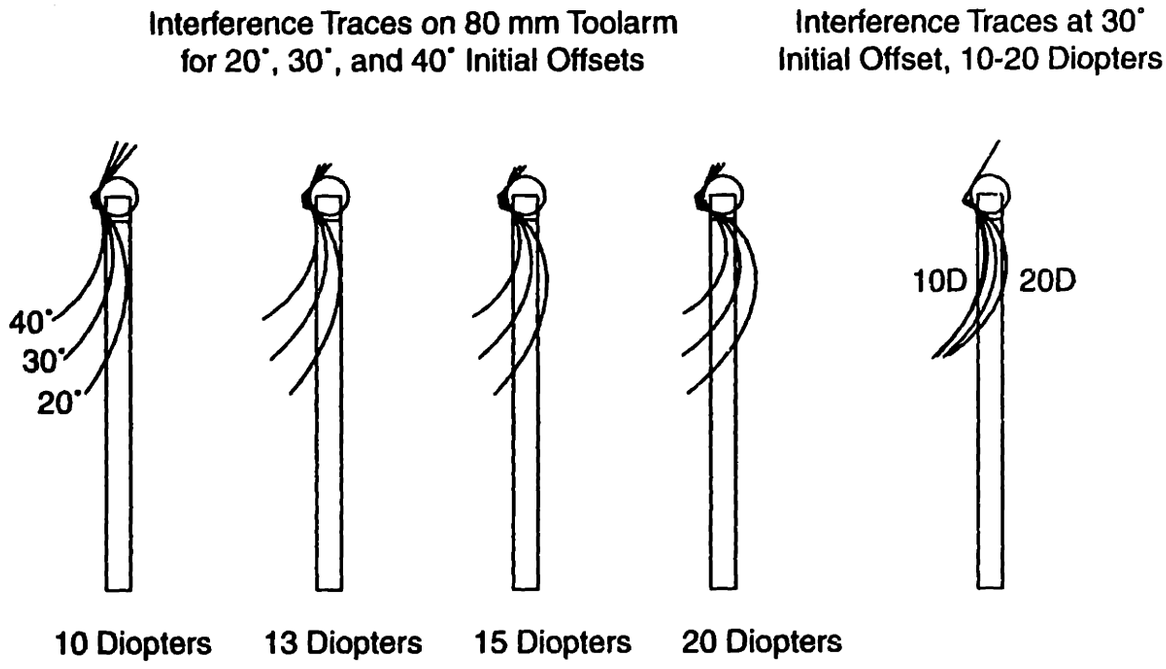

Figure 4-13: Comparison of interference effects on different toolarm configurations.

4.4 Inertia Minimization

Another consideration in the design of the toolarm is that the total rotary inertia of the system must be minimized. This is important for two reasons. The first comes from the fundamental relationship between the torque acting on a body, its associated rotary inertia, and the angular acceleration of the body:

$$T = J\alpha \tag{4.16}$$

Note that in this design, T is the available torque of the motor, which is the output torque of the motor minus any load torques from cutting forces, while J is the total rotary inertia of the FTS, including the motor inertia, coupling, and the toolarm and tool shaft. It is then easily seen that adding any additional rotary inertia to the system through the toolarm will directly limit the maximum attainable acceleration of the toolarm in a direct inverse relationship

$$\alpha = \frac{T}{J} \tag{4.17}$$

However, given the large torque of the Aerotech BM1400 servomotor used on the FTS, a second reason is of even greater importance. This is the effect of the toolarm inertia on the control performance of the FTS. Figure 4-14 shows a lumped parameter model of the FTS system. Here, J_m is the rotary inertia of the motor, J_t is the rotary inertia of the toolarm, shaft, and tool, and K is the lumped torsional stiffness of the flexible coupling and shaft ends (Note the Gam-Jakob bellows coupling utilized here is so torsionally stiff that the compliance of the stub shafts at the motor and tool shaft become an issue, see Ludwick[12]). θ_1 and θ_2 are the angles of the motor and toolarm, respectively. Applying Equation 4.16 to each inertia

$$J_m\ddot{\theta}_1 = T - K(\theta_1 - \theta_2) \tag{4.18}$$

$$J_t\ddot{\theta}_2 = K(\theta_1 - \theta_2) \tag{4.19}$$

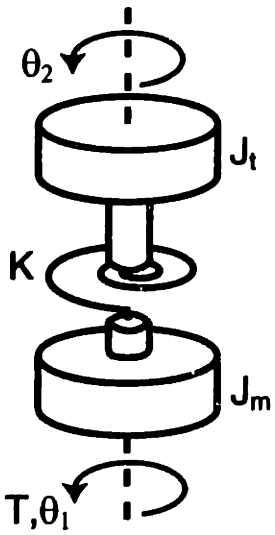

Figure 4-14: Lumped parameter inertia model of the FTS system.

Applying the Laplace Transformation to these equations, and substituting one into the other, the transfer function from the torque input T to the output θ_2 can be determined as

$$\frac{\theta_2(s)}{T(s)} = \frac{K/(J_t J_m)}{s^2(s^2 + \frac{K(J_t+J_m)}{J_t J_m})} \tag{4.20}$$

Thus the plant model of this system has two poles at the origin, as might be expected from a model of a free inertia. However, there are two additional undamped poles, resulting from the torsional resonance of the second inertia through the coupling. By noting this is a polynomial of the form $s^2 + \omega_n^2$, the natural frequency w_n can be found

$$\omega_n = \sqrt{\frac{K(J_t + J_m)}{J_t J_m}} \tag{4.21}$$

For control purposes, it is important to push the natural frequency of these poles as high as possible. This will enable the maximum closed loop control bandwidth to be obtained with conventional control techniques. While control algorithms do exist to work around such problems, it is always desirable to have as "clean" a plant as possible. A sufficiently high natural frequency will allow a simple notch filter to be effective at preventing the resonance from destabilizing the control loop, without any

more complicated control methods. Hence the quantity

$$\frac{J_t J_m}{J_t + J_m} \tag{4.22}$$

should be minimized. In the range where J_t and J_m are comparable, the direct factor of J_t in the numerator will have a large effect on this quantity, and the reduction of J_t, the toolarm inertia, will be important. Note that a similar evaluation of the natural frequencies could be developed by forming stiffness and inertia matrices K and M, and solving the generalized eigenvalue problem $K\phi = \lambda M\phi$. This would produce exactly the same result for the natural frequencies.

4.5 Stiffness

Stiffness is paramount in the support of any cutting tool. Cutting forces, as well as acceleration forces from the RFTS, provide loads to the toolarm carrying the cutting tool. These loads can induce deflections in the toolarm, changing the location of the cutting tool and inducing errors in the workpiece. The toolarm must be stiff to both these static and dynamic forces in order to produces accurate lenses.

In the following sections, I consider the forces produced by the cutting process. Acceleration forces can be modeled later with finite element analysis. In any case, I expect the acceleration forces to be somewhat lower in magnitude than the maximum cutting forces. For example, one can consider the forces needed to accelerate a shanked diamond tool as used on the final toolarm design. These tools have a mass of about 0.010 kg; using Newton's law of $F = ma$, it appears that only $\sim$ 5 N of force is needed at the arm tip to accelerate the tool at 50 g. This is much less than the maximum cutting forces noted below. A stiff, inertia minimizing arm design should also mimimize the effect of acceleration, since the bulk of the mass will not be traveling on a high acceleration path. This is one benefit of the RFTS topology.

Material	Cross Feed (μm/rev)	Depth of Cut (mm)	Cutting Forces (N)			
			Tangent	Normal	Crossfeed	Total
CR39	50	1	8.5	6	1.25	10.5
CR39	100	1	7.5	5	0.75	10
CR39	200	1	6	3	0.7	11.5
CR39	50	2	11	7	2.5	13.9
CR39	100	2	10	6	1.5	13.7
CR39	200	2	8	3.9	1.2	17
Polycarbonate	100	1	25	11.5	2.65	30
Polycarbonate	200	1	45	16	3.25	47.5
Polycarbonate	400	1	72	20	3.25	77
Polycarbonate	100	2	45	14.5	4.5	50
Polycarbonate	200	2	76	17	3.9	80
Polycarbonate	400	2	130	27	6	140

Table 4.1: Approximate cutting forces, 1200 RPM spindle speed. From Ludwick[12].

4.5.1 Static Stiffness

Any loading of the toolarm which occurs at frequencies well below the natural frequencies of the toolarm can be considered static for the purposes of the design. The magnitude of this loading can then be applied to the structural design in a static analysis, and the maximum deflection of the toolarm under this loading determined. Any deflection of the toolarm under this loading will of course directly translate into errors in the workpiece, as the tool is moving from its desired position. Given a good understanding of the loading on the tool, the design can be optimized to limit these effects. Cutting forces in turning operations can very greatly depending on the cutting parameters: workpiece material, depth of cut, cross feed rate, and the tool edge condition. Ludwick[12] has performed a characterization of the cutting forces, using a currently available commercial lens turning machine. Excerpts of this data are presented in Table 4.5.1.

Examining this data, it appears polycarbonate lenses will be significantly more challenging to cut than the CR39 lenses. However, since polycarbonate lenses make up an increasing proportion of the eyeglass lens market, due to their light weight and shatterproof nature, they must be easily cut by this machine. Of particular concern are the surface normal cutting forces, since deflection of the toolarm in this direction

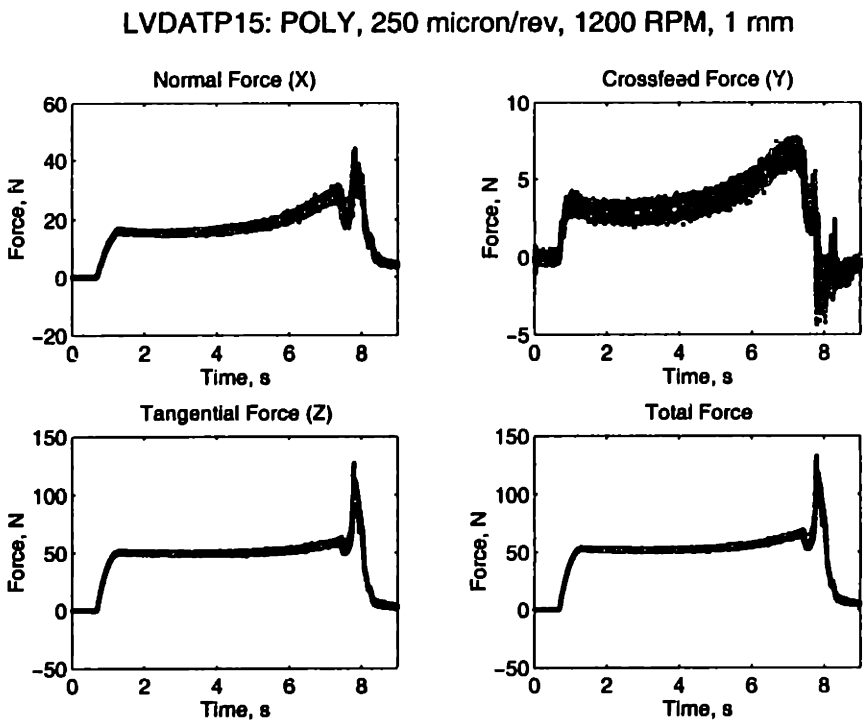

Figure 4-15: Typical force trace for a cut in a polycarbonate lens (1 mm depth of cut at a feed of 250 μm/rev). From Ludwick[12].

will cause an equal error in the lens surface. The tangential cutting forces, or forces in the direction of the cutting velocity, would not normally be a concern, since any deflection only induces "cosine" errors. Even in the center, the tool height adjustment would account for the deflection, and eliminate the center defect. However, the difference in cutting force behavior between the polycarbonate and CR39 materials creates a problem. Polycarbonate lenses produce much higher cutting forces near the center of the part, and in fact the cutting forces increase toward the center, as shown in Figure 4-15. If this force causes a tool arm deflection which is significant in relation to the desired center defect size, the same tool height setting will not be able to produce accurate lenses in both polycarbonate and CR39, requiring a recalibration of the machine. Thus the toolarm should be stiff to both normal and tangential cutting forces.

4.5.2 Dynamic Stiffness

Dynamic stiffness at the cutting tool is also important. Those familiar with conventional machining practice will recognize the condition of tool "chatter", caused by the excitation of the tool at its natural frequencies, and the associated poor surface finishes produced in the workpiece by the vibrating tool edge. Given the accuracy requirements of the RFTS, imperfections in the surface which may be regarded as surface roughness in conventional machining, on the order of several μm, may be regarded as errors in form for our machine. Therefore it is essential that the toolarm provide enough dynamic stiffness to prevent tool chatter or vibration during the lens cutting process.

Referring again to the data collected by Ludwick[12], it appears that cutting the polycarbonate lenses will not present a problem for the dynamic stiffness of the toolarm, as the cutting forces, while large, are dominated by lower frequency content. In contrast to the static stiffness case, cutting CR39 lenses could present more of a problem than polycarbonate lenses to the dynamic stiffness. As Ludwick notes, the large frequency spectrum of the CR39 lenses, while lower in magnitude, presents a white noise input to the machine. The higher frequency content could excite the toolarm if care is not taken in the design. Figure 4-16 illustrates the frequency content of a typical high-feedrate cut in CR39; the peaks shown in the response can be reduced somewhat by lower feedrates. The approach taken in the design should be to push the natural frequency of the first mode of vibration as high as possible, minimizing the possibility of it being excited by cutting forces. These results for the actual toolarm are presented in Section 7.3.4.

4.6 Tool Height Adjustment

Perhaps the most challenging functional requirement of the FTS toolarm is the requirement for integrated tool height adjustment. Adjustment of the tool height, or providing tool motion in the direction orthoganol to the cross slide axis and the spindle axis, is absolutely essential to producing accurate lenses. The tool height is not

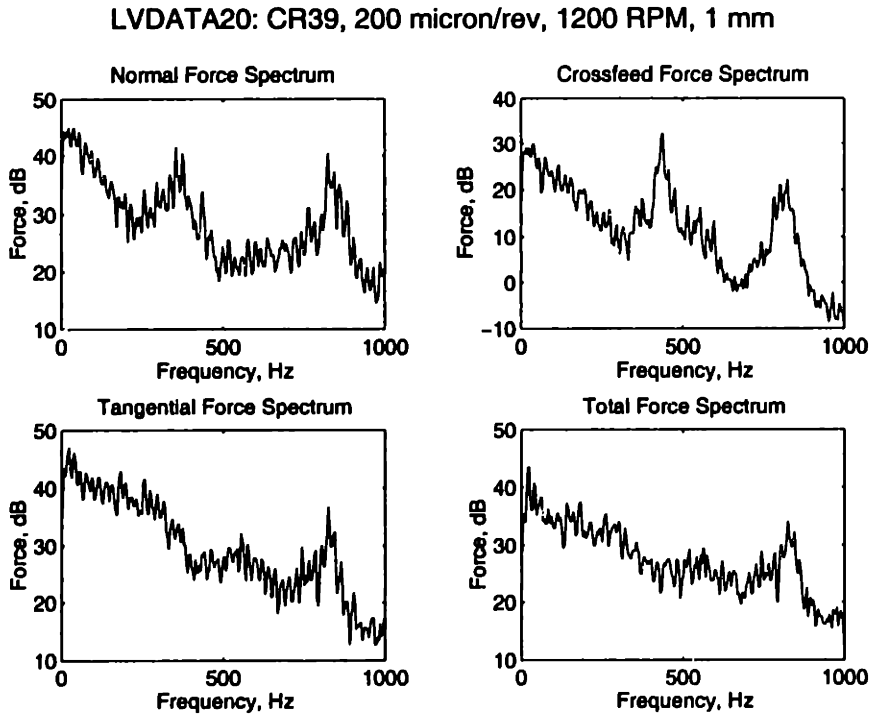

Figure 4-16: Frequency components of a high feedrate CR39 force trace (1mm depth of cut at a feed of 200 μm/rev). From Ludwick[12].

critical over most of the workpiece, producing only "cosine" error, or error which deviates from the desired value as the value of the cosine deviates from one when the input angle is perturbed about zero. However, any error in tool height will produce a defect in the center of the part, as the tool will be unable to physically cut in the center of the part, as shown in Figure 4-17. The radius of the expected defect in the center can be expected to match the error in the tool height, but the height of the defect is difficult to predict. In theory, it could extend to the original height of the lens before cutting, but the nature of the cutting process (fracture, etc.) will prevent defect heights of this magnitude in practice.

Implementation of a tool height adjustment to eliminate center defects will be difficult in light of the other functional requirements. Any added mechanism must by necessity add mass to the tool arm, thereby increasing the rotary inertia; any mechanism allowing movement of the tool will also likely add compliance, and thus lower the stiffness. This problem is challenging enough that Chapter 5 is dedicated to conceptual designs for solving this difficulty. These conceptual designs will require a

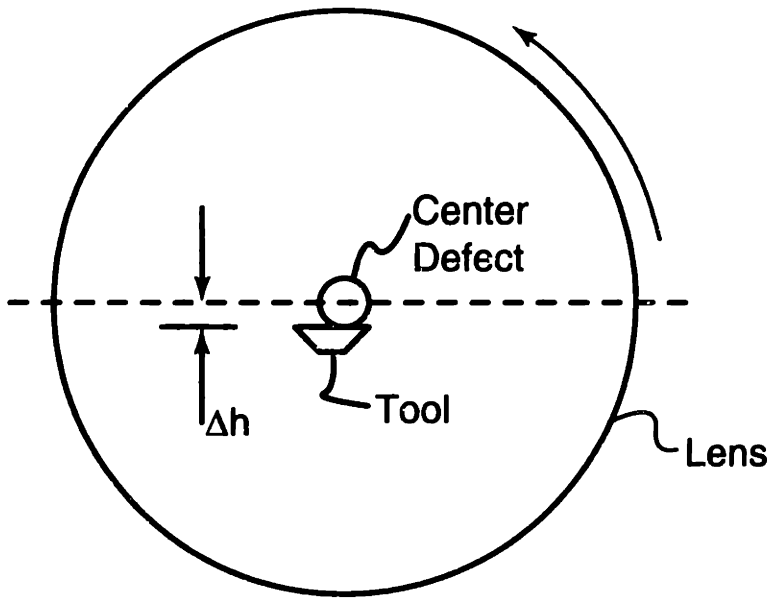

Figure 4-17: Center defect caused by tool height misalignment Δh.

firmer specification of this functional requirement to be developed fully. In particular, the desired range of travel and the resolution of the mechanism need to be determined.

The resolution of the system is the easier of the two parameters to specify. The resolution is easily set by the desired maximum defect size. If the maximum defect radius is specified to ± 1 μm, then the resolution of the adjustment needs to be < 1 μm. The range of travel is a bit more difficult to specify precisely. The necessary range will vary, depending on how well the toolarm can be initially mounted with respect to the spindle, the variation in tool heights from the manufacturer, and on the repeatability of the tool replacement. If the desired range of travel is quite large, it may be necessary to split the adjustment into two mechanism, one "large" adjust to bring the tool into the range of the "fine" adjust, which will eliminate the center error. As a starting point, one can examine the tool height adjustment mechanisms on the diamond turning machines at Lawrence Livermore National Laboratory[3]. One design there uses a hydraulic "microjack", in which a micrometer pushes hydraulic fluid to activate a diaphragm and flexure mechanism. This provides a total range of travel of 25 μm. Unfortunately, this design is too bulky and has too much mass to be adapted to our system. A good starting point for this design would be to specify that the minimum range of travel for a fine adjustment mechanism equal this 25 μm.

Chapter 5

Design Concepts for a Rotary Toolarm

Conceptual design is the second stage in the evolution of a component or product. Once the task has been well defined in terms of the functional requirements and design parameters, as in Chapter 4, the designer has the framework necessary to create conceptual designs. Every designer will rely heavily on a "toolbox" of favorite parts and solutions to problems, but one should not be restricted to just the elements in this personal database. It is vitally important to attempt an open-minded, "clean sheet of paper" approach in the initial conceptual design. It is only in this manner that "new parts" and approaches can be developed and stored in a designer's toolbox. Such efforts may seem fruitless, as the most conventional designs are often those chosen for manufacture. Economics often plays a large role in this, and there is no need to reinvent the wheel. If novel approaches and techniques are to be developed, however, this practice is required in every design.

The rest of this chapter documents much of the conceptual design for the rotary toolarm, focusing on the technologies needed to provide sub-μm resolution height adjustment. This is one of the most difficult challenges in the design of the structure and one of the most crucial to its successful operation. Such conceptual work is not often documented, but it is important here for several reasons. The final design developed here was chosen on standards of manufacturability, cost, etc. which were

appropriate for a prototype research machine. If the RFTS is implemented in a production machine, these standards may change and another concept may be more appropriate.

Several considerations have been kept in mind when developing adjustment concepts. Placement of the actuation system near the rotary axis of the toolarm would greatly reduce the rotary inertia added to the system, but with possible consequences on adjustment accuracy. The applied moments due to disturbance forces are largest at the base, due to the lever action of the arm, and the actuation system would need to bear these. This lever arm will also magnify any change in position of the actuator, in an "Abbe error" effect. Placement at the end of the arm would help minimize these problems, but with the considerable increase in rotary inertia, along with possible packaging problems (geometric constraints). Elastic deformation of the entire structure is another option, but may limit the total amount of travel, as well as compromise the stiffness of the structure to disturbance forces. Each of the concepts considered is presented in the sections which follow.

Concept 1

The first conceptual design incorporates a flexure at the end of the toolarm, as shown in Figure 5-1. The flexure at the end allows the vertical placement of the tool. The actuation is provided by a pin on a torsion bar, which rides in a slot in the flexure. The torsion bar is turned by a worm gear in the base, which is closer to the rotation axis, allowing more space for the gears and minimizing inertia. In this design, the tool height should only be adjusted in one direction, so there is no chance of cutting forces overcoming the preload of the torsion bar. Difficulties with this design would include obtaining a torsion bar with sufficiently high spring rate, and making the flexure sufficiently stiff against off axis motions.

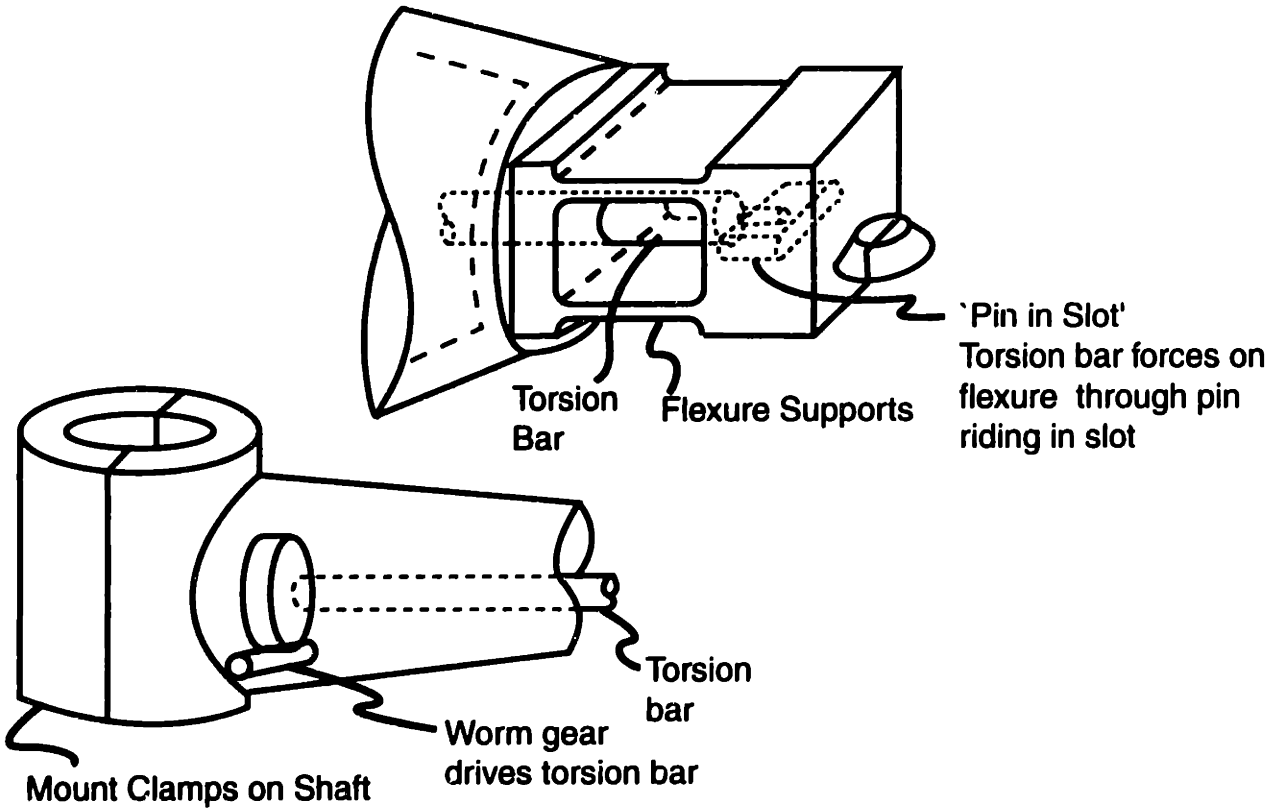

Figure 5-1: Concept 1 - Flexure at end of arm and torsion bar design.

Concept 2

This design moves the flexures from the tip of the tool to the base, as illustrated in Figure 5-2. The flexures are designed to provided translational motion in the vertical direction. A fine-pitch screw adjusts the height of the tool. Unfortunately, it is likely to be very difficult to properly locate the screw for driving this flexure stage. With the position of the actuator shown in the figure, the screw can induce pitch error in the flexural mounts. The lever action of the arm will then magnify this pitch error into displacement error at the tip, possibly negating the effects of the fine-pitch! The height could then be difficult to adjust to the required resolution.

Concept 3

Figure 5-3 presents a design which uses the toolshaft as a linear bearing surface. By adjusting the preload in the clamping screws, the bearing can be adjusted from a complete frictional restraint during operation to a sliding contact bearing for adjusting

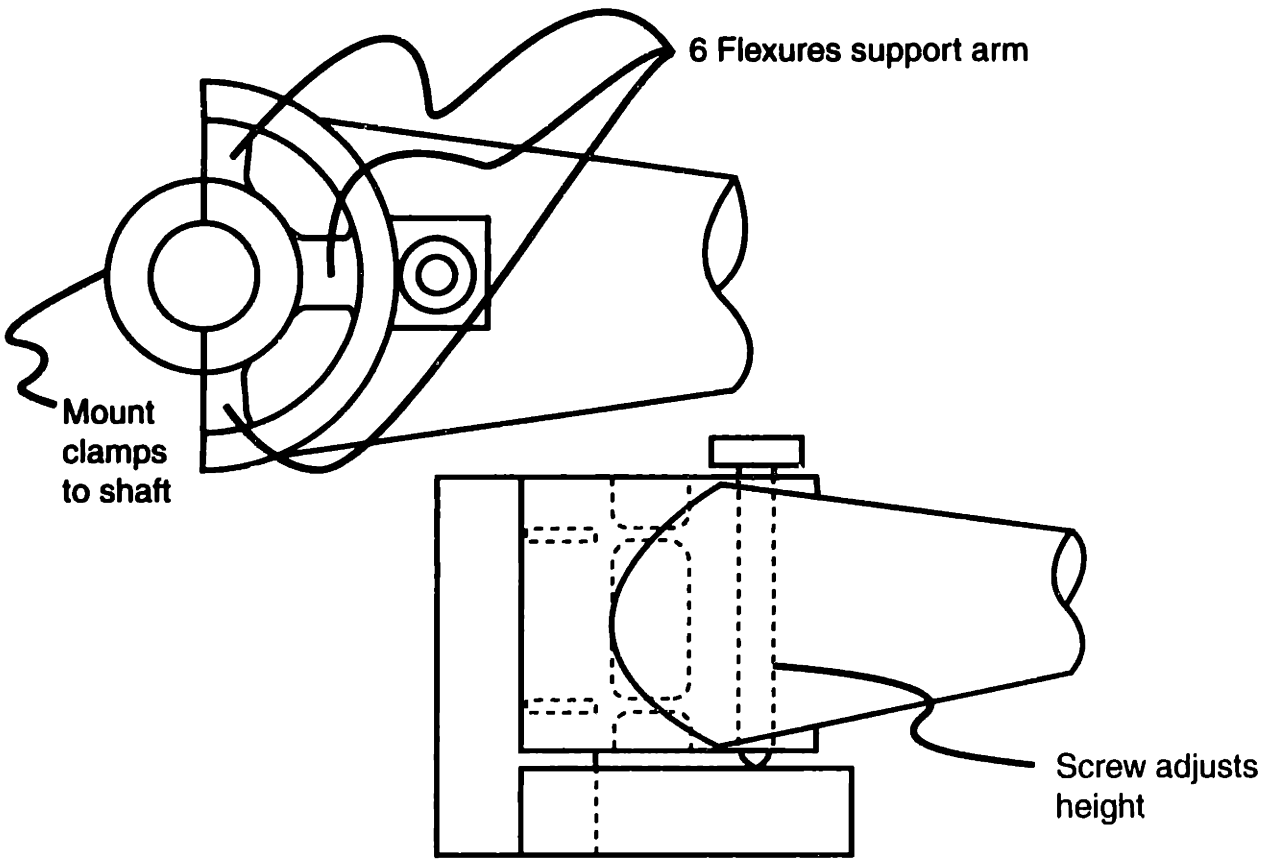

Figure 5-2: Concept 2 - Flexure at base design.

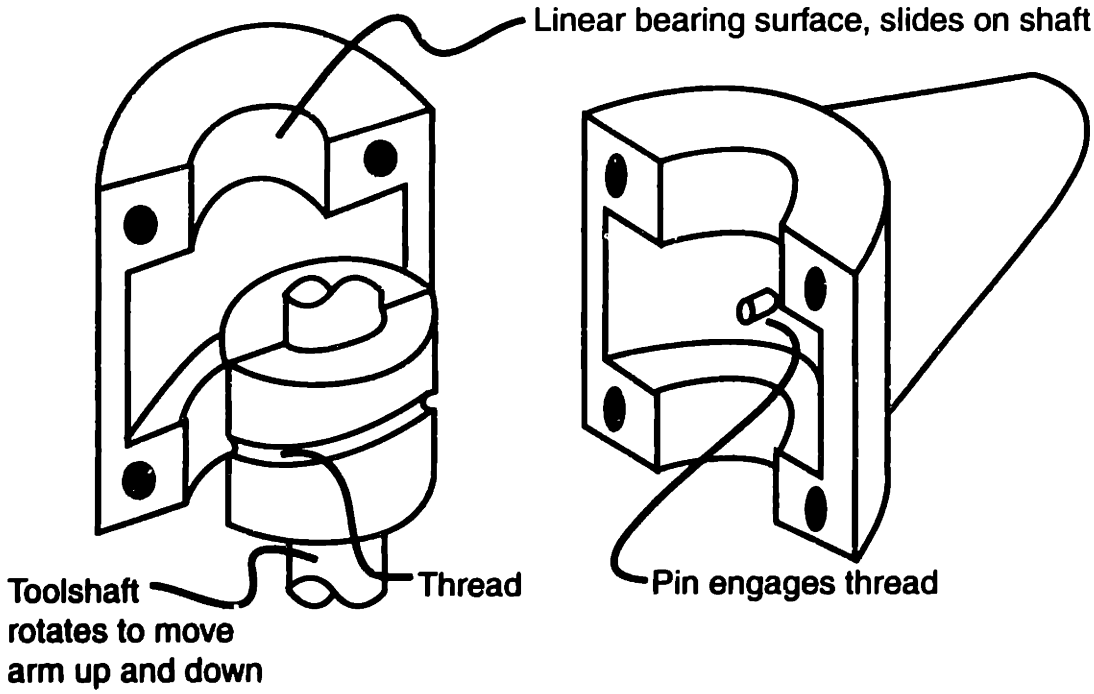

Figure 5-3: Concept 3 - "Pin in thread" with linear bearing design.

tool height. Movement of the toolarm vertically can then be accomplished by constraining the toolarm rotationally, but not vertically, and then rotating the tool shaft. A pin on the toolarm rides in a slot on the toolshaft, which provides a screw action to move the toolarm. Since the toolshaft servo has very high rotational resolution, fine adjustment of the toolarm height should be adjustable over a long range. Disadvantages include a reliance on the toolshaft as a good bearing surface, reliance on an operator to adjust the bearing properly, and the likely loss of calibration information on the rotational angle of the toolarm during the adjustment process.

Concept 4

Sliding contact linear bearings are used in this design, but now they are integrated into the toolarm, as opposed to relying on the surface of the tool shaft. Two different configurations are illustrated in Figure 5-4. The final choice is likely due to manufacturing considerations. The gibs may not need to be locked into position, if the height adjustment screw provides sufficient stiffness to cutting forces. The siiding contact interface may serve to damp toolarm vibrations. If carefully manufactured, rotational

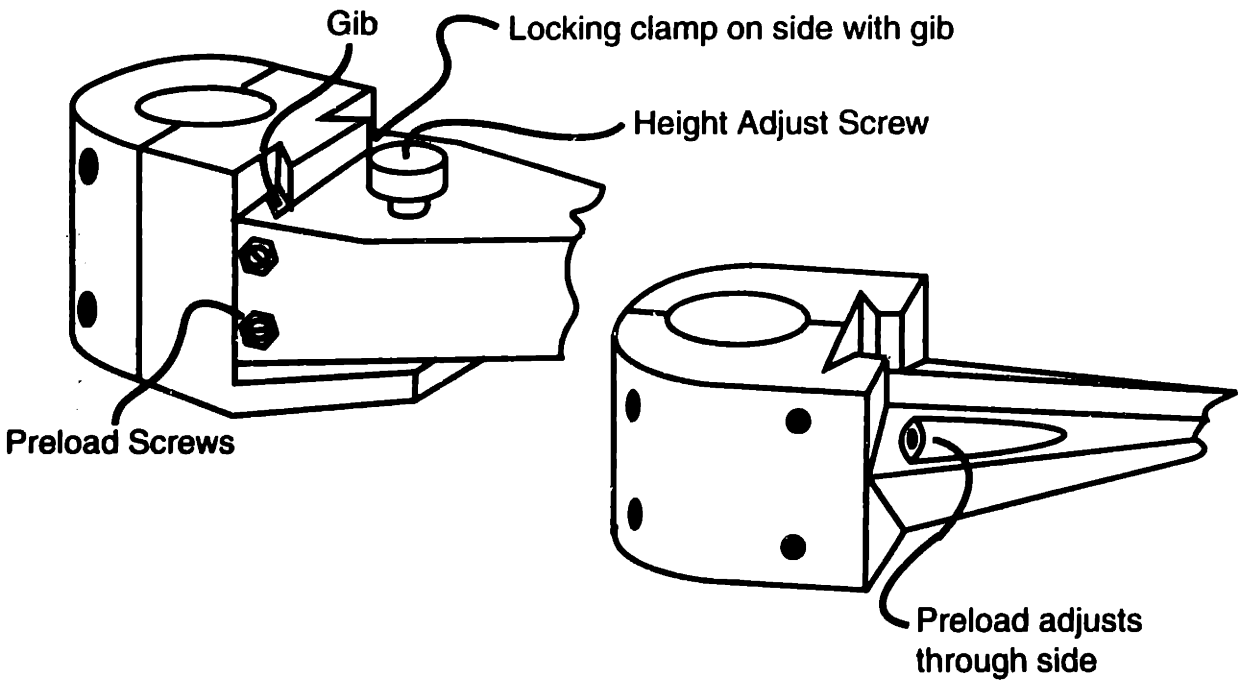

Figure 5-4: Concept 4 - Linear bearings, external to shaft.

angle calibration information for the toolarm may be retained while the tool height is adjusted in this design, but the cost of such precision fabrication will be expensive.

Concept 5

Similar to Concept 3, this design attempts to remove the operator skill needed for adjusting the bearing preload. As shown in Figure 5-5, this design forms a properly preloaded bearing with the main clamps, which should be adjusted at the factory. The gibs can then be adjusted in an "on-off" fashion to lock the toolarm in place. This design could use the pictured screw to adjust tool height, or it could use the pin and servomotor technique from Concept 3. Rolling element bearings are shown, but the design could be adapted to work with the sliding contact bearings shown earlier. As this concept releases the interface with the toolshaft, there is still a problem with a loss of rotational position information during adjustment.

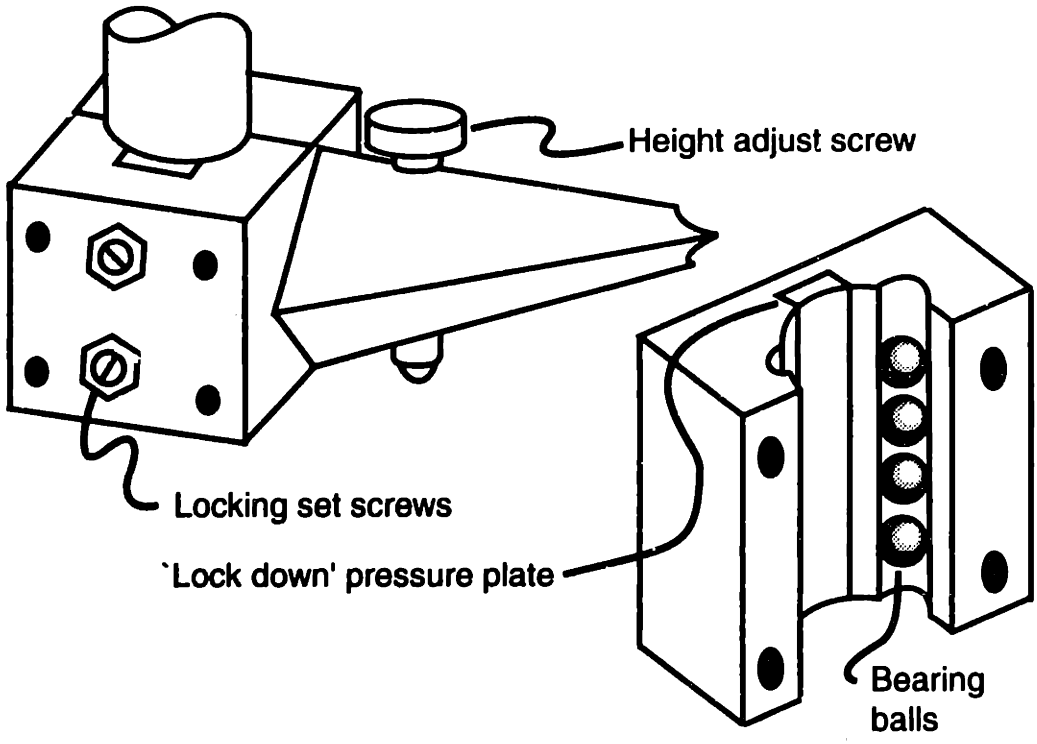

Figure 5-5: Concept 5 - Linear ball bearings.

Concept 6

This concept, rather than the utilizing linear motion of the previous design, implements rotary motion instead, as shown in Figure 5-6. The rotational tilt of the arm approximates linear motion at the end, in much the same way that the rotational acceleration of the RFTS approximates linear acceleration. Unfortunately, as the angles of displacement become larger, the pitch of the tool will result in different heights along the radius of the tool. This may not be problematic if the same edge of the tool is used while cutting in the center; this would require all lenses to have similar center depths, so that the arm is in the same final angle at the center. High grade ball bearings or rotational flexures provide the angular motion. Actuation could be provided by a worm gear drive, or by directly pushing on the end of the arm with a micrometer, then locking the arm in place. With proper design, this concept could retain the other calibration settings for the RFTS after adjustment.

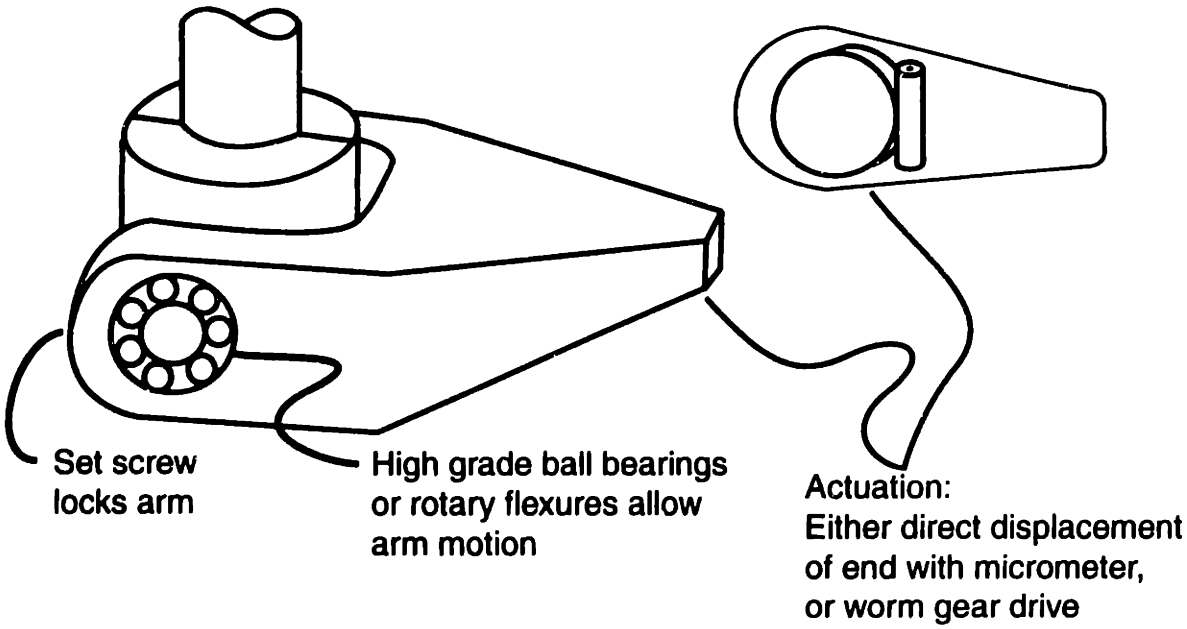

Figure 5-6: Concept 6 - Rotary bearing system.

Concept 7

Concept 7, presented in Figure 5-7, illustrates some alternate drive mechanisms for the linear bearing examples shown earlier. These may be appropriate if problems arise with the fine-pitch screws that were often shown in previous designs. In example (a), a capstan drive is actuated by a worm gear. This method can achieve a very high reduction of the motion for good resolution. The capstan rides on the tool shaft or other bearing surface and would need to be properly preloaded. In example (b), the wedge reduces the motion of the screw. Wedges can be built with much smaller inclines than the typical screw for better reduction, and when combined with a coarse screw can provide higher forces that fine-pitch screws can provide. Many manufacturers claim their fine-pitch screws have limited load capacity due to the fine threads; this is discussed in more detail in Section 6.3.1.

Concept 8

As shown in Figure 5-8, the tool can be adjusted using a hydraulic jack. Hydraulic jacks have been successfully used as tool height adjusters in other precision turning

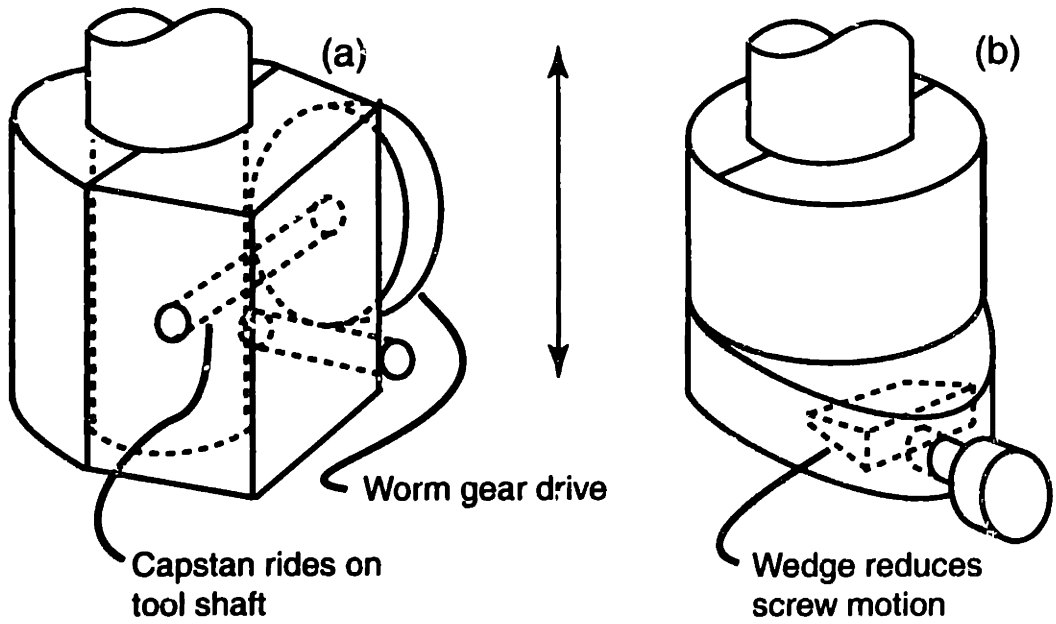

Figure 5-7: Concept 7 - Alternative actuation systems for linear bearings.

machines[3]. The use of an essentially incompressible fluid allows very stiff actuators to be formed which have very high reductions when compared to mechanical transmissions. The transmission ratio is a simple function of the ratio of the areas of the actuating plunger and driven plunger. This design allows much of the actuation mechanism to be located off of the toolarm. However, it would then need to be connected to the toolarm with a hose coupling, which would prevent the toolarm from rotating outside a limited angle, and the hose would introduce compliance into the actuator. This design depends on one of the linear bearings introduced earlier, with the consequent possibility of undesired rotational motion. However, if the interface with the arm is designed properly, such motion may be minimized to an acceptable level. Seals at the jack may be eliminated with flexure bellows.

Concept 9

Air bearings provide a rapid clamping/unclamping mechanism in Concept 9, illustrated in Figure 5-9. The toolarm is normally clamped to the toolshaft, but introduction of air into bearing pockets forces the toolarm and shaft apart. The air then

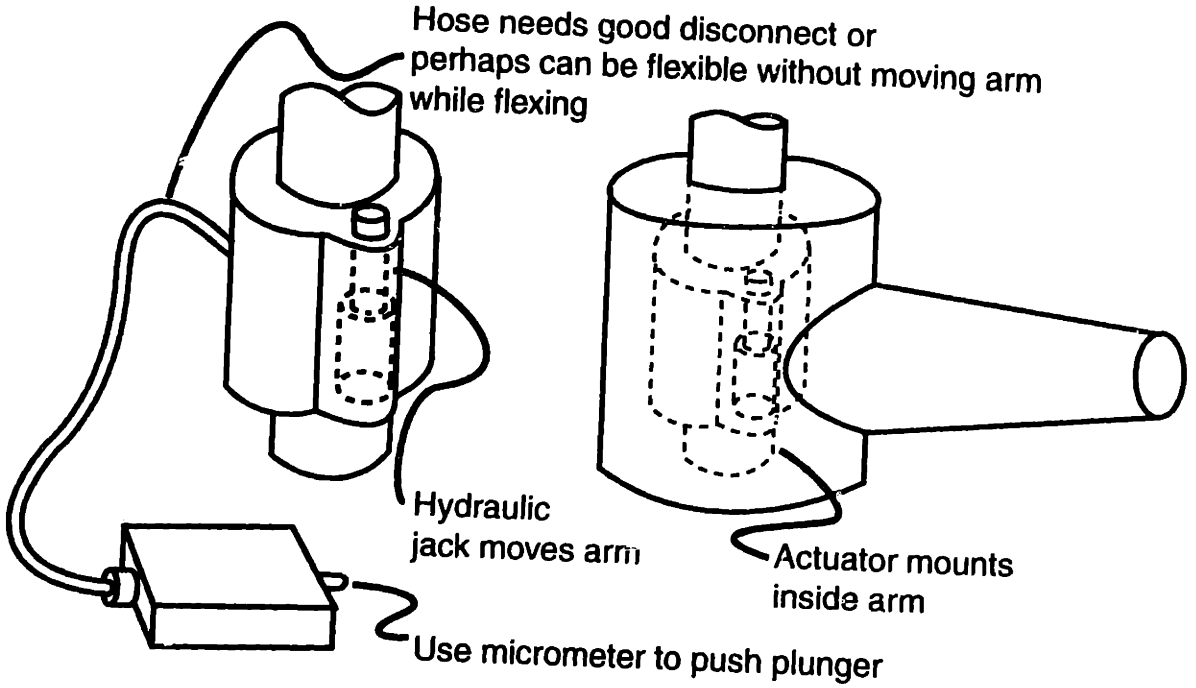

Figure 5-8: Concept 8 - Hydraulic jack with linear bearing.

forms a fluid bearing. This design would depend on having a toolarm material which can undergo sufficient elastic deformation to allow the air pressure to force the two pieces apart, yet be stiff enough to have sufficient clamping when the air pressure is removed. If no additional clamping force is provided, this clamp will have to support both the accelerative and cutting forces provided by the RFTS. Designing such a bearing may prove to be very difficult. In addition, this design will require recalibration of the rotational axis after setting the tool height, since rotational position can be lost when the air bearing is activated. However, the toolarm length should remain constant.

Concept 10

Elastic deformation of the entire toolarm provides tool motion in this concept. There are many possible actuator configurations which can provide such motion; two are pictured in Figure 5-10. High force screw or cable elements can exert a large force on the structure, causing elastic deformation which moves the tool. Such force is preferably applied close to the end, as significant deflection can be achieved when

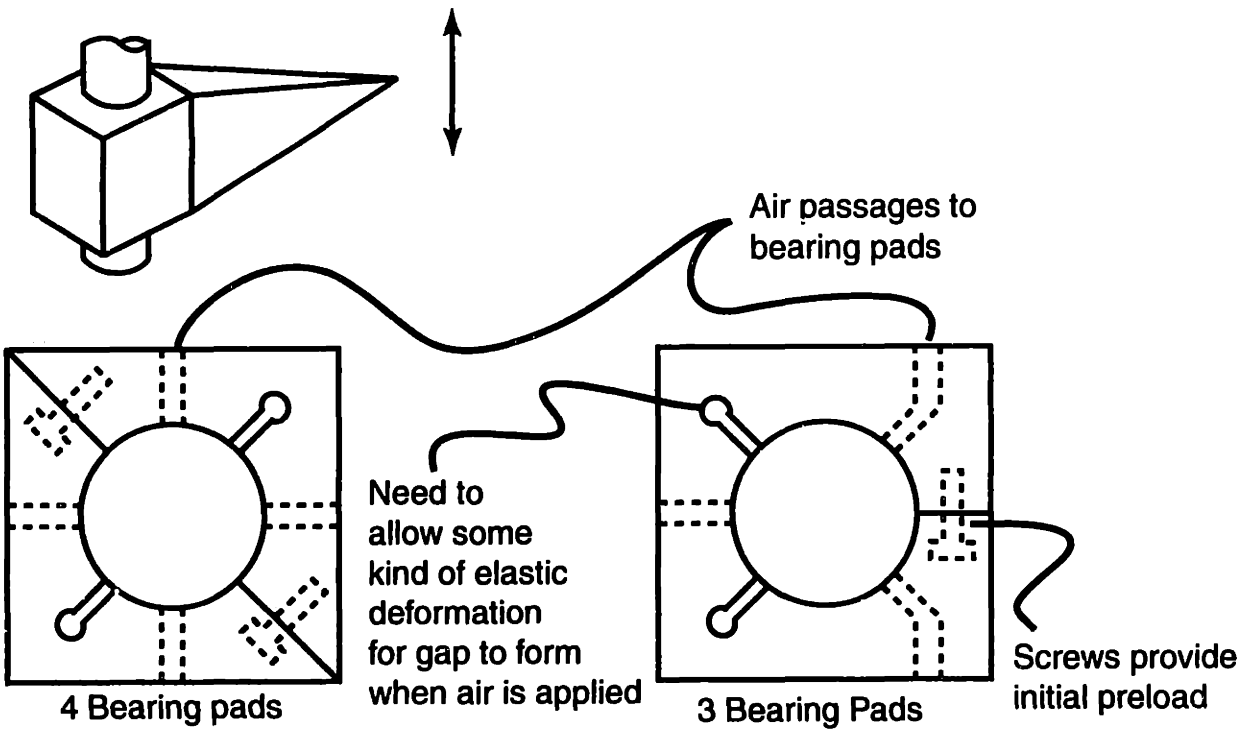

Figure 5-9: Concept 9 - Air bearing.

integrated over the entire length of the arm. For small ranges of travel, these designs have the advantage of requiring little or no additional calibration to compensate for parasitic motion, although for large travels, both toolarm length and rotational position could be affected. The long-term stability of the structure at such high force levels may prove to be one difficulty with the design; another may arise from the high force actuators, which often exhibit "stick-slip" phenomena that makes precise adjustment difficult. In addition, the stiffness of the structure to cutting forces may be unacceptably compromised.

Concept 11

This concept recognizes that the relative height of the spindle and tool need not be adjusted just by moving the tool. Instead, the spindle can also be moved relative to a fixed tool. Figure 5-12 presents two possible methods of adjustment, one using a rotational bearing system, and the other a linear bearing. These designs are ideal in that they decouple one of the functional requirements from the rest of the toolarm,

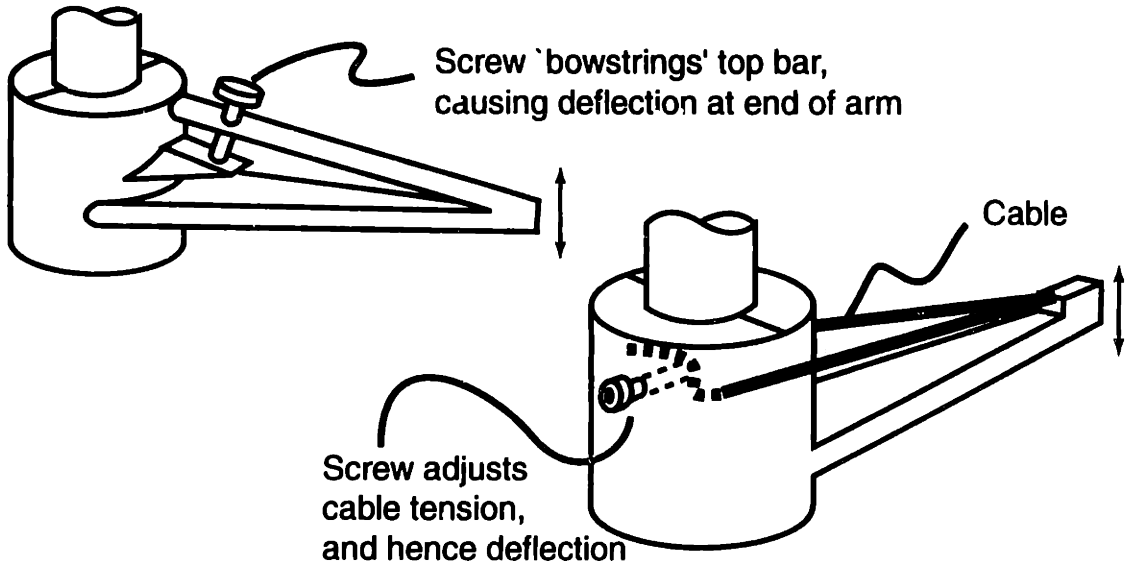

Figure 5-10: Concept 10 - Elastic deformation of toolarm.

releasing constraints and easing toolarm design. However, they both have several difficulties in implementation. In each case, significant parasitic motion can accompany height adjustment. For the rotational system, such motion will certainly occur along the direction of the cross slide axis, but similar motion is also likely to occur in the linear system, given the manufacturing expense necessary to eliminate it at our levels of precision. Such error can easily be removed by changing the cross-slide calibration setting, but the exact setting will require additional effort to determine. Other parasitic motion, such as spindle yaw, is even more difficult to determine and will further increase calibration effort. An additional concern is the load capacity of the air-bearing cross-slide; it already supports the heavy spindle, and the additional support material may be severely weight limited. This has the effect of constraining the stiffness of the spindle support. The dynamic stiffness of the spindle support may be particularly problematic, as not all workpieces will be well balanced.

Concept 12

Concept 12, illustrated in Figure 5-12, features a single flexural pivot at the base, combined with a wedge drive actuator. The wedge drive provides a nice reduction in the motion of any actuator, allowing fine movement. The wedge itself should also try

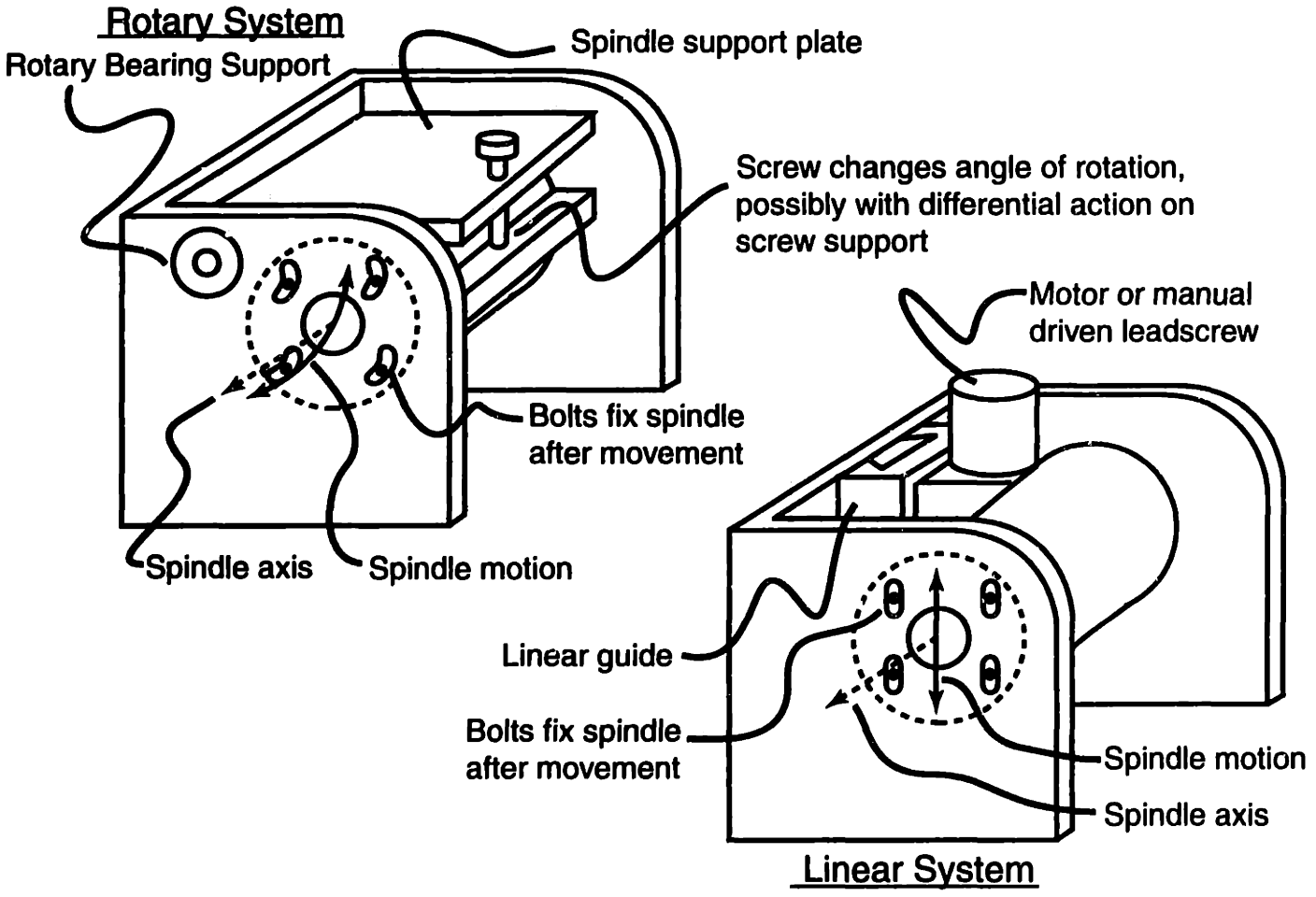

Figure 5-11: Concept 11 - Move the spindle relative to fixed toolarm.

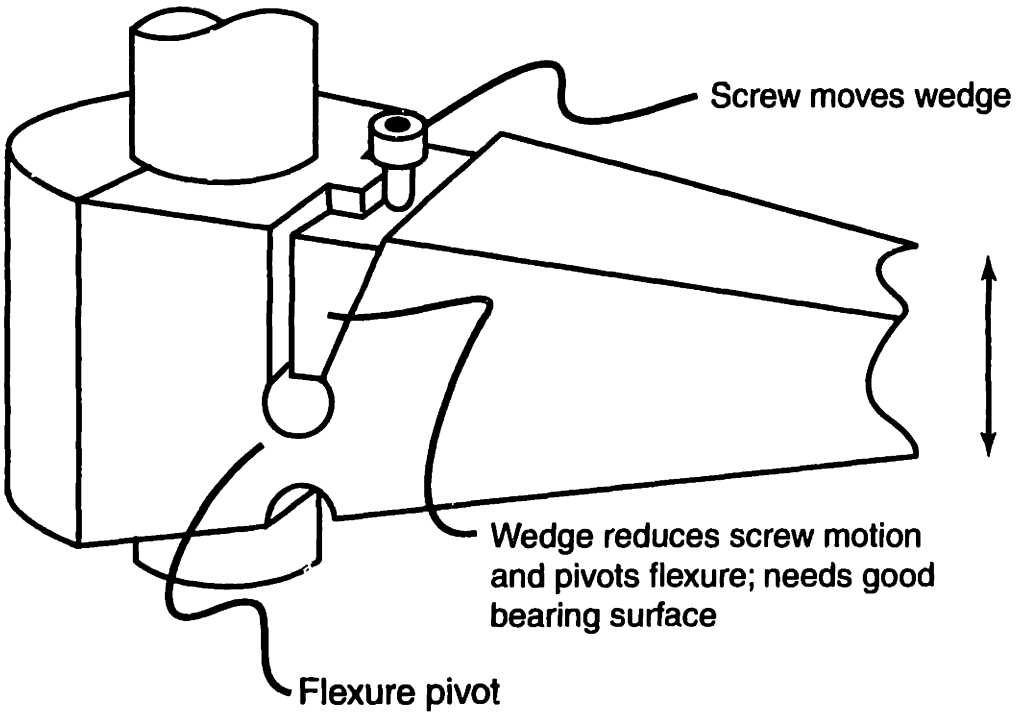

Figure 5-12: Concept 12 - Single rotary flexure with wedge drive.

to provide as large a contact area as possible, for high stiffness. This will likely be a line contact formed by a cylinder riding on the wedge. Such a design provides a "semi-kinematic" interface with the wedge and will likely allow much better adjustment. Difficulties in manufacture and design will include the bearing interfaces with the wedge, which will need to be smooth for friction-free, fine adjustment of the arm. Advantages include the lack of parasitic motion for small adjustments, if the notch bearing is manufactured precisely.

Concept 13

This "double-diaphragm" design was actually developed during the detailed design phase, and was not one of the initial design concepts. It grew out of a combination of Concepts 10 and 12, using the elastic deformation of a beam from the former with the rotational notch flexure of the later. By using two opposed diaphragms, pictured in Figure 5-13, shear force is removed from the notch support flexure. Adjusting the relative spacing of the diaphragms produces a very small movement at the tool

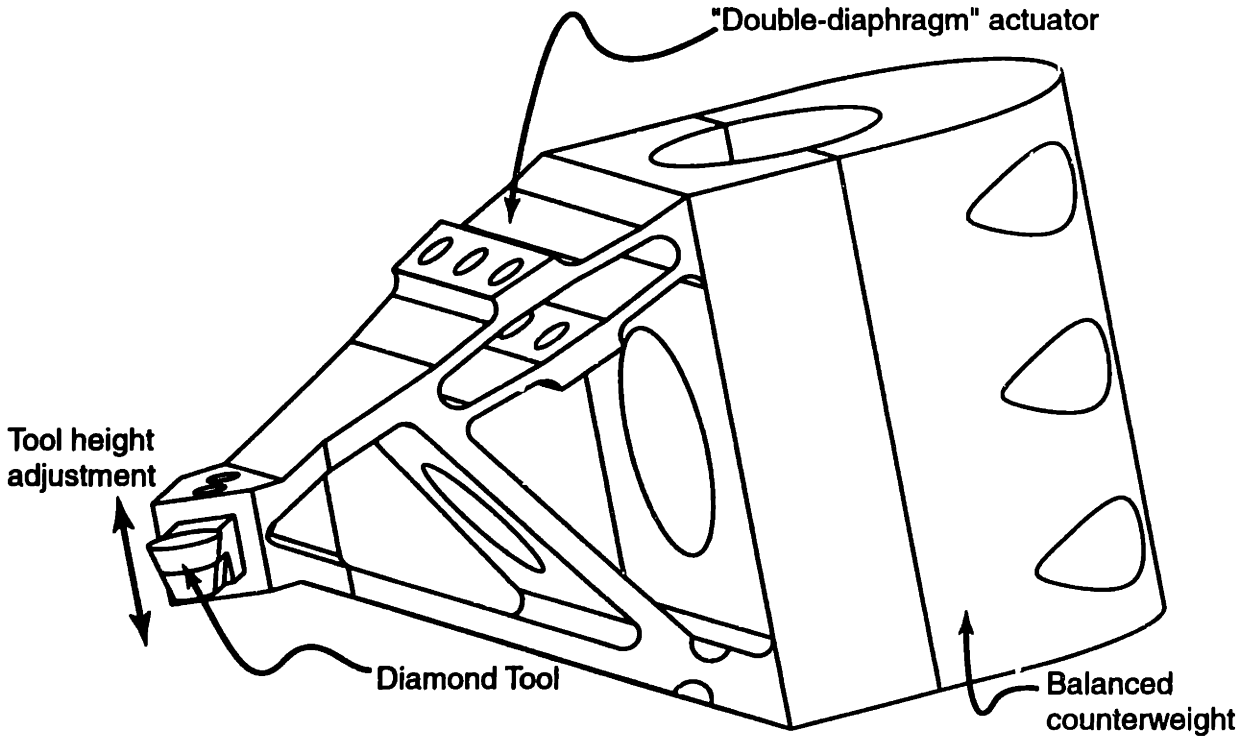

Figure 5-13: Concept 13 - "Double-diaphragm" actuator design.

tip, providing an excellent reduction ratio. This design also has the property that it can easily be manufactured with the Wire-EDM process, which is one reason it was selected for the final design.

Chapter 6

Design Elements

6.1 Overview

This chapter describes techniques for the design of many of the elements in the concepts of Chapter 5. While some evaluation of design concepts may be based on "gut feel" or experience, especially with regards to the manufacturability of a design, further knowledge of the physics behind the concepts is needed for proper detailed design. This chapter covers the design of several of the more promising actuator, bearing, and structural technologies used in the conceptual designs. With this knowledge of the relevant physics, informed decisions can be made on which concepts should be explored further.

6.2 Flexural Bearings

Flexural bearings are widely used in many industrial and commercial applications. The design and implementation of flexural bearings are quite different from that of conventional bearings, such as journal bearings, ball bearings, or linear guides. The latter all rely on some form of sliding or rolling contact, whether it is through direct mechanical support or a fluid film, to provide translational or rotational motion. As such, they are susceptible to friction, lack of accuracy, and other undesirable effects. Flexural bearings, in contrast, rely on the elastic strain of materials to provide

translational or rotational motion. Such bearings are then free of frictional effects, although they will of course also have a stiffness associated with the axis of motion.

Flexural bearings have a wide variety of applications. At one end of the spectrum, flexural bearings, or flexures, are used to provide the highest precision motion available. Commercial linear actuators are available with atomic level (Ångstrom) resolution, where the frictionless characteristics of flexures are indispensable. At the other end, "snap-fit" devices and simple hinges are made from flexures, easing assembly tasks and simplifying the manufacture of thousands of everyday devices, where injection molded plastic can take of the place of much more expensive fasteners.

There are numerous advantages to using flexural bearings over conventional designs. The accuracy of these bearings, like any bearing, is limited by the accuracy of the manufacturing process, but is in general quite good. Flexural bearings are somewhat less sensitive than other bearings to the manufacturing process, and off-axis error motions from the bearing can be minimized with proper design and manufacture. For many applications, the inaccuracies in the bearing are often not a problem, due to the outstanding repeatability of these bearings in the absence of varying loads. With low hysteresis materials and consistent loading, flexures can be made to repeat to subatomic levels, which has lead to their wide use in high resolution instruments, such as Atomic Force Microscopes[30]. Even the effect of varying loads, if the loads are known, can be accurately predicted. Since there is no sliding or rolling contact in flexural bearings, structural finite element analysis techniques can quite accurately predict the stiffness and deformation of the bearing, something that is much more difficult with other bearings. Depending on the exact geometry of the bearing, analytic techniques can also be very successful. The friction-free nature of the bearing also allows the resolution of the system to be limited only by the actuation mechanism, and frees the bearing from many environmental effects. Conventional bearings require seals to prevent grit or dust from entering the bearing, which is particularly problematic in a cutting machine, which produces a large amount of chips from material removal. The lack of interfaces in relative motion makes flexural bearings immune to these effects.

Disadvantages of flexural bearings include their very limited range of travel. This problem is heightened by the desire to limit the maximum stresses in the flexure material to 10-15% of the yield strength[29]. Limiting the maximum stresses to this level ensures that the flexure will remain dimensionally stable over long periods of time. Of course, larger stresses, up to the elastic limit of the material, could be used if long term stability is not necessary, and fatigue life not an issue. Another disadvantage is the negligible damping of the flexure, which is due to its lack of interfaces. For many structures, it is the interfaces between elements where most damped energy is dissipated. For example, in a conventional dovetail slide, large area oil-covered slideways can provide significant squeeze film damping.

Flexures can be designed in a variety of configurations, depending on the type of motion required. Rotational motion can be provided by "notch," beam, or "cross-strip" flexures, and translational motion by multiple beams or rotating axes. The design of these flexures is explored in the following sections.

6.2.1 Notch Flexures

The "notch-type" flexure, as shown in Figure 6-1 is perhaps the most common single axis flexure, used to provide rotational motion. This type of flexure has very desirable kinematic properties in that the axis of rotation is reasonably well defined, as nearly all the bending occurs at the center of "necked-down" region. Unfortunately, the angular rotation of the flexure is limited by this feature as well, since the elastic strain is confined to this small region.

The behavior of these flexures is well-modeled analytically using beam bending theory. The general differential equation of an elastic curve[38] for a beam subject to an applied moment M is

$$EI\frac{\partial^2 y}{\partial x^2} = M \tag{6.1}$$

where E is the modulus of elasticity of the material and I is the moment of inertia of the section of the beam with respect to the neutral axis. This assumes the material is isotropic, homogeneous, obeys Hooke's law, and has planar cross sections which

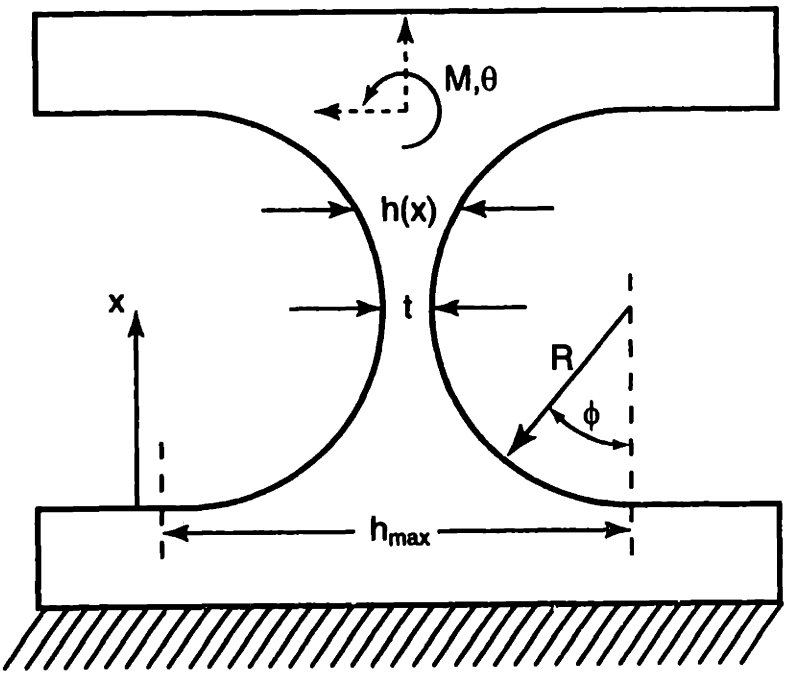

Figure 6-1: A notch hinge rotational flexure.

remain plane during bending. Modeling the hinge with one fixed end, the angular displacement of the free end $\theta = \frac{\partial y}{\partial x}$ is given by rearrangement and integration of Equation 6.1 as

$$\theta = \int_0^L \frac{M dx}{EI} \tag{6.2}$$

where $L = 2R$ is the length of the beam, neglecting any deformation past the notch, which will be relatively small. However, the rectangular cross section of the hinge, and hence I, is variable over the length of the beam. Thus it is more convenient to redefine the problem in polar coordinates (r, ϕ) as shown in Figure 6-1. The moment of inertia of a rectangular beam in Cartesian coordinates is given by

$$I = \frac{1}{12} b h^3 \tag{6.3}$$

where b is the width of the beam into the page. Performing a change of variables $x = R\cos\phi$ and $h = t + 2R - 2R\sin\phi$, Equations 6.2 and 6.3 become

$$I = \frac{1}{12} b (t + 2R - 2R\sin\phi)^3 \tag{6.4}$$

$$\theta = \int_0^{\pi} \frac{MR\sin\phi d\phi}{EI} \tag{6.5}$$

This integral can be evaluated by parts, with a table of integrals or symbolic math software, as per Slocum[29], to

$$\theta = \frac{3MR}{2Eb[Q^2 - R^2]} \left\{ \frac{1}{Q} + \frac{1}{Q^2 - R^2} \left[\frac{2R^2 + Q^2}{Q} + \frac{3RQ(\frac{\pi}{2} - \arctan(\frac{-R}{\sqrt{(0.5t-R)^2 - R^2}}))}{\sqrt{Q^2 - R^2}} \right] \right\} \tag{6.6}$$

where $Q = 0.5t + R$. This equation gives the angular displacement as a function of applied moment and geometry, but of more interest is the maximal angular displacement based on the elastic limit of the material, since actuation systems can be sized to apply the appropriate loads. The maximum stress will be found at the thinnest section in the center of the web, where $\sigma = \frac{Mt}{2I}$. Combining this with Equation 6.3 results in

$$\sigma_{\max} = \frac{6M}{bt^2} \tag{6.7}$$

Using Equations 6.6 and 6.7, designers can iterate to a successful flexure using a computer spreadsheet. Alternately, numerical solutions for a particular variable, given the others, may be programmed using iterative techniques. In either case, it is important to recognize some key points which may be obscured by the complex nature of Equation 6.6. First, more deflection can be achieved from the flexure by *decreasing* the center thickness t. Confronted with parameters which produce the desired deflection, but exceed the yield stress of the material, the designer may be tempted to *increase* t to lower the stress, based on Equation 6.7. However, this will be counterproductive, as the resulting increase in the necessary applied moment to achieve the same deflection will result in even higher stresses. Note that for any specified deflection, increasing t increases the strain, and hence the stress, in the outermost layer of material. Thus the proper procedure is to *decrease* the thickness of the material. Another point to recognize is that almost all the bending occurs at the center of the hinge; thus, these expressions are still quite useful even if the maximum height $h_{max} < t + 2R$. Equation 6.5 could be integrated for $\phi = \phi_1 \ldots \phi_2$

instead of $\phi = 0 \ldots \pi$ if the center of R does not lie on the edge of the hinge, but this would involve more computational effort.

The cumbersome nature of Equation 6.6 can be alleviated if some simplifying assumptions are made. Paros and Wiesbord[24] have shown that if $\frac{t}{2R} \ll 1$, and $t \ll h_{max}$, Equation 6.6 reduces to

$$\theta \approx \frac{9\pi M R^{\frac{1}{2}}}{2Ebt^{\frac{1}{2}}} \tag{6.8}$$

Such a simplification can be performed by introducing nondimensionalized variables $\beta = \frac{t}{2R}$ and $\gamma = \frac{h_{max}}{2R}$ into Equation 6.6 and noting $\beta \ll 1$ and $\beta \ll \gamma$. Paros and Wiesbord[24] also illustrate that even the more general case, where $h_{max} < t + 2R$, the solution will still reduce to Equation 6.8. Again, this is due to the concentration of bending in the center.

By combining Equations 6.7 and 6.8, the maximum angular displacement can easily be found as a function of the elastic limit of the material.

$$\theta \approx \frac{3\pi R^{\frac{1}{2}} \sigma_{max}}{4Et^{\frac{1}{2}}} \tag{6.9}$$

Of course, σ_{max} can be adjusted from the yield strength of the material to account for a factor of safety. As noted earlier, 10-15% of the yield strength is often used for long term stability.

Other researchers have attempted different approximations of Equation 6.6. Smith and Chetwynd[30] present results derived empirically from finite element analyses. However, there is an error in Equation 4.20 of their text, where the denominator has the form $8R + E$. These units are not only inconsistent, but even if they were desired, they do not make sense in any consistent unit system, such as (m,N,Pa,s), where the E term would make $8R$ inconsequential. This error was present in the third, 1997 printing of the text, and prevented it from being used in this design. Subsequent checking has shown that the fourth, 1998 printing has corrected this term to $8R + t$. Even so, Equations 6.6 and 6.8 are still more useful, as the Smith and Chetwynd

empirical results are only valid for $t < R < 5t$.

6.2.2 Beam Flexures

When large angular displacements are required, the designer may quickly become frustrated with the notch flexures in Section 6.2.1. Very large radius notch flexures are required for significant angular displacements, due to the confinement of strain to the center of the flexure. These flexures are frequently larger than the available space for the bearing. One basic method for increasing the maximum angular displacement for a given space is to increase the amount of material subject to significant strain, by elongating the thin central section into a beam. It is best to preserve some radius from the notch flexure at the interface of the beam with the base and supported components, in order to reduce stress concentrations at the interface, as shown in Figure 6-2. In this manner, the total deflection of the flexure may be calculated by the addition of the notch deflection with the beam deflection. Unfortunately, by introducing this large area for strain, the kinematic properties of the notch hinge are not preserved, and significant parasitic deflections will be experienced in other directions. In addition, the long thin beam will significantly reduce the resistance of the flexural bearing to shear forces perpendicular to the beam. These tradeoffs may be considered acceptable if space is a major constraint.

The angular deflection of the beam section can be easily calculated from Equation 6.2. Since the beam is of constant cross-section, I is constant, and

$$\theta = \frac{ML}{EI} \tag{6.10}$$

It is very important to note the loading assumptions made here and in Section 6.2.1; that the beam is subjected to a *moment* load. This results in the *maximum* angular deflection, since each planar section in the beam is distorted by an equal moment. Care must be taken in the design of the actuation system to best approximate such loading. Since most actuators will likely output forces, they must be aligned such that the applied force is along the longitudinal axis of the beam, and generates a moment

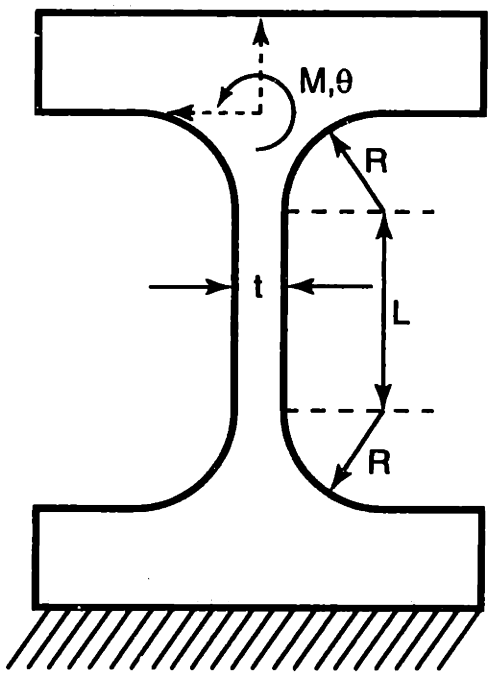

Figure 6-2: A beam hinge flexure.

by being offset from the neutral axis. If the applied force is instead transverse, the beam will not be subjected to a constant moment, instead reaching a peak at the base of the beam. This will generate much less deflection before σ_{max} is exceeded, since much of the beam will not see the full loading. Indeed, if the beam is subjected to a transverse force F, this will generate only *half* as much deflection as a moment $M = FL$. The notch hinges are somewhat less sensitive to this effect, given that the strain is confined to such a small area.

Beam flexures need not be straight. Even more angular deflection can be achieved in a given linear dimension by curving the beam, increasing the available length for deflection, as shown in Figure 6-3. Such beams need not be limited to the quarter-circle shown, but could have several curved sections. Since it is unlikely that an applied moment could be well approximated for such a beam, it is best to design with applied forces. Such highly configuration-dependent formulas will not be presented here, but are well documented in references such as *Roark's Formulas for Stress and Strain*[38]. These flexures will suffer from a lack of stiffness to disturbance forces, as thin sections will be presented in virtually every direction. This makes them difficult to use in the presence of variable loading, unless the actuation forces are much larger

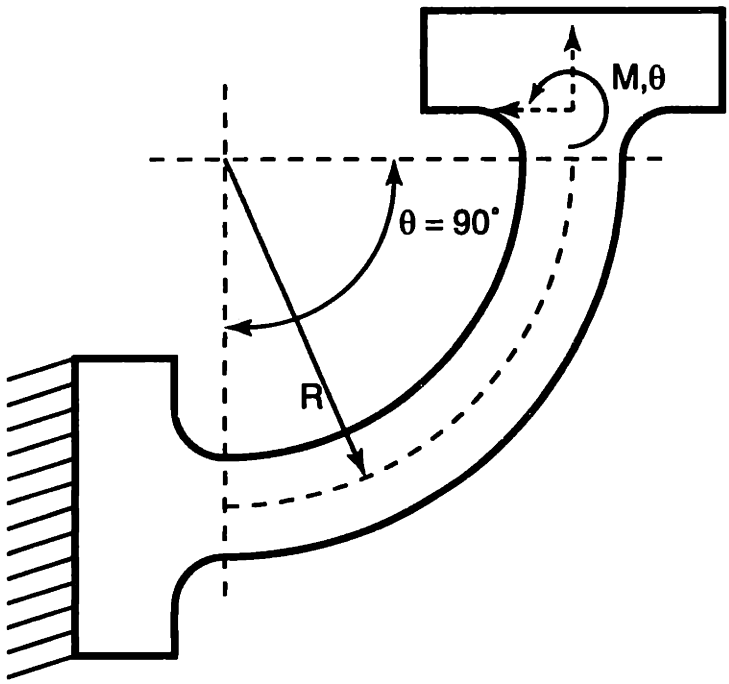

Figure 6-3: A curved beam flexure.

than the variable disturbance forces.

6.2.3 Cross-Strip Flexures

The beam flexures in Section 6.2.2 suffer from a lack of stiffness, particularly in off-axis motion as they are made thinner and longer to accommodate more deflection. Such flexures also become less and less "kinematic" as the beam length is increased, since there is no defined axis of rotation. Cross-strip flexures, as shown in Figure 6-4, eliminate many of these problems while retaining much of the large deformation capability of beams. These flexures have a well defined axis of rotation, and are much less susceptible to deflection due to disturbance forces. The axis of rotation is found at the intersection of the two strips; note that such strips due not need to physically cross and the rotation will occur about their projected intersection, as in Figure 6-4. However, cross-strip flexures still suffer from parasitic off-axis motions. While the axis of rotation is well defined, it will also translate as the flexure is pivoted. Cross-flexures are often assembled from clamped sheet material, but can also be monolithic in nature. One complication for assembled flexures is that care must be taken to ensure that no

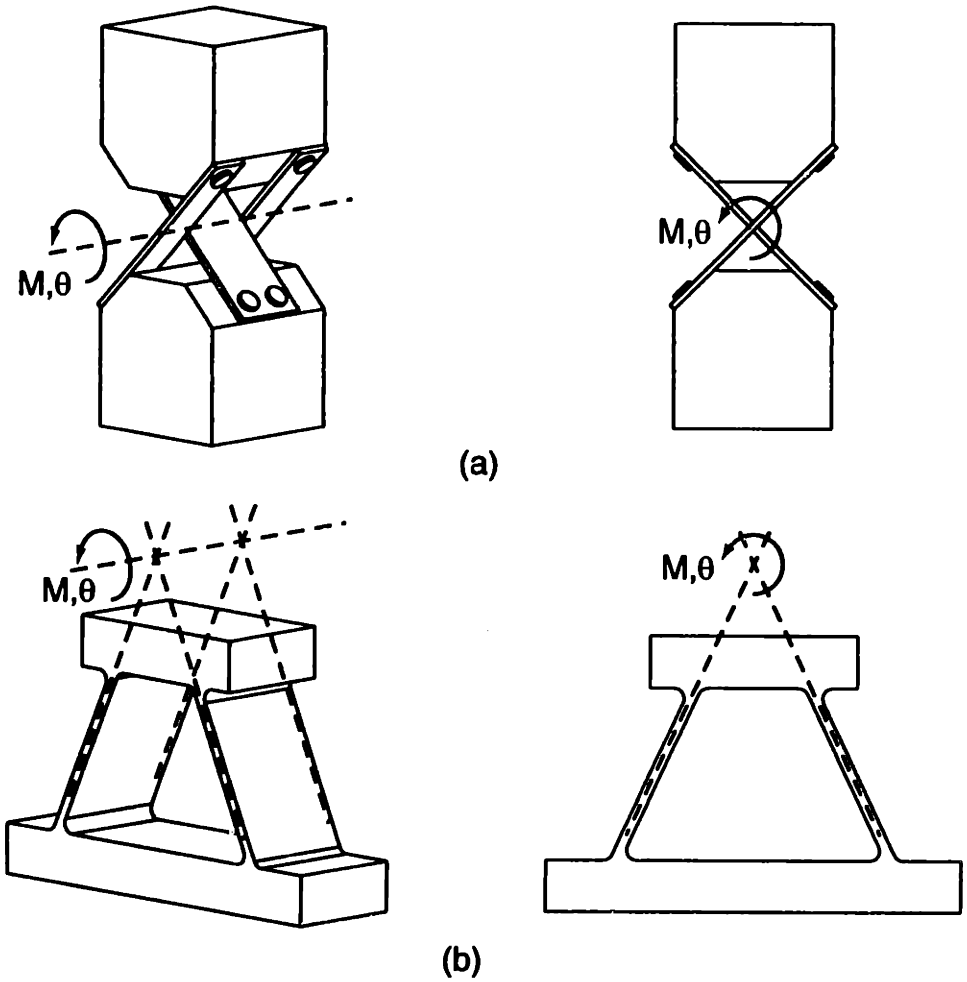

Figure 6-4: Cross strip flexures. (a) clamped design (b) monolithic design

stresses are induced in the material during assembly. Commercial cross-strip flexures are available from vendors such as Lucas Aerospace [16] in a variety of standard sizes to suit the needs of the designer. These have a circular housing to enable them to be easily mounted like conventional rotary bearings.

For the ultimate kinematic performance, a 3-strip flexure can be used. Such a flexure is illustrated in Figure 6-5. The intersection of the three strips should be set to form a unique axis of rotation. Unlike the traditional, 2-strip flexure, the axis of rotation for a three strip flexure will have little parasitic translation for larger angular rotations. These flexures, like the 2-strip flexures, can be monolithic or assembled, but the assembled versions may require a tension adjustment in the strips to allow proper function.

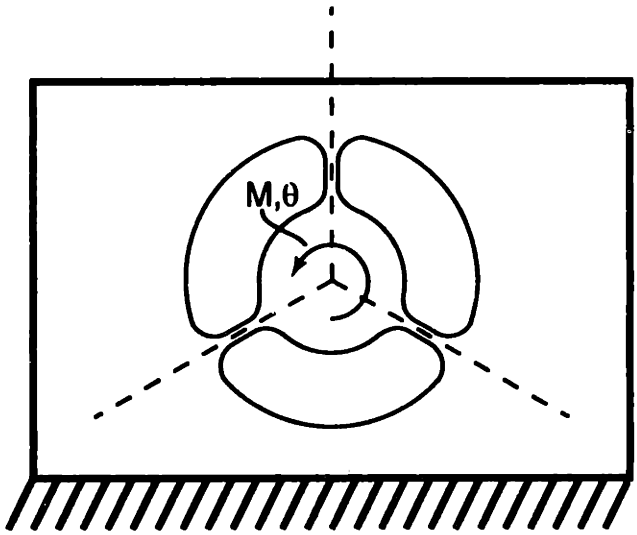

Figure 6-5: 3-strip monolithic flexure

The design of these cross strip flexures is more involved than the simpler notch or beam flexures; greater constraint produces more complex shapes. Weinstein documents the design of these structures in a two part series in *Machine Design*[35],[36].

6.2.4 Translational Flexures

The preceeding sections focused on the design of rotational bearings. If translation is desired, the previous designs can be adapted to provide translational motion. Two equal-length beam flexures can be mounted so that the beams are parallel, as shown in Figure 6-6 (a). This is equivalent to designing a cross strip flexure where the intersection of the axes is at infinity. If large loads are to be supported, the design must be checked to insure that the beams are not susceptible to buckling. These flexures are do exhibit some error motions, primarily in pitch angle and in vertical motion. Such errors can be magnified by the manufacturing inaccuracies in the flexure, primarily the variation in beam length and spacing, as well as by the actuating force. The actuating force must be halfway between the platform and the base in order to prevent a moment from being induced on the structure. Also note that the beams must now be modeled with fixed-guided end conditions, not the fixed-free conditions used earlier, to derive the lateral displacements. These are *not* cantilevered beams.

If columnar buckling is a problem, the translational flexure can be constructed

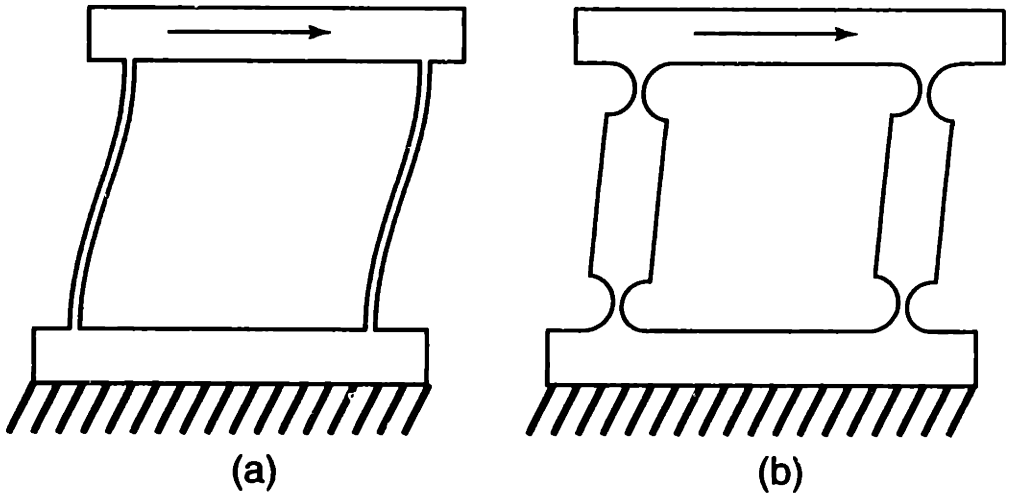

Figure 6-6: Translational Flexures. Note that actuation forces need to be properly applied to avoid parasitic motion

from notch hinges, as in Figure 6-6 (b). The reinforced beam length will be much less susceptible to buckling. However, as in the rotational flexure design, there will be the tradeoff of reduced travel in the flexure.

6.3 Actuators

Actuation systems need to be considered simultaneously with the bearing design for any system, as they are usually closely interrelated. For example, translational flexure stages, as shown in Section 6.2.4, require the actuator to force halfway between the beams, and this may restrict the space and geometry available. For this design, the actuators need to be capable of providing μm or sub-μm motion, which is a much higher resolution than most motion systems. Often, when designers consider high precision motion, they think of motor-based systems with a high resolution feedback system. Such systems are impractical for this tool height adjustment mechanism, however, because of the limitations of size and inertia, the latter being particularly difficult.

For this design, compact, low mass actuators are needed. This does not prevent feedback from being utilized, however. The tool height adjustment should ideally

be a "set and forget" type adjustment which is performed only after a tool change. This allows a feedback device to be used during the adjustment, then removed for operation of the toolarm. While conventional electrical servo loops could be closed in this arrangement, the most practical control loop involves a human operator adjusting the tool height while it is measured with some type of gauge. Many high precision lathes today have a "tool height set station" which is a nulling device; the operator moves the tool to the "set station", then adjusts the tool to the known zero (which has been determined experimentally). Used in this manner, the gauge needs resolution and repeatability, but not accuracy over its travel.

6.3.1 Screws

Screws are one of the most basic instruments for inducing mechanical motion and can be viewed as an effective way of packaging an inclined plane in a compact space. Typically, designers consider ballscrews and leadscrews when designing high-precision mechanisms. These devices have considerable attention paid to the accuracy of the lead and removal of backlash, but they are much too bulky for the toolarm system. Conventional fasteners, in contrast, are often overlooked as sources of motion. They suffer from a lack of lead or thread accuracy, and have high friction. For a "set and forget" measurement, however, this high friction can be very desirable; since it prevents "backdriving" of the screw, the motive power can be a human operator, who need not be present after the position is set. Lead accuracy problems are also avoided if an external gauge is used; thus, the bulky graduated barrels of a micrometer are not necessary. A typical person, with some kind of feedback gauge, can adjust a common $\frac{1}{4}$-20 screw to the desired position within 5-10 μm. Note that the pitch of this screw is 20 threads per inch, corresponding to an movement of 0.050 in. or 1.27 mm per turn.

Finer pitch screws are available as standard fasteners, but they have smaller body diameters which may compromise their usefulness. A #10-32 fastener, with 32 threads per inch, represents a useful increase in pitch over the $\frac{1}{4}$-20 screw, but maintains only about 55% of the cross-sectional area. It is important to size the diameter of the

actuator appropriately. If the screw is used to push, the bending stresses due to misalignment can be very significant, and buckling of the screw could result at high load levels. This is somewhat less of a problem for screws operating in tension, due to the lack of buckling, but misalignment can still result in plastic deformation of the screw. Since the moment of inertia is a function of the d^4, most small diameter fine screws, such as a #4-40, are very limited in their load capacity.

Large diameter fine pitch screws are available, but are more difficult to find. They are usually found marketed as adjustment devices in optics mounts, a low-force instrument application. The most common size is the $\frac{1}{4}$-80 screw, which is available from manufacturers such as Newport [23], New Focus [22], and Thorlabs [33]. The fine 0.0125 in. lead permits sub-micron resolution over relatively large travel ranges. These screws are only available as "push" actuators, with ball or flat ends. Ball tips help prevent any coupling to the driven device other than the desired translation. The fine thread does impose some manufacturing difficulties, and these screws are usually supplied with a matched bushing for mounting the screw. These bushings considerable increase the mounting space required for the screw, however, which could make their use difficult on the toolarm. Alone among these manufacturers, Thorlabs supplies $\frac{1}{4}$-80 taps for cutting threads in other components.

Unfortunately, one possible complication with the use of fine-pitch, high resolution screws is limited load capacity. These screws are typically used in low-load instrument applications. Newport, in their catalog, quotes a load capacity of 20 lbf, and notes that the small screw threads will "bind" at those loads and "motion will become difficult". This is in sharp contrast to a conventional $\frac{1}{4}$-20 screw, which is likely to provide more than 1500 lbf clamping force, based on yield stress, although this will vary depending on the material composition. Newport does claim that such loads are unlikely to damage the screw, just make motion difficult. However, in an independent test, engineers at the University of Hawaii[9] noted "degradation" of a Newport screw when axially loaded with 30 lbf and moved over its range of travel. The extent of such degradation is not noted.

To test the load capacity and feasibility of these fine pitch screws, several Thorlabs

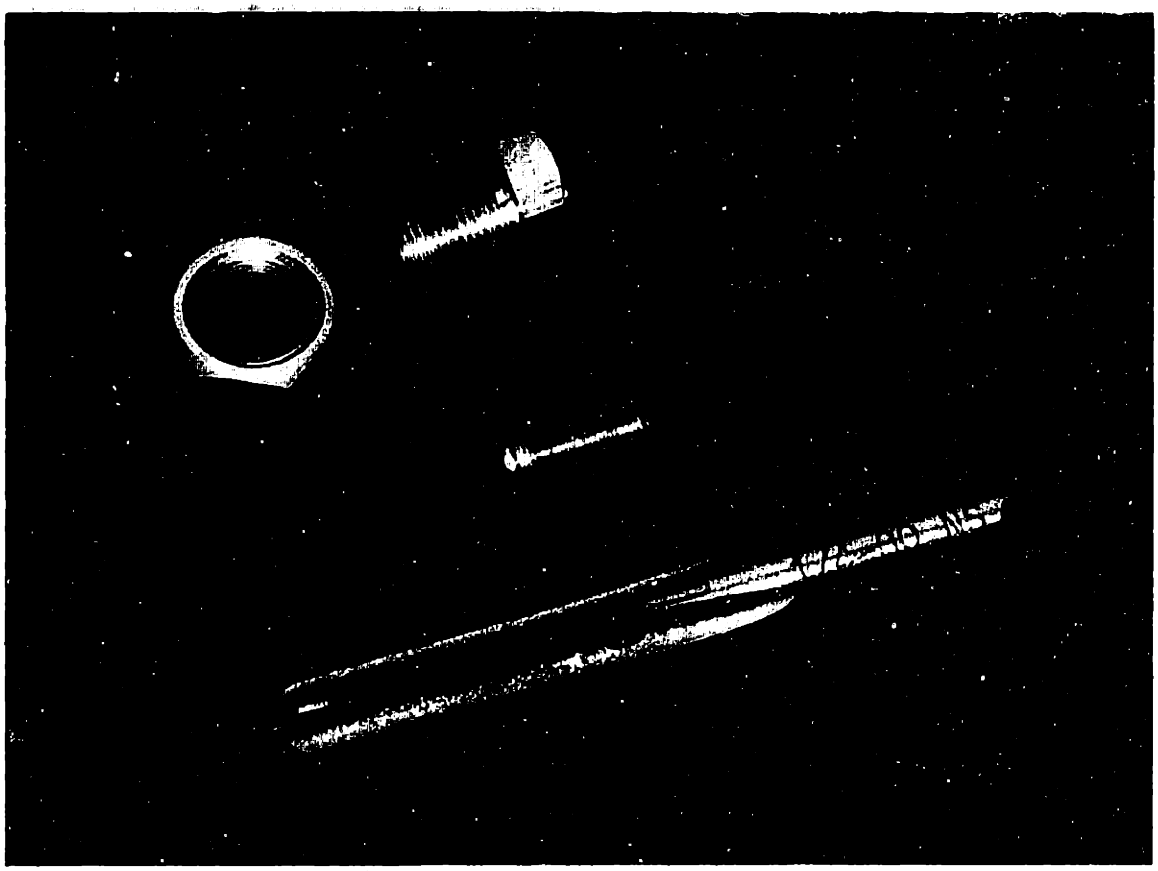

Figure 6-7: Thorlabs $\frac{1}{4}$-80 bushing, screw, and tap

$\frac{1}{4}$-80 screws were purchased, as shown in Figure 6-7, and tested to determine their force output. The tests were conducted using the supplied brass bushings, pushing against Kistler [13] Model 9212 load cells connected to Type 5010 charge amplifiers. These amplifiers would produce an analog output, scaled to a desired range, which could be read on an oscilloscope or voltmeter. As can be seen in Figure 6-8, the actual force output was much greater than the 20 lbf value which Newport quoted. However, this was achieved using hex head screws with an Allen wrench; this provided about a 2 in lever arm. Over 200 lbf could be achieved with this setup. The force output with a knurled knob end, with which some screws are sold, would undoubtably be lower.

The high force output of the screw may not be easily usable for adjustment, however. When the high force levels where reached, friction in the threads caused a significant "stick-slip" problem, particularly when trying to move gradually in the reverse direction, where the load force tries to move the screw in the same direction as

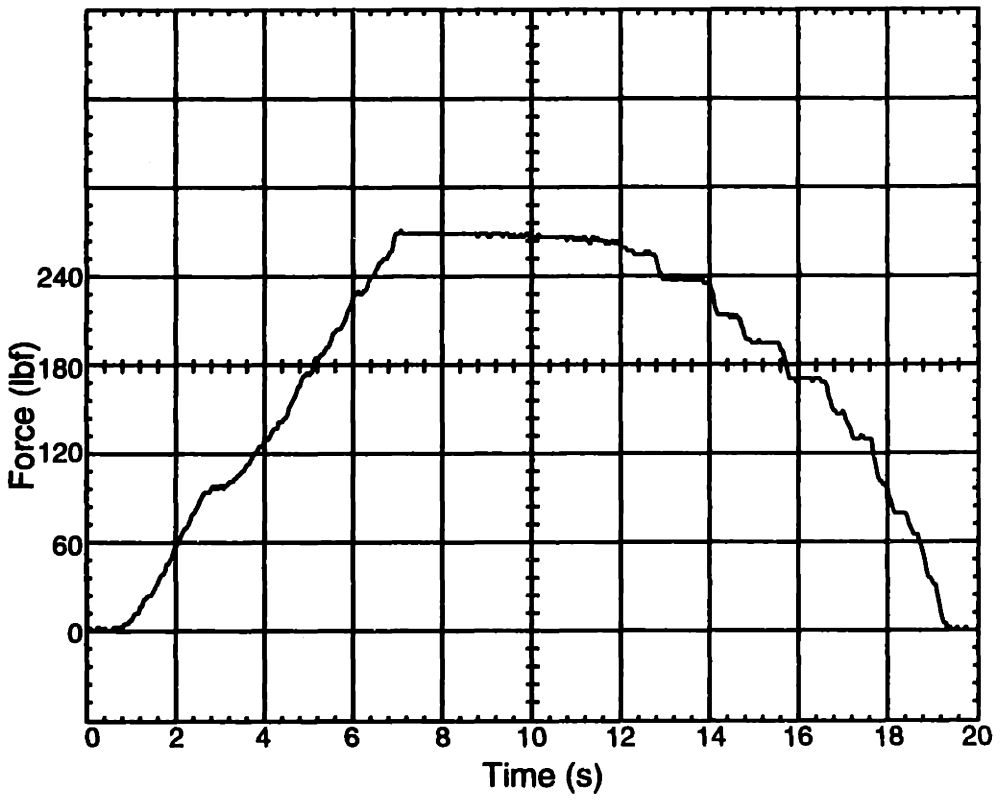

Figure 6-8: Force output from $\frac{1}{4}$-80 screws. Note the "stairstepping" as the force is decreased, due to stick-slip.

the adjustment. This can be seen in the downward path in Figure 6-8. While it may be possible to achieve the desired position with this setup, adjustment could be an exercise in patience at high force levels, given the "stick-slip" phenomena. Adding to this problem was the significant deflection of the wrench handle, which stored energy to be released when the "slip" occured.

It is also worth noting that test threads were cut with purchased taps. It is recommenced that the screws be used with the bushings, but these add bulk and may make implementation of a drive system difficult. Tap cut threads seemed to function acceptably when cut in both steel and aluminum. Tribological considerations dictate that the screws should not be used when threaded directly into aluminum, as galling could result since the screws are steel. Of interest, however, is to see that the tap drill must have overcut into the softer aluminum; the thread depth on the $\frac{1}{4}$-80 screws is so small that the threads were not continuous around the circumference in aluminum!

Another means of obtaining very high effective resolution screws, while retaining large force capability, is to use differential screws. These screws are attractive because they can be manufactured from the commonly available coarse and fine threads used in standard fasteners. The key concept is to rely on the difference between two threads. Referring to Figure 6-9, note the two parts, A and B, fastened by a screw with the different pitches P_1 and P_2 in each part. If the screw is rotated one turn, it will thread into part A by the distance $\frac{1}{P_1}$, and into part B by $\frac{1}{P_2}$. The separation between the pieces then changes by the difference between these two advances:

$$\frac{1}{P_{eq}} = \frac{1}{P_1} - \frac{1}{P_2} \tag{6.11}$$

This simplifies to:

$$P_{eq} = \frac{P_1 P_2}{P_1 - P_2} \tag{6.12}$$

This relationship allows standard $\frac{1}{4}$-28 and #10-32 UNF screws to be combined to form an equivalent 224 tpi screw, which provides 7 times the resolution of a #10-32 screw by itself and almost 3 times the resolution of a fine pitch $\frac{1}{4}$-80 screw!

Although differential screws are an excellent way to increase the resolution of a

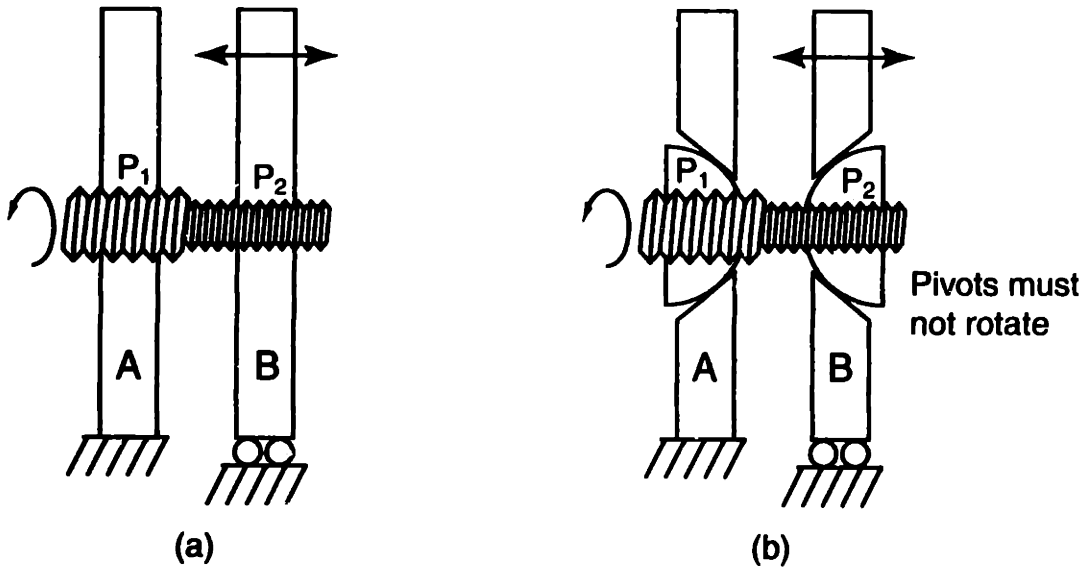

Figure 6-9: Implementation of differential screws. Pivots in (b) prevent binding, but rotation must be constrained.

screw system, there are several pitfalls which need to be avoided. First, the screw is threaded into *both* parts. Any *small* angular misalignment in the two parts will cause binding in the threads, due to the large bending stresses, making motion impossible. This provides a quite different challenge from conventional fasteners, where there is a clearance hole in one piece. Care must also be taken to ensure that there is no angular misalignment, or else the screw needs to ride in a pivot joint of some sort, such as that shown in Figure 6-9 (b). Note that these pivots must be restrained from rotation, so that the screw threads into the pieces. The total travel of the system is also affected by the same factor as the decrease in resolution. Thus, given the factor of 7 in the example earlier, the travel is also decreased by a factor of 7. This effect also makes assembly of the screw into the pieces difficult, especially with very fine pitches, as the travel is not sufficient to move the parts into the desired location after assembly. It is often necessary to mount the screw in some kind of threaded bushing, whose position can be adjusted in the part. This could be incorporated into the pivot joints mentioned earlier.

Another problem with the differential screw is that the play in the two screws adds together, forming a screw system with a large amount of backlash. It is best to preload the system with a spring or other device, in order to bring the backlash down

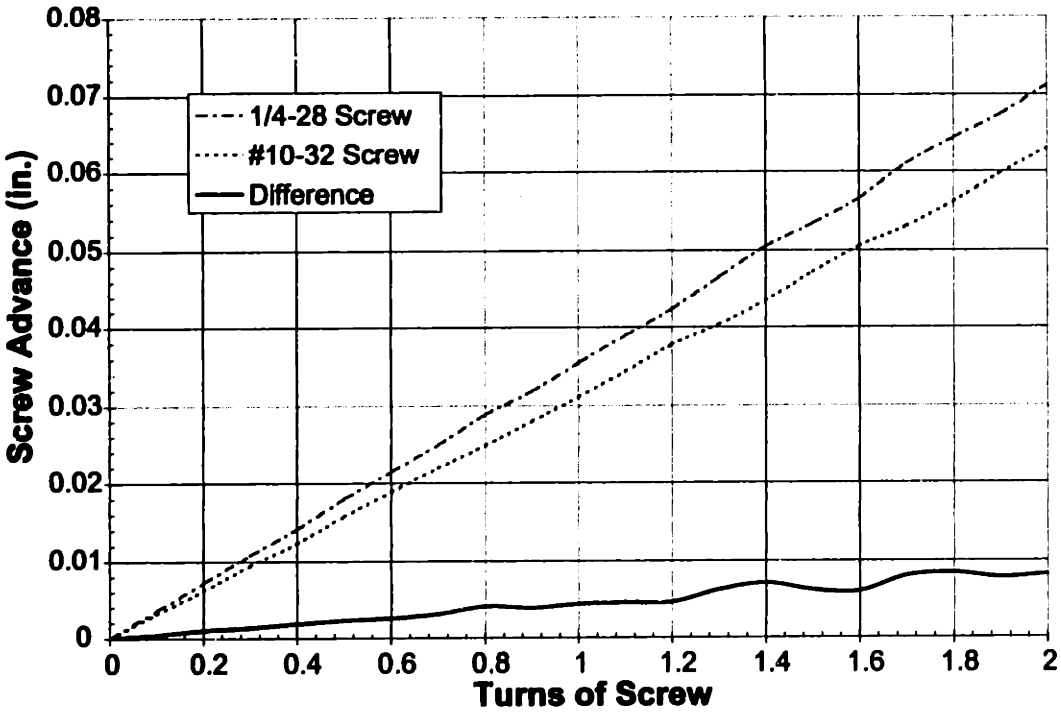

Figure 6-10: Errors in differential screw movement, random ±1.25% pitch error per screw. Note direction reversals.

to an acceptable level. But perhaps the biggest problem with the differential screw is the lead error. Each screw, particularly those formed from standard fasteners, has some amount of lead error. But since the design relies on the difference between two threads, if the threads are too close in pitch, the error could cause the difference to become extremely small or even reverse! Figure 6-10 illustrates this effect with the example screw presented earlier, adding a random error of ±1.25% to each screw. As shown in the Figure, there are not only "dead" spots in the screw, but also reversals of direction! This effect can be avoided by not being too ambitious in the resolution of the screw and using threads with a greater pitch difference.

6.3.2 Transmission Mechanisms

Transmissions are an important part of any actuator mechanism. Conventionally, transmissions consist of systems of gears, pulleys, belts, and chains which scale the output of an actuator to achieve some desired end. In an automobile, for instance, the transmission increases the torque of the engine, at the expense of increasing the num-

ber of engine revolutions per mile. Likewise, in precision mechanisms, transmissions can be used to scale forces, although the most common use is to change the resolution of an actuator. This resolution must come at a price; decreases in resolution must come with a corresponding decrease in the amount of travel. For purely rotational systems, this is trivial to overcome, as the number of rotations can be increased. Linear systems, however, can be more problematic.

Gears and chain drives, the mainstays of conventional gross-motion power transmissions, have more limited application for high precision mechanisms. Nonlinearities in the output due to backlash, for example, can make implementation difficult. Any type of sliding interface can lead to limited repeatability. These problems can be limited at some level by using "Anti-backlash" gears, where two gears ride on the same axis and are preloaded against another gear. But perhaps the most common transmission for precision mechanisms is the most simple: the lever and fulcrum, as shown in Figure 6-11. A simple summation of moments and forces yields the well known relationship

$$\Delta = \frac{\delta l_2}{l_1} \tag{6.13}$$

This basic device can be used with a flexural rotational bearing to provide excellent repeatability and a powerful reduction in output, as noted by Slocum[29]. Alternately, the small displacement output of a piezoelectric actuator could be scaled up to a more useful level. Typically, a lever mechanism could be made to provide a reduction in far less space than a gear transmission, but at the cost of very limited travel.

Another excellent reduction mechanism is the bowed flexure, as illustrated in Figure 6-11. By idealizing this as a triangularly shaped beam, an expression for the transmission ratio can be developed. Subdividing the beam into two right triangles, the hypotenuse should remain of essentially constant length for small deflections. Application of the Pythagorean theorem, $c^2 = a^2 + b^2$, then yields

$$\left(\frac{l_w}{2}\right)^2 + l_h^2 = \left(\frac{l_w}{2} + \Delta\right)^2 + (l_h - \delta)^2 \tag{6.14}$$

Assuming small deflections and neglecting higher order terms, this reduces the trans-

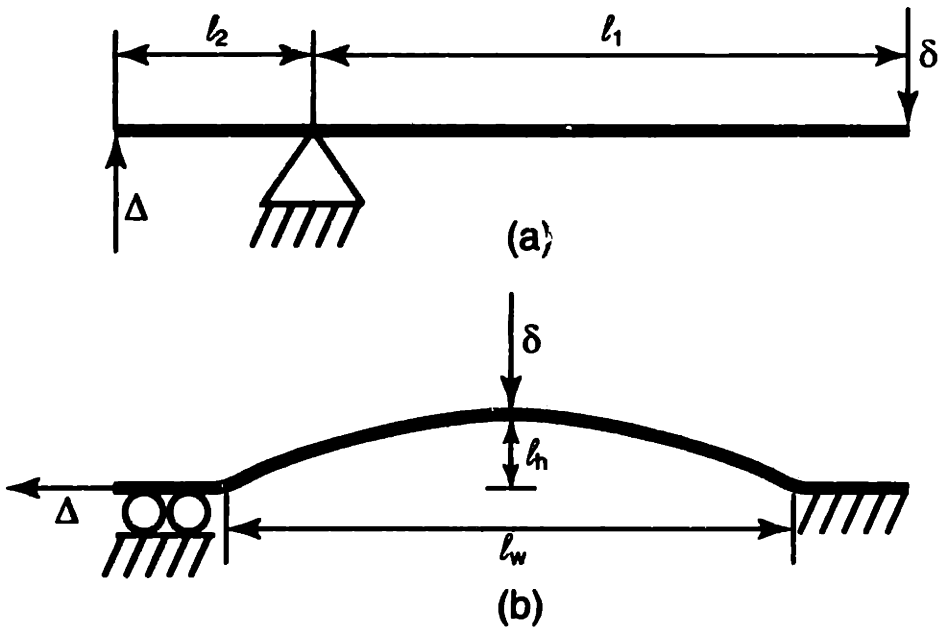

Figure 6-11: Mechanical transmissions. (a) lever (b) bowed flexure

mission ratio to:

$$\frac{\Delta}{\delta} = \frac{4l_h}{l_w} \tag{6.15}$$

For a truly curved beam, however, Slocum[29] notes that the actual deflection may be one-half this value, varying with the operating point of the actuator.

6.4 Structural Elements

Once a bearing and actuation system has been specified, the supporting structure of the tool can be further developed. This is the "arm" portion of the toolarm, and should extend the reach of the tool while fitting within the geometric constraints developed in Section 4.3.3. In addition, since this structure will likely form the bulk of the toolarm, it should be designed to limit its contribution to the rotary inertia of the system, while maintaining a very high stiffness against disturbance and acceleration forces.

One geometric configuration which stands out as an ideal candidate for the structure is the tapered hollow tube, as shown in Figure 6-12. Tubular structures are well known for their high stiffness and low mass, leading to their wide use in lightweight

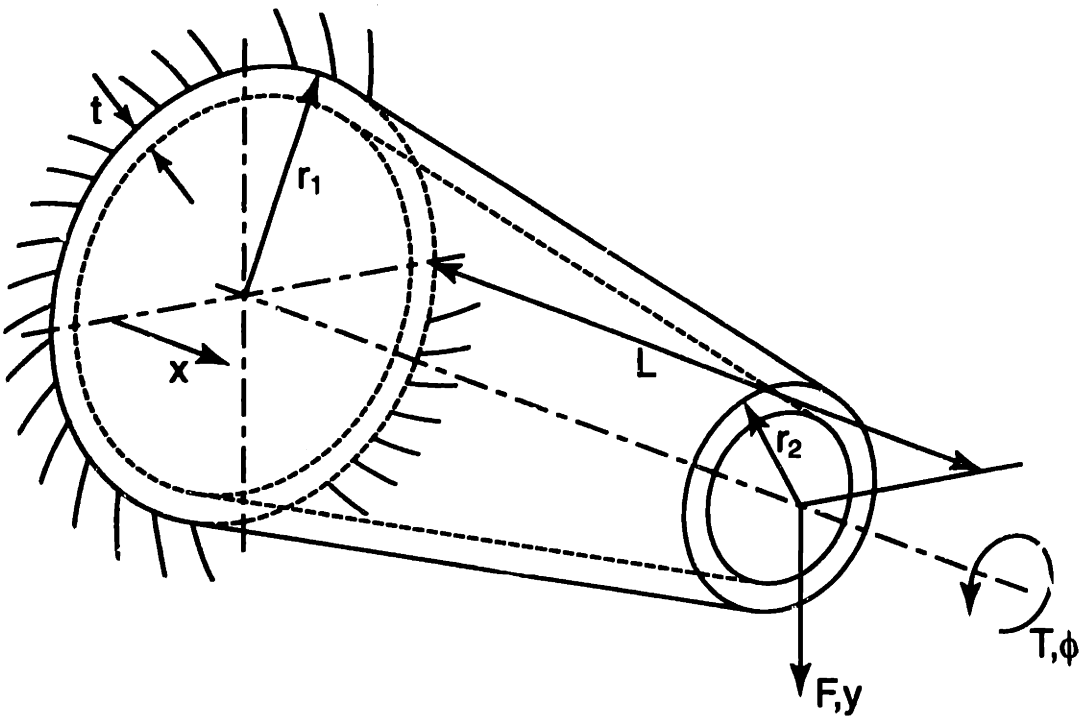

Figure 6-12: Tapered tube structural element

truss and beam structures such as bicycle frames. Hollow tubes place their mass at as large a distance from the neutral axis of the beam as possible, maximizing their cross-sectional moment of area. At the same time, the hollow nature removes most of the "dead-weight" which contributes little to the cross-sectional moment of area, since this is a function of the radius r^4. Large moment of areas contribute directly to increased bending stiffness. The tapered configuration of the tube will help maximize stiffness while fitting within the geometric constraints. The tool can be mounted on a "dogleg" off of the narrow end of the beam, allowing the tool to hook around obstacles.

Torsional stiffness will also be important in the toolarm structure, as not all cutting forces will be coincident with the centroid of the arm. In particular, the tangential cutting forces from Section 4.5.1 will likely exert a large moment on the structure, due to the cutting point being offset to minimize geometric interference. Fortunately, tubular structures present an ideal case to optimize torsional stiffness. Circular cross sections are the only ones which can be easily analyzed analytically, as plane cross sections perpendicular to the axis of the beam *remain plane* when a torsional load

is applied. For noncircular prismatic beams, out of plane deformations or warping results under torsional load. This can result in significant normal strains, and the beam cannot be treated as operating in pure shear, as with a circular cross section. This makes an analytic treatment nearly impossible, although if the structure has a closed, thin-walled cross section, shear force equilibrium can deliver approximate solutions.

In order to properly design a structure with a minimum of iteration and testing, the relationship between the stiffness of the beam and the geometric configuration and material properties needs to be well understood. These equations are developed in the following sections.

6.4.1 Tapered Tubes - Exact Analytic Bending Stiffness

The bending deflection of any beam can be found with proper integration of Equation 6.1. The integration is difficult for the tapered tube, however, because the cross section, like that of the notch flexure, is of a variable cross section. Unlike the notch flexure, there is no convenient change of coordinates to simplify the integration. The moment of area of any given cross section is

$$I = \frac{\pi}{4}\left(r_{outer}^4 - r_{inner}^4\right) \tag{6.16}$$

To express I as a function of the linear position x, note that r_{outer} varies linearly over the length L between the radius r_1 at the base and the radius r_2 at the end. The inner radius $r_{inner} = r_{outer} - t$, where t is the thickness of the tube. This results in the expression

$$I(x) = \frac{\pi}{4}\left(\left(\frac{(r_2 - r_1)x}{L} + r_1\right)^4 - \left(\frac{(r_2 - r_1)x}{L} + r_1 - t\right)^4\right) \tag{6.17}$$

The primary loading of the structure will come from cutting forces at the end.

Thus the moment in a given cross section is

$$M = F(L - x) \tag{6.18}$$

Substituting Equations 6.17 and 6.18 into Equation 6.1, it is obvious integration will be very difficult, since the integrating variable x cannot be factored out of the expression. This proved completely intractable to integration by hand, and the powerful symbolic mathematics software MAPLE V [34] was therefore applied to the solution.

After the first integration, the slope of the tube θ may be expressed as a function of x

$$\begin{aligned}\theta = \frac{dy}{dx} &= \frac{FL^2}{Et^3\pi C_4}\Big\{C_7\big[2\ln C_5 - C_6 + \ln(C_2C_3L^2) - 2\ln(C_1L)\big] \\ &\quad - 2t\arctan\left(\frac{C_5}{tL}\right) + 2\arctan\left(\frac{C_1}{t}\right)\Big\}\end{aligned} \tag{6.19}$$

where the values C_x are given by

$$C_1 = 2r_1 - t \tag{6.20}$$

$$C_2 = 2{r_1}^2 - 2r_1 t + t^2 \tag{6.21}$$

$$C_3 = r_2 - r_1 \tag{6.22}$$

$$C_4 = r_2^2 - 2r_2r_1 + r_1^2 \tag{6.23}$$

$$C_5 = 2C_3x + C_1L \tag{6.24}$$

$$C_6 = \ln\left[C_3(2C_4x^2 - C_5Lt + 4C_3Lr_1x + 2L^2r_1^2)\right] \tag{6.25}$$

Equation 6.19 can then be integrated again, substituting L in the limit of integration to find the total deflection at the end as

$$\begin{aligned}y &= \frac{-FL^3}{2t^3E\pi C_3C_4}\Big\{4C_7C_3\ln C_1 - 2C_7C_3\ln C_2 + 2C_7C - 6\ln(C_1L) \\ &\quad - C_7C_1\ln(C_2L^2) - 2C_9\ln(LC_7) + C_9\ln(C_8L^2) + 4tC_7\arctan\left(\frac{C_7}{t}\right) \\ &\quad - 4tC_7\arctan\left(\frac{C_1}{t}\right) + t^2(\ln C_2 - \ln C_8)\Big\}\end{aligned} \tag{6.26}$$

where the additional C_x values are given by

$$C_7 = 2r_2 - t \tag{6.27}$$

$$C_8 = 2{r_2}^2 - 2r_2 t + t^2 \tag{6.28}$$

$$C_9 = 4r_2^2 - 4r_2 + t^2 \tag{6.29}$$

Care must be taken during the solution to ensure the correct boundary conditions are held; either by performing indefinite integration and solving for the constants of integration, or by proper use of a dummy variable for definite integration.

Equations 6.19 through 6.29 provide the exact analytic solution to the bending deflection of a tapered beam. Unfortunately, they are a bit unwieldy for design purposes. Great care must be taken just to enter the formulas into a design spreadsheet. Of greater concern, however, is the C_3 term in the denominator of Equation 6.26. This term forms a singularity if there is no taper to the beam!

Ideally, Equation 6.26 should be valid for both tapered and straight beams, with only the substitution of identical radii at both ends needed for straight beams. However, since $C_3 = r_2 - r_1 = 0$ for straight beams, there are multiple singularities in Equation 6.26, not just the C_3 term in the denominator, but also in the $\ln(C_3)$ terms elsewhere. The source of these singularities is apparent, however, in the parameterization of the moment of area in Equation 6.17. The linear variation of radius with x results in x begin directly multiplied by C_3. While the moment of area is still well defined if $C_3 = 0$, the integration of Equation 6.1 proceeds under the assumption that x terms lie in the denominator. Indeed, these terms are the complication that led to the use of MAPLE. It is apparent that these terms are necessary for the solution to be valid.

If the beam is straight, it is relatively easy to compute the deflection with a constant moment of area I, and this is well documented in countless texts. Numerical comparison of this result with that of Equation 6.26 shows what appears to be a monotonic convergence of deflection towards the analytic value as $r_2 \rightarrow r_1$. However, once $r_2 \approx r_1$, oscillations begin in the deflection, until total divergence at $r_2 = r_1$.

This result is not unexpected, and actually quite satisfying. The initial apparent convergence gives confidence in the results when $r_2 < r_1$, and proves to be a nice "sanity check" on Equation 6.26. The results appear quite stable until the difference between r_2 and r_1 is very small, and should be useful if a beam has any appreciable amount of taper.

6.4.2 Tapered Tubes - Approximate Bending Stiffness

The cumbersome nature of the exact solution to the bending of tapered tube, in Equation 6.26, makes an approximate solution very desirable. Unlike the solution of the notch flexure in Equation 6.6, the exact solution to the tapered tube in bending cannot be easily simplified by making assumptions about any values or ratios being $\ll 1$. Instead, recall the original difficulty with the integration of the beam equilibrium equation - the complicated moment of inertia term, in Equation 6.17. If this term can be simplified, the resulting integral will be much more tractable.

An approximation to Equation 6.17 can be made if the thickness of the tube $t \ll r$. With this assumption, the area of the cross section can be viewed as being distributed at a constant radius r. An approximation of cross sectional area is then given by $A = \text{length} \cdot \text{width}$, or $A = (2\pi r) \cdot t$. Here, $r = r_{outer}$ is chosen for convenience, although $r = r_{inner}$ would produce a more conservative estimate of stiffness. Recall that the polar moment of inertia of a cross section is $J = \int r^2 dA$[27]. Since the area is viewed as being distributed at a constant radius, we have $J = r^2 A$ or $J = 2\pi t r^3$. Note that $J = I_x + I_y$, and that for a circular cross section, any choice of coordinates with an origin at the center will produce $I_x = I_y$. Thus $J = 2I$ and

$$I = \pi t r_{outer}^3 \tag{6.30}$$

Substituting a linear variation in radius, as in Equation 6.17, from a radius r_1 at the base to a radius r_2 at the tip, yields

$$I = \pi t \left(\frac{(r_2 - r_1)x}{L} + r_1 \right)^3 \tag{6.31}$$

This expression, along with Equation 6.18, can be used to integrate Equation 6.1 for a tapered tube. The approximation to the inertia makes the solution much easier than in the exact case. Using a table of integrals, or symbolics mathematics software, gives the following result for the slope at a location x in the beam.

$$\theta = \frac{dy}{dx} = \frac{-FL^2[2r_1(x-L) - r_2x]x}{2r_1^2t\pi E[r_1(x-L) - r_2x]^2} \tag{6.32}$$

Equation 6.32 can be integrated again, and evaluated at $x = L$, to find the deflection at the tip of the beam

$$y = \frac{-FL^3(2r_1^2[\ln(-r_1) - \ln(-r_2)] - 3r_1^2 + 4r_1r_2 - r_2^2)}{2E\pi tr_1^2(r_2 - r_1)^3} \tag{6.33}$$

Unfortunately, it initially appears that this equation will be problematic. Not only does it have the singularity when the beam is not tapered, but the logarithmic terms $[\ln(-r_1) - \ln(-r_2)]$ have negative arguments, which will produce complex results. Fortunately, the identity $\ln(ab) = ln(a) + ln(b)$ can be applied to each term, such that

$$\begin{aligned} \ln(-r_1) - \ln(-r_2) &= \ln(-1) + \ln(r_1) - \ln(-1) - \ln(r_2) \\ &= \ln(r_1) - \ln(r_2) \end{aligned} \tag{6.34}$$

Thus the deflection at the tip is given by

$$y = \frac{-FL^3(2r_1^2[\ln(-r_1) - \ln(-r_2)] - 3r_1^2 + 4r_1r_2 - r_2^2)}{2E\pi tr_1^2(r_2 - r_1)^3} \tag{6.35}$$

Equation 6.35 provides a much easier method for evaluating the deflection of tapered tubes in bending than the exact solution presented in Equation 6.26. It still suffers from the same singularity when $r_2 = r_1$. The designer must also be aware that the fundamental assumption for this approximation is that $t \ll r$. Generally, it is best used when $t < \frac{1}{10}r$. Note also that if r_1 and r_2 can be taken from inner or outer radii; inner radii will error towards more deflection, outer radii will error towards

stiffer structures. As long as care is taken in meeting the assumption, Equation 6.35 can be used very effectively.

6.4.3 Tapered Tubes - Torsional Stiffness

Offset cutting forces can generate significant torsional loads on any supporting tool structure. For many prismatic beams, this is a weakness; not all shapes which generate good bending stiffness can support torsional loads well. Fortunately for the tapered tube, its circular cross section is not only relatively easy to evaluate analytically, but is the most torsionally stiff shape.

For a linear elastic material, the total angular deflection of a circular shaft subjected to a torsional load T is

$$\phi = \int_0^L \frac{T dx}{GJ} \tag{6.36}$$

where ϕ is the angular deflection in radians, G is the shear modulus of the material, L is the length of the shaft, and J is the polar moment of inertia for the cross section. As noted earlier, for a circular cross section $J = 2I$. Hence Equation 6.17 can be doubled and substituted into Equation 6.36. Evaluating this integral gives

$$\phi = \frac{TL[2\ln(C_7 L) - \ln(C_8 L^2) - 2\ln(C_1 L) + \ln(C_2 L)]}{G\pi t^3 C_3} \tag{6.37}$$

where the C_x values are the same as those in Section 6.4.1. Like the solutions in Section 6.4.1, this is a functional, but unwieldy solution.

The same approximation methods to the moment of inertia used in Section 6.4.2 can also be applied here. Doubling Equation 6.31 and substituting into Equation 6.36 for J, the integral can be evaluated to find

$$\phi = \frac{TL(r_1 + r_2)}{4Gt\pi r_1^2 r_2^2} \tag{6.38}$$

This form is much more tractable than Equation 6.37 and easier to evaluate. It is still subject to the assumption that $t \ll r$ as noted in Section 6.4.2.

6.5 Conclusions

This chapter presented the basic elements required to build a precision mechanism, including bearings, actuators, and structural elements. All of these elements are required to design an integrated tool height adjustment for the toolarm. The tapered tube analysis I have developed will be of particular use in designing structures that are both stiff and of low inertia. The design parameters presented here will be exploited in the following chapter to perform detailed design of several of the concepts presented in Chapter 5

Chapter 7

Detailed Design of Toolarm

In this chapter, I develop several of the concepts presented in Chapter 5 into detailed designs, using the elements presented in Chapter 6. While optimizing these concepts for performance and manufacturability, a new "double-diaphragm" actuator design is developed. The other designs detailed initially could likely be made into successful toolarms, but based on ease-of-fabrication, low inertia, and high stiffness, the "double-diaphragm" design was selected for incorporation into the RFTS. This chapter documents the development of the initial designs and shows how they led to the design of the new actuator and toolarm.

7.1 Wedge Drive Arm Design

The wedge drive design concept (Concept 12) showed several advantages over the other designs. These include:

- Rotational Movement - requires less strain in flexural mounts, since the strain is amplified by the length of the arm.
- Preservation of other calibration settings while height is adjusted - minimal parasitic motions.
- Wedge actuator helps maintain stiffness, since the larger actuation forces allow flexural elements to have higher spring rates, and provides a line contact zone.

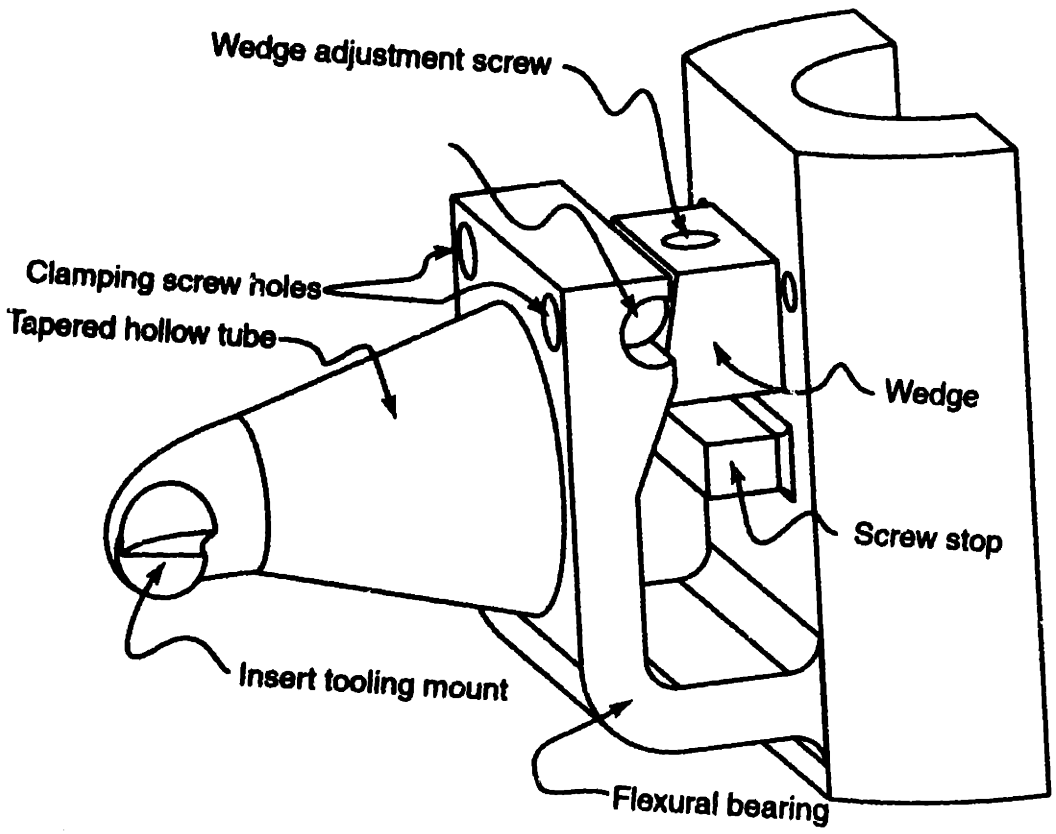

Figure 7-1: Wedge arm actuator.

Based on these advantages, further detailed design was conducted. This design is shown in Figure 7-1.

7.1.1 Flexural Pivot

As shown in Chapter 6, there are many types of flexural pivot bearings suitable for providing rotational motion. For this design, single strip notch and beam flexures will be considered. This will allow the flexure to be easily made in a monolithic fashion, and integrated into the structure. Clamped designs would require more difficult assembly and likely compromise bearing stiffness. Several parameters need to be specified for the design of the flexural bearing. First, the desired range of travel needs to be determined, based on the functional requirements. Next, the material used to construct the bearing needs to be specified. This will allow the appropriate geometry to be chosen.

Travel Range (μm)		Angular Change	
Unidirectional	Bidirectional	(mrad)	(°)
5	10	0.10	0.006
10	20	0.20	0.011
20	40	0.40	0.023
50	100	1.00	0.057
100	200	2.00	0.115
150	300	3.00	0.172
250	500	5.00	0.286

Table 7.1: Angular change required for tool height travel, 50 mm arm length.

The range of travel of the bearing is not a simple specification, since more travel is always desirable, yet excessive travel will lead to decreased stiffness in the system if the flexure needs to be too thin. The question is really to find an acceptable constraint on the travel. Hence the specification needs to take place with some examination of the required geometry for various travel ranges. For a good estimate of the angular flexure required for various travels, a 50 mm arm length is assumed. This is the nominal 80 mm arm with 12.7 mm subtracted for tool shaft clearance and an additional 17.3 mm subtracted to allow for the flexure and some base material. This allowed the travel ranges in Table 7.1 to be determined.

The two material properties which most directly effect the bearing performance are the elastic modulus and the yield strength. As shown in Equation 6.9, the maximum deflection of the flexure is directly proportional to $\frac{\sigma_{max}}{E}$. Generally, one would want a material with a high strength, but low modulus. Of the common engineering materials, aluminum would fit this nicely, as it is more flexible than ferrous based alloys but can have a comparable as-delivered yield strength. (Ferrous alloys can obtain much higher strengths than aluminum through proper heat-treatment). However, there are other factors for the material choice in this design. Since it is desired to produce a monolithic bearing integral with the structure, the structure must have identical material properties. This makes aluminum much less attractive, since the structure should be as stiff as possible. Typically, when aluminum is substituted for steel, the moment of inertia of the cross section can be increased to compensate, but this design is limited by geometric constraints. Any design made from aluminum can

be stiffened by substituting a ferrous alloy.

An additional consideration is the method of manufacture. For this design, the intent was to explore investment casting as a manufacturing method. This would allow reasonably high tolerance parts to be produced with complex shapes. These requirements led to "ductile" cast iron to be used as the design material, as it is an easily cast material with desirable properties. The modulus of ductile iron is usually quoted to be ≈165 GPa, but the *ASM Metals Handbook*[4] notes that for flexural structures such as a cantilever beam, a more appropriate value is ≈140 GPa, based on actual deflections. This is approximately twice the stiffness of aluminum. The yield strength, like many ferrous alloys, can be determined by heat treatment, but it is possible to achieve 310 MPa as cast, with a 12% strain at failure, indicating a strong, ductile alloy that is suitable for flexures. Another desirable property is a damping capacity about 6.6 times that of common steel, although still much less than typical grey cast irons.

Using this material and Equation 6.9, a sample hinge with R = 12mm and t = 5mm was chosen. This would provide a travel of more than 250 μm as shown in Table 7.1 if the material was stressed to its elastic limit. Given that the deflection $D \approx R\theta$, and that θ is linear with σ_{max}, the deflection can be linearly scaled by the desired factor of safety. A finite element model of this hinge was then developed in ANSYS and tested to compare with the analytic results, as shown in Figure 7-2. An actuating force, acting in the compressive longitudinal direction, was offset from the neutral axis of the hinge to provide a bending moment. A pure bending moment could have been better approximated with a force couple, since moments cannot be directly applied to a plane stress model. However, it is more desirable to model the actual real world conditions, and apply the force in the manner of the actuator. Agreement between the analytic solution and the finite element model then does not just validate the FEM but also validates the analytic assumptions.

Post-processing the FEA results, it was found that the maximum flexural stress exceeded the analytical expectation by ≈12%, and the angular displacement, found by the angle of the line formed on the underside of the notch hinge, exceeded the

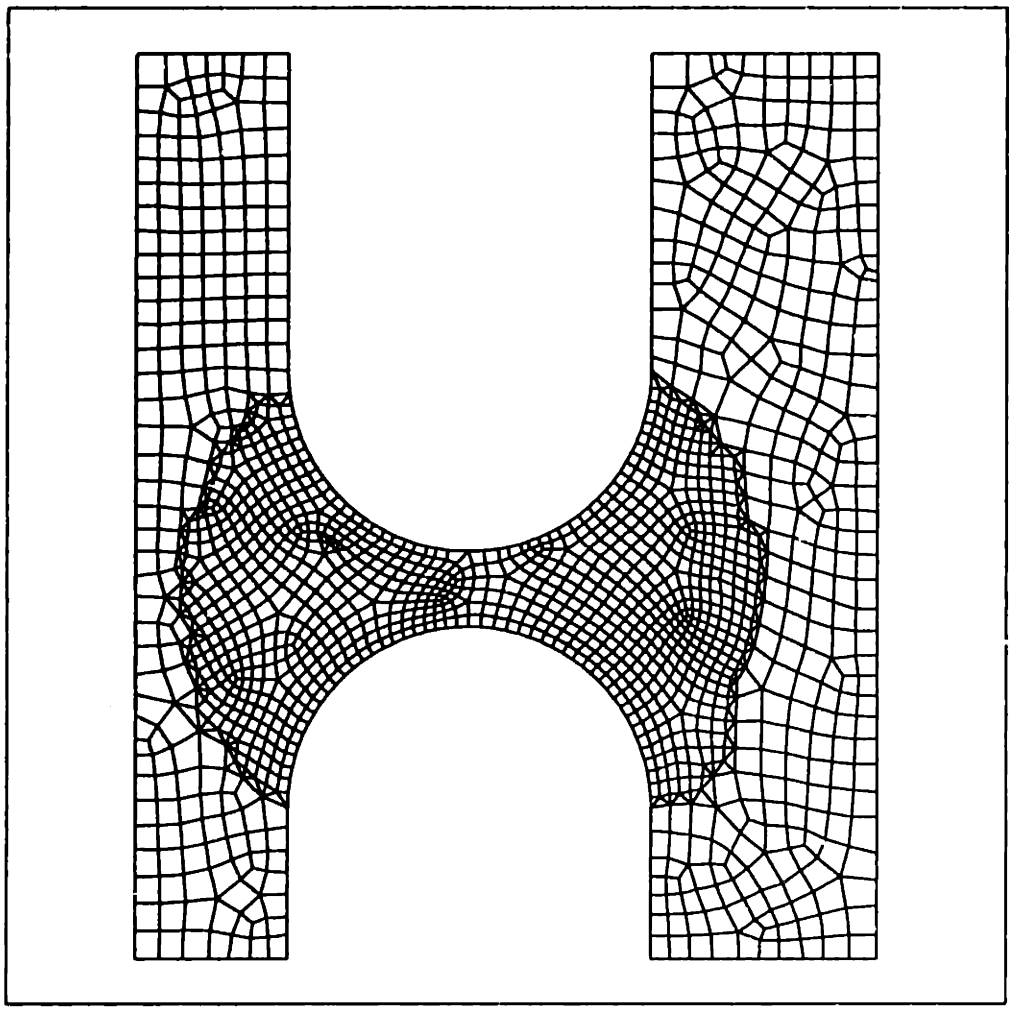

Figure 7-2: Finite element of model of notch hinge bearing.

expectation by ≈13%. This may seem odd, as the finite element solution should converge to the exact solution from *lower displacements*, as noted in the development of finite element theory by Bathe[2]. However, the results are being compared against an analytic model which assumes only a bending moment and neglects shear effects. Therefore these can be considered good results, and finite element process can be trusted. It is important to always check any computer simulation with a basic model such as this one, and build confidence that the process is sound, before progressing to more complex models.

Once this initial geometry was chosen, the design evolved further. Other considerations began to enter into the design, such as the functional requirement for low rotary inertia (Section 4.4). With this in mind, it seems as though any "notch" hinge, while preserving kinematics, carries excess mass. The flexural pivot is to be mounted low on the arm, as in the conceptual sketches, in order to help increase the resolution of the actuator (by giving it a longer lever arm about the pivot), and to help increase the torsional stiffness, by moving its area inertia and that of the actuator as far apart as possible. If the arm is mounted above the notch hinge, however, the bottom portion of the hinge below the pivot point will be supporting little load and add some mass to the system.

In order to reduce the mass of the hinge, the design was changed to move from a notch hinge to a curved-beam hinge (as illustrated in Figure 7-1, which would blend more smoothly into the structure. This was accomplished in two steps, first by converting the notch into a straight beam hinge, checking it with ANSYS, and then converting to the full curved beam, as shown in Figure 7-3. The larger strain area allowed the thickness of the hinge to be increased to help stiffen against off-axis deflections, while preserving the angular deflection capability. The ANSYS results shown in the figure confirmed the deflection of the hinge and the required actuation forces, which are quite large, about 800 N for 8 mrad deflection. Note the figure shows additional details of the geometry required for integrating the actuator.

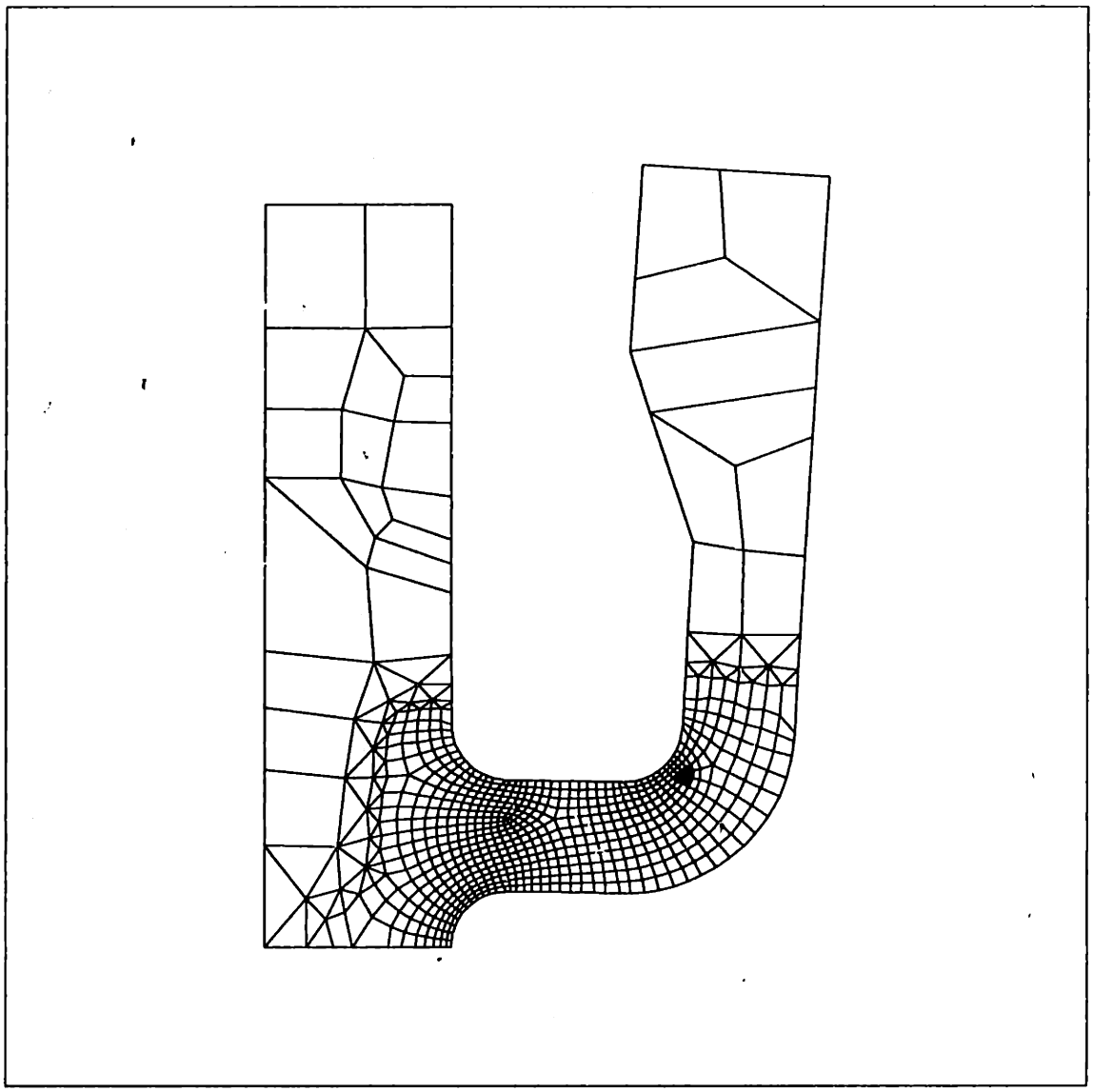

Figure 7-3: Deformed mesh of curved beam hinge.

7.1.2 Wedge Actuator

A wedge is often used as a means of both increasing the resolution of a screw and increasing its force as an actuator. The wedge drive arm design should exploit both of these features for optimal performance. However, there are several issues that need to be confronted during implementation.

The force multiplication advantages of a wedge appear very good at first glance. Constructing a basic energy balance, $Force_{out} \cdot Distance_{out} = Force_{in} \cdot Distance_{in}$, one might conclude that a significant force multiplication can take place, since $Distance_{out} \ll Distance_{in}$ for a small slope wedge. Unfortunately, wedges are often not very efficient due to frictional forces, which create an energy loss term which needs to be considered. A direct force balance is a more appropriate modeling of the problem.

For a quick evaluation of the magnitude of the frictional effects, consider a sliding the middle plate in a stack of three parallel plates, loaded by a normal force F_N. This middle plate is a good approximation to a small slope wedge. The frictional force at each interface is $F = \mu F_N$, so the total frictional force that needs to be overcome by an actuator is

$$F_r \approx 2\mu F_N \tag{7.1}$$

If the static coefficients of friction for clean steel on steel, $\mu \approx 0.8$ or cast iron on cast iron, $\mu \approx 0.4$, are used, it is easy to see that the force required to move the plate can be greater than the normal force F_N! Thus, for small slope wedges, the force required to move the wedge can be greater than the actuation force output, and no force multiplication is provided. Lubrication can significantly reduce these coefficients of friction, down to $\mu \approx 0.2$ for both cases, but the frictional losses will still be considerable. If the actuation forces are significant compared to the stiffness of the actuating screw, significant "stick-slip" conditions can result, making adjustment difficult.

It is possible to avoid these problems by not making the wedge an actuator, but merely a position reference. That is, the wedge moves freely, with no loading, and another clamp screw pulls the arm into position against the wedge. To adjust, that

screw is loosened, the wedge is moved, and the clamp screw again pulls the arm into position against the wedge. The difficulty here is that is it not possible to have a direct readout of the arm position during adjustment, and some iteration will need to take place.

An additional issue with the wedge actuator arises in ensuring the desired resolution. Since the flexural bearing supporting the arm is a rotational bearing, there is only one configuration of the arm in which all of the wedge bearing interfaces are parallel. As the wedge moves from this configuration, it is likely that a line contact will develop at one edge of the wedge or bearing surface. This changing contact area and kinematic configuration makes consistent high resolution positioning difficult. This problem is only worsened by any clamping screws used to lock the position, as they will tend to bend the interfaces back into complete contact, and could deform the structure further.

To alleviate this problem, one bearing surface can be replaced with a cylindrical surface. This will ensure a consistent line contact at one bearing interface, between the flat and the cylinder, and provide much better positioning resolution. The configuration is still not totally ideal from a kinematic standpoint, as the cylinder and plane may not be totally parallel. However, improving this kinematically by the point contact of a sphere as opposed to a cylinder would lead to undesirable tradeoffs in the stiffness of the interface, and permit too much "rocking" to be caused by tightening any offset clamping screws. Figure 7-4 illustrates the actuator.

The interface of the cylinder on the wedge, however, can lead to very high stresses when the clamping screws are tightened. The line contact causes infinite stresses at the interface, which will quickly be reduced as the material elastically deforms to accommodate the stress. This is "Hertzian" contact stress, with the larger stresses occuring in the flat surface of the wedge. It is important to ensure that such deformation remains elastic, as any plastic deformation will result in detents forming on the surfaces, which will make adjustment extremely difficult. In addition, it is desirable to design the interface so that a minimal amount of deformation occurs, so that the tool height is negligibly affected by the tightening of the clamping screws.

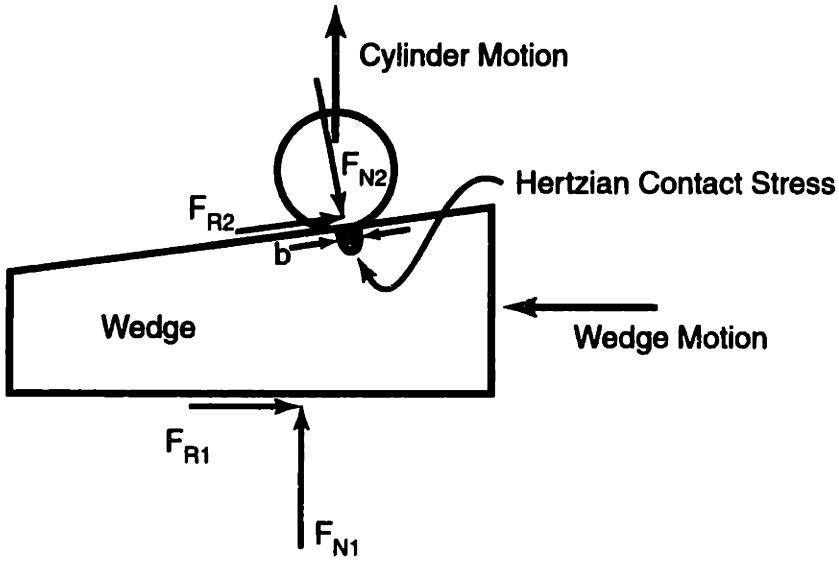

Figure 7-4: Wedge actuator forces and stress zone.

The contact stress between a cylinder and a plane may be found from the contact stress between two cylinders, and setting the radius of one cylinder to infinity. The solution this problem is well documented in texts such as those by Shigley[27] or Roark[38]. If we further assume that the materials of both the cylinder and wedge are identical, giving identical moduli of elasticity $E_1 = E_2 = E$, and are common engineering materials with a Poisson's ratio of $\nu = 0.3$, the width of the contact zone b is given by

$$b = 2.15\sqrt{\frac{FD}{LE}} \tag{7.2}$$

where F is the applied force and D is the diameter of the cylinder, while L is its length. The maximum contact stress is slightly higher than a simple force divided by area approximation, since it various over the area. The maximum value is given by

$$\sigma_c = 0.591\sqrt{\frac{FE}{DL}} \tag{7.3}$$

To estimate the deformation at the interface, it is necessary to return to the more general theory of the change in center distance between two cylinders, given by

$$\delta = 0.579\frac{F}{LE}\left(\frac{2}{3} + \ln\frac{2D}{b} + \ln\frac{2D_2}{b}\right) \tag{7.4}$$

Here, D_2 is the "diameter" of the second sphere, or the flat bearing surface, and a suitable large number can be substituted. With the "diameter" of the wedge D_2 now included, the sensitivity of the deformation to this parameter can be examined, but should be relatively small.

Ideally, a wedge and cylinder follower should be designed from Equations 7.3 and 7.4 which does not deform enough to significantly affect the tool height. The practical limits on the cylinder diameter prevent this from being possible. The high stresses involved dictate that the cylinder should be an insert into the arm structure, since the ductile iron should not be hardened as this would result in brittle flexures. An insert could be constructed which has a vary large radius machined on one side, but it is most practical to use a pressed in hardened steel dowel pin as the cylinder. Choosing a 0.25 in. diameter pin, it is found that the clamping screws can be tightened to $\sim$ 200 lbf. each while keeping the contact stresses below 100 ksi. The wedge and pin can be hardened to easily survive such loading. More importantly, variation in the clamping screw force by $\pm 15\%$ results in a variation in deformation of only 1 μm – this repeatability will make adjusting the tool height much easier.

7.1.3 Arm Extension

Once the bearing and actuator system were designed, the arm was extended to hold the tooling. For this first design, it was decided to stay with the polycrystalline diamond (PCD) insert tooling, since it was readily available. Using the interface overlays developed in Section 4.3.3, the arm was extended in a tapered beam to hold the tool, while simultaneously avoiding any lens interference. Equations 6.35 and 6.38 indicate that the toolarm should have a estimated stiffness of over 600 $\frac{N}{\mu m}$, but while this includes torsion, it neglects the bending of the stub end; the actuator system will also increase this compliance.

7.1.4 Manufacture

The structure of this toolarm was designed from the start to be cast from ductile iron. The complex and hollow structure of the arm could not be easily reproduced with conventional machine tools. Casting is often considered as a technique for rapidly producing quantities of roughly toleranced parts. Considerable expense and effort must often be expended in making the molds when the parts are complex, although the molds for simple parts may be quite inexpensive.

The conventional casting process, however, is rapidly changing in the face of new "CAD to cast" techniques. These make it much simpler to produce small lots of prototype parts, even when incorporating relatively complex geometry, using a new investment casting process. The geometry of the part is first designed in a three dimensional solid modeling program, such as the Pro/ENGINEER software used in this work. The geometric information is then transferred to a rapid prototyping system which can quickly produce a full scale model of the part. Several different rapid prototyping techniques, such as selective laser sintering or three-dimensional printing can be used, but they must produce the model out of a suitable material. In the case of three-dimensional printing, a cellulose based material is used. This model is then dipped in a slurry of refractory material, dried, and then coated again several times to increase its thickness. The model can then be burned or melted out of this coating, which then forms a mold for metal casting.

After casting the bearing surfaces for the wedge actuator are unlikely to have a sufficiently smooth surface for good operation. The cylindrical surface can easily be added to the part by pressing in a hardened steel dowel pin. But the opposite surface, nearest the shaft, will require a secondary machining operation. Grinding would be ideal, but it is difficult to fit any wheel in the available space. Electron-Discharge Machining (EDM) may be a better solution.

In any case, the manufacturing difficulties led to the exploration of other design options. Not only would the secondary machining be complicated, but the casting process could lead to unforseen problems. "CAD to cast" techniques allow very

complex shapes to be easily cast in theory, but good casting design requires careful consideration of the part cooling in the mold. Thermal differences as the part cools can lead to porosity, voids, and stresses in the cast part, ultimately leading to failure of the piece. Good casting design will design the parts to avoid these problems, but given our lack of experience in this area, it was prudent to consider other ideas.

7.2 Monolithic Bearing and Actuator Design

7.2.1 Design

A new design effort was conducted to produce a toolarm design which contained a monolithic bearing and actuator system. This idea uses a similar rotational bearing to the "wedge-arm" design, but the wedge reduction mechanism is instead replaced by an integrated lever system. The monolithic nature of the design should eliminate several of the difficulties in the previous "wedge actuator" arm design, as the only moving parts should be actuating screws. The sliding contact present in the wedge is eliminated, reducing the possibility of "stick-slip" occuring during adjustment, or encountering detents in the wedge from Hertzian contact stresses.

The manufacturability of the design is greatly enhanced by the removal of the bearing surfaces. That is the central goal of this new study – to design a toolarm which can be produced with the equipment present in our on-site machine shop. One machine which can be used to cut flexures is our waterjet machining center. This machine uses a 40,000 psi jet of water, mixed with abrasive, to cut most materials. The nature of the process, however, also prevents the machine from cutting anything but two-dimensional sections, to an accuracy of about ± 0.005 in. For this reason the new design will be completely two dimensional, which will prevent implementation of the tapered beam construction used earlier.

Figure 7-5 presents several possible monolithic configurations. Only the bearing system and actuator is shown. Each consists of an actuation beam coupled to a "mounting beam" which would support the rest of the arm structure. The actuation

beam is driven by an adjustment screw and moves the mounting beam as a lever transmission mechanism, which in turn moves the final tool endpoint via the arm. The tool height relationship for any of these configurations can be expressed as

$$\Delta h = \frac{l_2 L}{l_1 l_3}\delta \tag{7.5}$$

where Δh is the change in tool height, δ is the movement of the adjusting screw, and l_1,l_2,l_3 are the lengths of the actuation, intermediate, and mounting beams, respectively, and L would be the additional length of the tool support structure. Configurations (a),(b), and (c) respectively increase the resolution of the actuating screws by approximately 5.7, 5.4, and 4.8, given $L = 50$ mm and the other dimensions scaled appropriately. Any of these configurations should provide sufficient resolution for the tool height adjustment, as they can make a common 32-pitch fastener the equivalent of a $\sim$ 150-pitch fine adjust screw on the endpoint.

Each configuration has additional advantages and disadvantages. In configuration (a), the actuating screws are easily accessed for adjustment, but mounting the rest of the arm structure is more problematic. The arm will need to "wrap around" the actuating beam to reach the mounting beam, possibly compromising stiffness in the structure. In configurations (b) and (c), the arm structure can be easily attached to the mounting beam, but access to the adjustment screws will be difficult.

The kinematics of the different configurations also affect the maximum range of adjustment. In configurations (a) and (b), the intermediate flexure F_2 is required to under go a deflection $F_2 = F_1 + F_3$, since the actuation beam and mounting beams rotate in opposite directions. In configuration (c), the two beams rotate in the same direction, and hence the intermediate flexure undergoes a deflection $F_2 = F_1 - F_3$. This will allow configuration (c) to obtain a range of travel $\sim$ 25% greater than the others. Note that the actuation beam of configuration (c) is narrower at one end. Since the actuator will see the load of any imposed forces on the arm, this will result in lower stiffness.

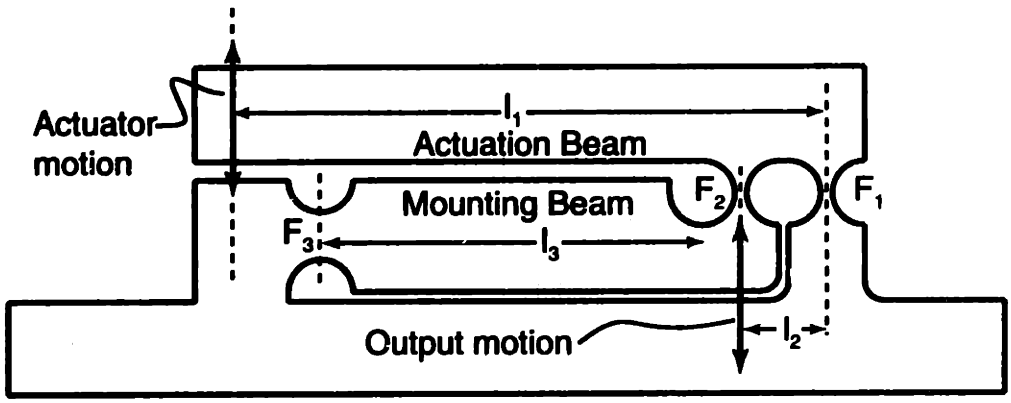

(a)

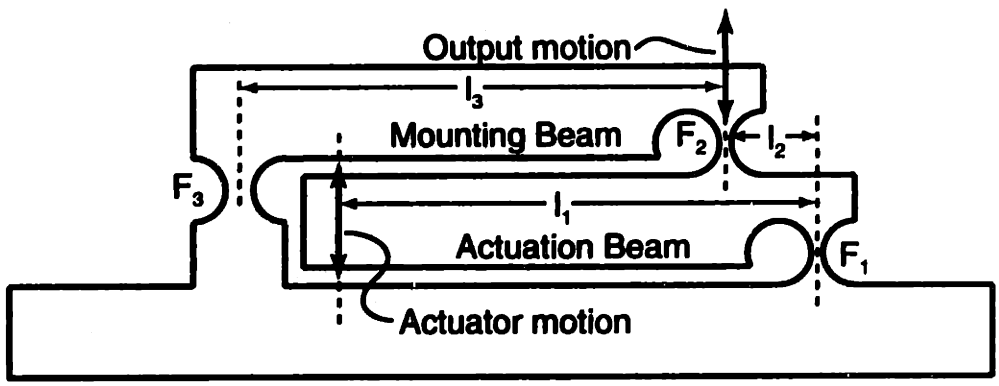

(b)

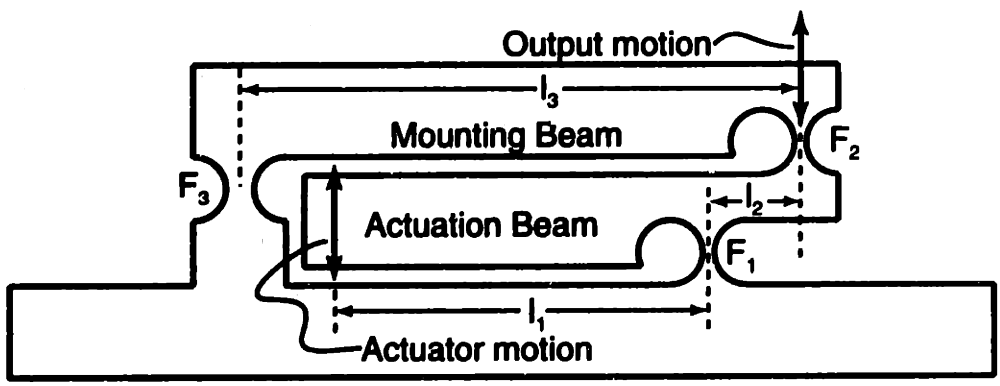

(c)

Figure 7-5: Several configurations for monolithic bearing and actuator systems.

7.2.2 Manufacture

In order to further evaluate the performance and manufacturability of this concept, a prototype was manufactured for each configuration to be compared against finite element results. The size of each of the flexures was developed using Equation 6.9. The range of travel of the flexures is limited by space considerations, since the mechanism must be kept as close to the toolshaft as possible in order to reduce rotational inertia. Configurations (a) and (b) provide about ± 100 μm tool adjustment, while (c) provides ± 125 μm, based on mild steel construction. The actuation and mounting beams were also sized based on space; for an actual toolarm, these would need to be optimized for not only bending strength, but also low inertia. This would likely be accomplished by using wide beams and cross-drilling them. This would remove the inertia increasing material while maintaining the bending stiffness.

Figure 7-6 shows two of the three finished prototypes. Aluminum pieces were bolted to the mounting beams, so that the motion of the toolpoint could be measured. Unfortunately, there were severe problems with the waterjet machine during manufacture. The machine's water pump was worn, resulting in a lower pressure jet; this prevented effective cutting of the 1.125 in. thick steel. The nozzle on the machine frequently clogged with abrasive, and the total cutting time increased to upwards of 8 hours for one part, instead of the planned two hours.

These problems led to the production of very inaccurate parts. The beam thicknesses in configurations (b) and (c) were much thinner than designed, with the result that they could not function. The beam bending stiffness was less than that of the flexures, so the actuation screws simply bent the beams! Configuration (a) performed as designed, with an effective travel of ± 100 μm, and sub-micron resolution, as verified on a capacitance gauge. Given the difficulty in manufacturing, it did not seem that it would be possible for a complete arm to be successfully manufactured in-house. Additionally, minimization of the inertia of these structures seemed difficult. As a result, more designs were studied.

Figure 7-6: Photo of two monolithic actuator prototypes.

7.3 Final Toolarm Design

The previous design efforts had developed toolarms which likely could be made to work, but seemed less than ideal. The wedge was designed to be investment cast, which could require considerable lead time, especially considering the lack of vendor contact and experience within our research group. The monolithic bearing and actuator design appeared more difficult to optimize for low rotary inertia. One more concept would be researched, that of Concept #10, using continuum deformation of a beam. The desire was to make a design completely manufacturable by a well-equipped machine shop, so the toolarm could be manufactured as quickly as possible. The design should make even greater use of two-dimensional sections than the monolithic bearing and actuator design, with the arm itself two-dimensional as well. This would allow the arm to be produced by the Wire Electron Discharge Machining (EDM) process, which uses a thin wire to "slice" through conductive materials. The wire does not actually cut the material, but instead erodes it with many tiny sparks. It is a very accurate, if slow, process that can create exceptionally thin and deep two-dimensional

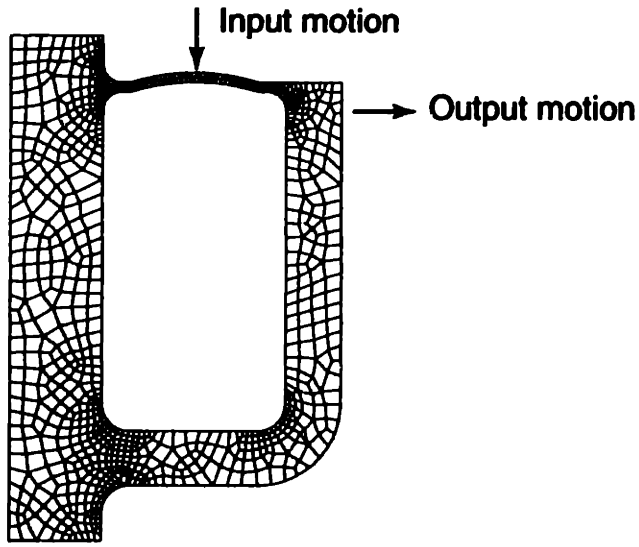

Figure 7-7: ANSYS model of diaphragm actuator.

sections, making it ideal for producing flexures.

7.3.1 Development of a novel "Double-Diaphragm" toolarm concept

The design calls for a toolarm which is very stiff to cutting forces, so it seemed unlikely that the whole toolarm could be made to deform as a beam. Although actuating forces could be much larger than the cutting forces, this approach would still seem to compromise necessary stiffness. Instead, the concept was modified, so that deformation of a smaller section would cause a rigid body rotation of the toolarm about a pivot. The first attempts focused on creating a deformable "diaphragm", similar to the beam flexure actuator described in Section 6.3.2.

A first design was evaluated by simply removing the wedge actuator from the previous design and replacing it with a thin strip of metal. The diaphragm was chosen to be 1 mm thick, based purely on manufacturing considerations. This was thought to be the thinnest section that could be easily manufactured with conventional metalcutting methods. The diaphragm was offset in a curve that deflected it 1 mm in the center, over its 14 mm span. This was then analyzed as a 2D section in ANSYS, as shown in Figure 7-7.

This initial model showed several encouraging results, but also revealed some potential problems. The diaphragm actuator performed roughly as expected, based on Equation 6.15, with the desired transmission ratio. However, the total travel for the system was quite small compared to the previous design, with a total travel of approximately 20 μm at the yield stress of the material, which was still the ductile iron. The flexure required relatively high actuation forces, although these could be provided by standard fasteners. The problem with this high actuation force is that it caused direct shear of the beam flexural pivot. This caused an undesirable coupling effect between the motion of the screw and flexure; instead of rotation about the pivot, the flexure translates the arm downward as well. This has the effect of increasing the transmission of motion from the screw, instead of the desired decrease from the diaphragm actuator. The previous wedge based design did not have this problem, as the force acted axially on the flexural pivot. This problem could be compensated for with a notch pivot that is stiffer in shear, but a more decoupled actuator design needed to be undertaken.

7.3.2 Design of "Double-Diaphragm" Actuator

The initial ANSYS analysis led to the design of a new, novel, "double-diaphragm" toolarm actuator concept, illustrated in Figure 7-8[1]. In this design, two diaphragm plates are placed back-to-back for the actuator. These plates can then be squeezed together by conventional screws. One significant problem in our earlier attempt was the high shear force the actuator placed on the toolarm structure and bearing. This force is eliminated in the "double-diaphragm" design, as the forces from the screws cancel each other through the diaphragm plates.

The double-diaphragm design also *doubles* the resolution of the screw, without even considering the transmission effect from the diaphragm. As the screw compresses the top diaphragm, it pulls itself into the bottom diaphragm. However, the bottom diaphragm has a stiffness equal to that of the top diaphragm, and it moves up the

[1]I would like to thank Professor Slocum for his helpful discussions during the development of this design.

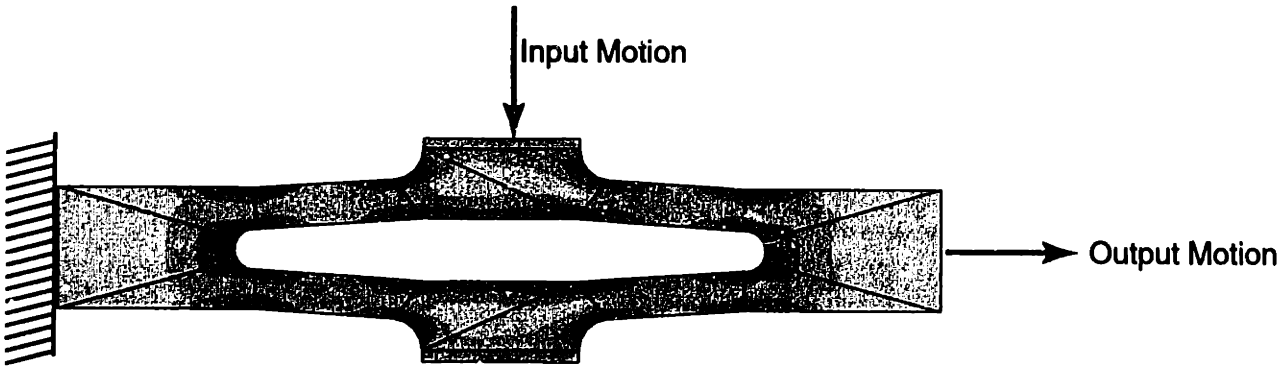

Figure 7-8: Model of "double-diaphragm" actuator.

same distance the top diaphragm was moved down. Thus, if the screw advances a distance x with each turn, the top diaphragm and the bottom diaphragm are each compressed a distance $\frac{x}{2}$.

It quickly became clear that the $\frac{\sigma_{max}}{E}$ relationship that dominates many flexures would limit the ultimate travel of this device. Since the wire-EDM process is not affected by the hardness of the material being cut, hardened 4140 steel was selected to be the toolarm material. This is available prehardened to Rockwell 30 C hardness, which has a yield strength of 1000 MPa, yet is still reasonably ductile to failure.

While finite element analysis is a great tool to analyze the deformation of structures, it is best to begin development with an analytical model. This allows the fastest possible convergence to the final design, since good estimates of the desired parameters can initially be made. The parameters for the length, width, and offset of the center of the diaphragm need to be determined. The offset is important, as it will determine the transmission ratio of the device.

The diaphragm can be modeled as a cantilever beam with fixed-fixed end conditions, as shown in Figure 7-9. The center section of the diaphragm needs screw mounts and is hence much thicker. This thickness will prevent significant deformation, and hence it can simply be subtracted from the total length of the beam, as the slope will be continuous accross it. The deformation of the beam can then be found in a handbook such as *Roark's*[38] and is modeled by

$$y = \frac{-FL^3}{192EI}M = \frac{FL}{8} \tag{7.6}$$

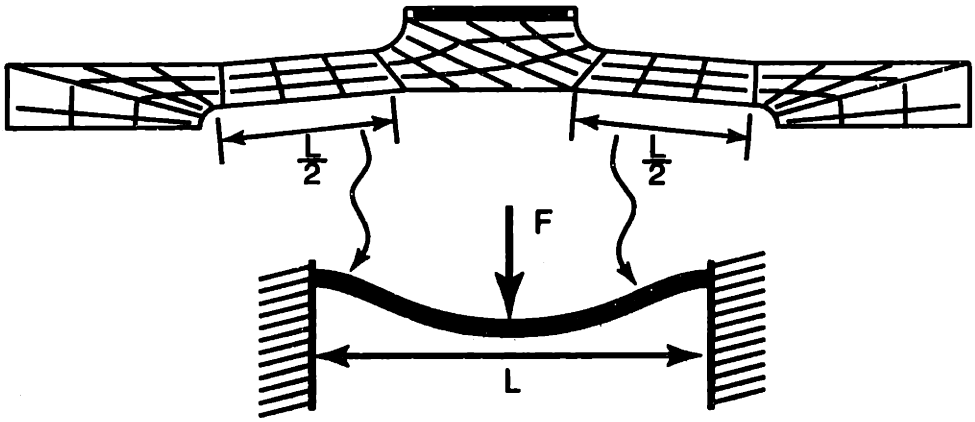

Figure 7-9: Diaphragm can be approximated with a cantilever beam.

where y is the deflection of the beam, F is the applied force, L is the length of the beam, I is the moment of inertia, E is the modulus of elasticity, and M is the maximum bending moment.

Coupling these equations with the limiting stress $\sigma = \frac{Mt}{2I}$, it is possible to choose the rough parameters for the diaphragm which will produce the desired stress state. The transmission ratio can be estimated from 6.15. Finite element analysis can then be used to evaluate the results.

Finite element studies were then used to evaluate several models. Since Equation 7.6 is cubic in nature, it became clear that depending on exactly what was regarded as the free length of the beam, the results could be seen as in agreement with the finite elements. The free length is not exactly clear, since there must be a radius where the beam blends into the structure. Nevertheless, it was relatively easy to come up with results which agreed to within 25%. The final acutator was chosen to have 1.5 mm thick diaphragms with 0.75 mm of offset. The drawings used to produce the arm are found in Appendix A, and illustrate the dimensions.

A prototype actuator was then constructed in the on-site machine shop. Since we do not have a wire EDM, only a 0.75 in. deep section could be machined. This is sufficient to form a test demonstrator, illustrated in Figure 7-10. Testing this actuator found excellent agreement with the finite element results, to the resolution of our gauges, in both the travel and stiffness of this device. Stiffness was tested simply by hanging 10 lbf and 20 lbf weights from the end of the actuator, and measuring the

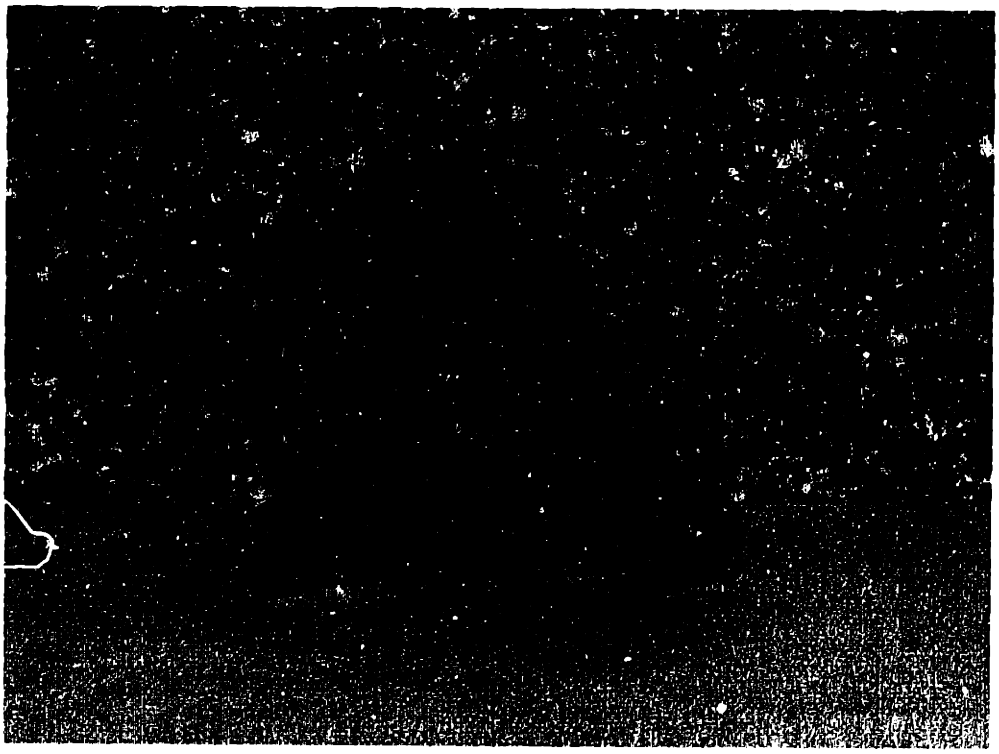

Figure 7-10: Prototype piece used to test "double-diaphram" actuation method.

deflection. Deflection measured 5.5 μm for 90 N of force; note the actual toolarm will be stiffer than this thin prototype, since it is much thicker and has a slightly diffenent configuration.

Actuation screws were chosen to be #8-32 in size, with three of them spanning the top of the actuator. Both diaphragm plates were threaded, which may appear to prevent proper screw movement, but actually allows maximum flexibility. The screws can be configured in a "jam" configuration, where the two outer screws are tightened in the opposite direction of the center screw, locking the position. With both plates threaded, the screws can be configured to either push or pull. To pull like a conventional screw, "captive-type" screws need to be used, which lack threads near their base so there is no interference with the plate being pulled. To push, another short screw can be threaded into the opposite plate, and adjustment screw will push against it.

Figure 7-11: Tooling used in this project. Left to right: tungsten carbide insert, PCD tool on shank, and single crystal diamond tool on shank.

7.3.3 Structure of Toolarm

One major change from the "wedge-actuator" design presented earlier was the decision to accommodate shanked tooling. Single crystal diamond tooling was becoming increasingly attractive to improve the surface finish of the cut lenses, and using shanked tooling would be the easiest method of accommodating these tools. Shanks of $\frac{1}{4}$ in. side length were selected for use, as this is the smallest common size available. These tools are illustrated in Figure 7-11, while Figure 7-12 shows a magnified view of the rake face of a single crystal diamond tool. The nearly perfect edge permits exceptionally fine surface finishes to be obtained.

Contact with PCD and single crystal tool vendors proceeded to develop tools specific to our application. Shank length was kept short, to 0.75 in., in order to limit the added inertia at the end of the toolarm. A long shank is not needed, since the unsupported length of the shank should be minimal to increase the stiffness, while any extra material can have a devastating effect on the inertia, as it is added at the

Figure 7-12: Magnified view ($\sim$ 800$\times$) of the rake face of a single crystal diamond tool.

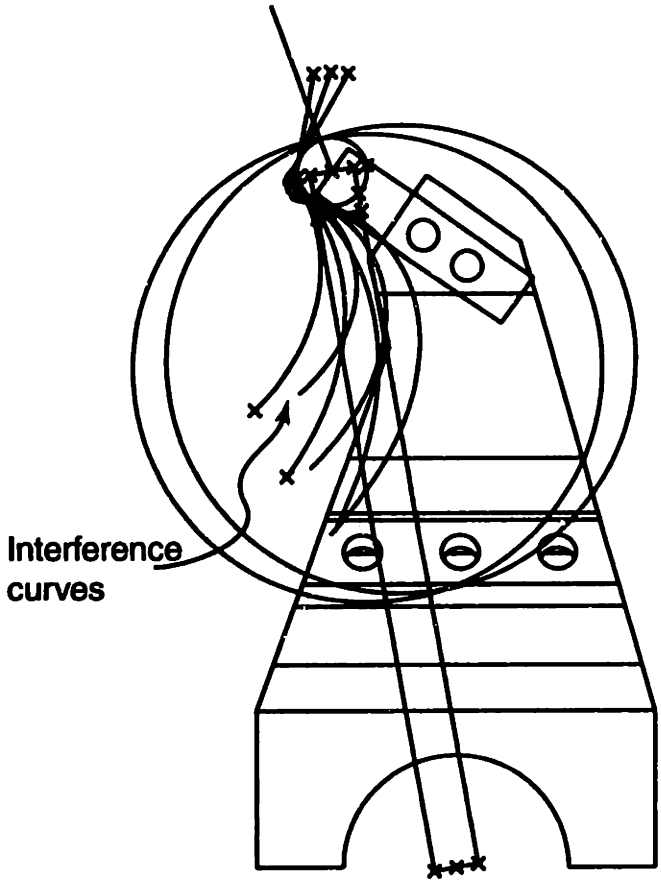

Figure 7-13: Inteference "overlays" used in the design of the toolarm.

maximum radius. Both PCD and single-crystal tools have an edge radius of ~ 4 mm. The single crystal tool is limited to an included angle of 100° on its edge; this required the tool to be carefully oriented on the shank to enable proper cutting.

The toolarm consists of a triangular truss structure, supported by a flexural bearing at the bottom and the "double-diaphragm" actuator at the top. As shown in Figure 7-13, the interference overlays generated in Section 4.3.3 were used to create a "dog-leg" holding the tool to avoid lens interference. These overlays are planar; since the toolarm has thickness out of the plane, it is still possible to generate interference with arm height. This can be avoided by keeping some separation distance from the interference line, since the lens radii are much larger than the thickness of the toolarm.

The shank itself is supported in a steel "box" at the end of the truss. Four #6-32 setscrews secure the tool shank; two press the shank vertically, and two horizontally.

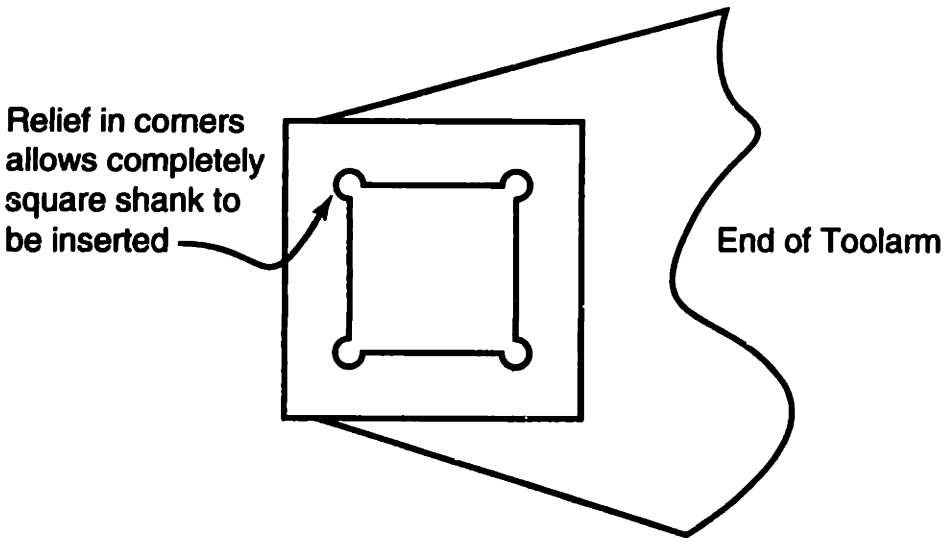

Figure 7-14: Relieved corners permit square tool to be held with minimal additional wall clearance.

The #6 screws were the largest size screws that could be practically used. The corners of the box are specified to be relieved slightly, with no radius, so that a true square shank may fit with minimal additional wall clearance. This can easily be done with the Wire-EDM, as shown in Figure7-14.

By maintaining the flat-sided, two-dimensional nature to the structure, further improvements to the stiffness and damping can be made in the future. Structural adhesives can be used to bond flat panels to the sides of the toolarm, as illustrated in Figure 7-15; this could greatly increase its bending stiffness about the axis of rotation. Similarly, damping could be incorporated into the structure by adding alternating layers of viscous and structural material; Slocum[29] and Nayfeh[21] develop concepts for structural damping in detail.

Once the final geometric design was established, the inertia was minimized iteratively, with several passes of finite element analysis. The arm was subjected to a static, 100 N load in the approximate resultant cutting force direction. Holes were placed in areas of low stress, so that material could be removed without adversely affecting stiffness. One large improvement came with the removal of the material in the "tapered-hole" illustrated in Figure 7-16. This hole increases in size through the arm as it follows the angle of the tool. The material that was previously present added a

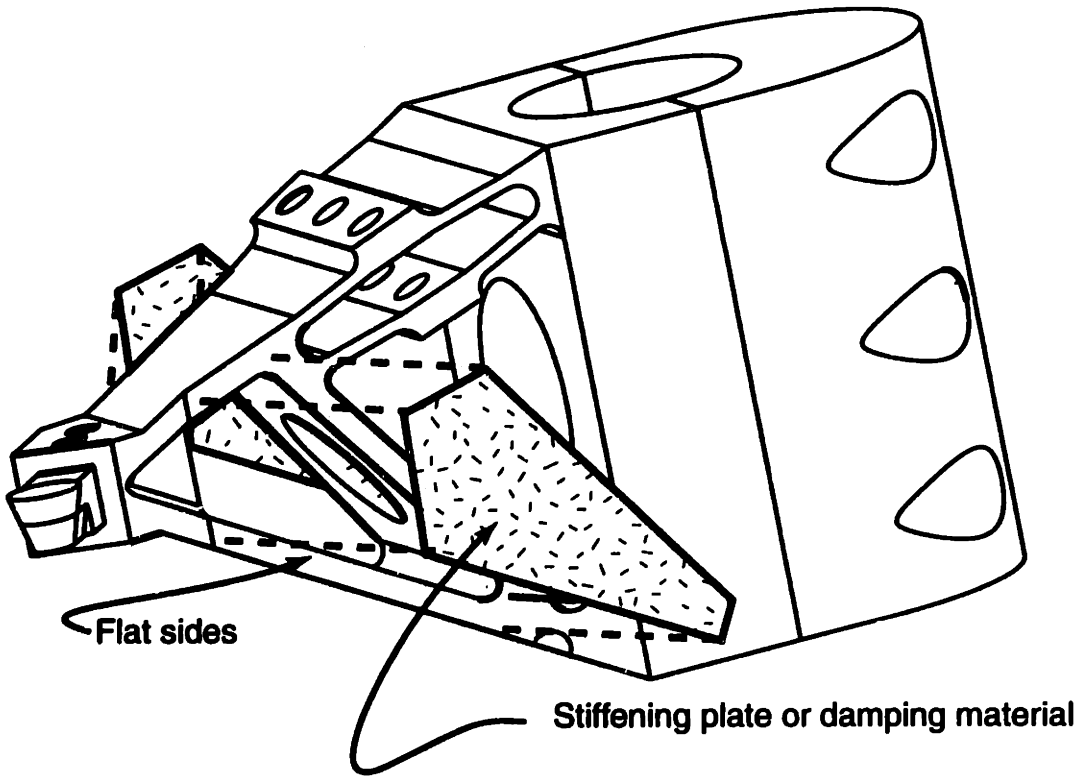

Figure 7-15: Stiffening plates or structural damping may be added to the flat sides of the toolarm.

significant amount of inertia, while adding little to the stiffness of the tool. Removing this material reduced the rotational inertia by $\sim 10\%$. Unfortunately, manufacturing such a hole is difficult with the EDM process, since it is not a completely planar profile. It thus requires a 4-axis wire EDM, which allows the wire to be angled to form tapered walls. The final inertia of the arm reduced to 310 kg-mm^2, with an estimated stiffness of $56\frac{N}{\mu m}$ at the end of the arm, loaded vertically and neglecting any stiffness added from the tool shank. The drawings used to manufacture the arm are found in Appendix A.

7.3.4 Modal Analysis

A modal analysis of the complete three dimensional model was conducted in Pro/MECHANICA. The model consisted of the toolarm fixed in space at the shaft interface. Several holes were omitted from the arm in order to simplify the meshing of the part; this will lead to a stiffer structure. The first mode of resonance was found to occur at 6.5 kHz,

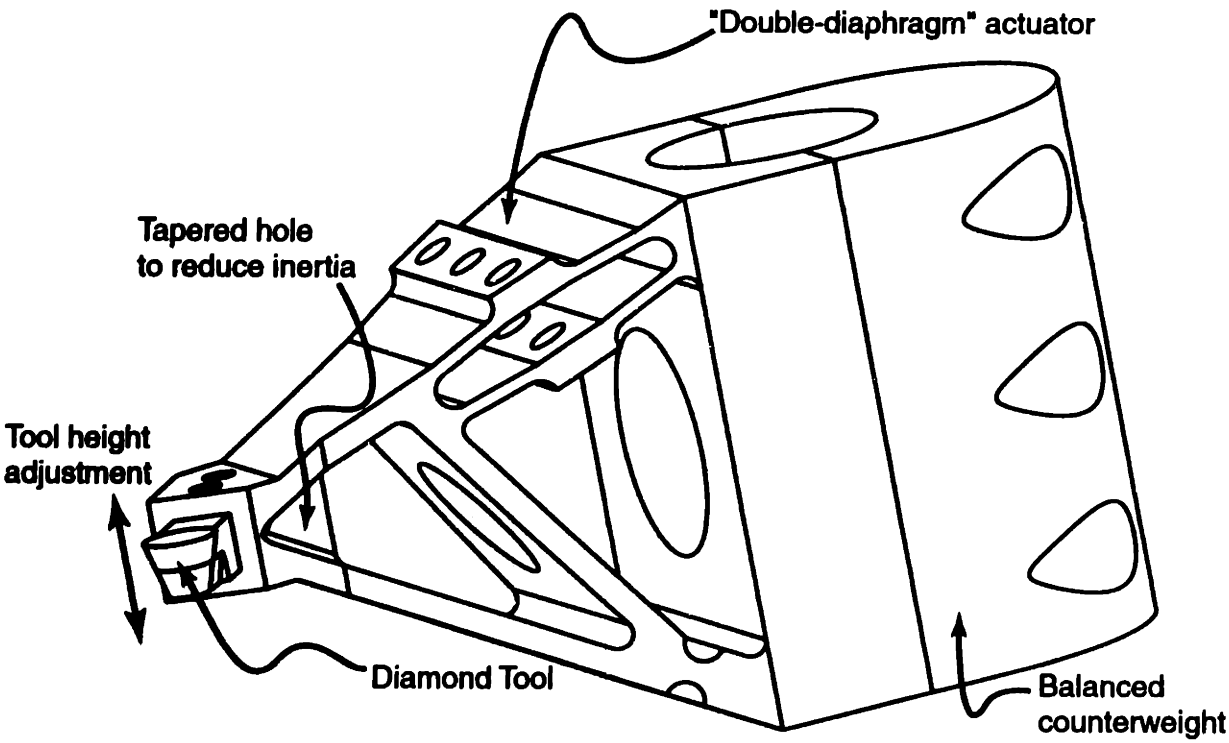

Figure 7-16: Toolarm has tapered hole to reduce inertia.

which included the oscillation of the diaphragms. This value was much better than expected, and leads to the suspicion of modeling errors. This model is certainly in error for the final mounted configuration, because the presence of the tool was neglected. This would lower the frequency due to additional mass, with no significant increase in stiffness. For the tested model, however, designing for high static stiffness and low inertia also produced a structure with this high dynamic stiffness. These results were considered encouraging enough that, when time constraints were considered, no additional analysis was performed. If the structure had revealed an unacceptable low resonance, steps could have been taken to improve the performance. The point of maximum deflection in the mode shape would need to be constrained, either by increasing the thickness of the support beams, or preferably by adding an additional "truss" to this point. This treatment would ignore the effects of increasing the mass, however, so iteration would likely be necessary to achieve the desired performance. It does not seem likely that the dynamic stiffness could be improved by lowering the mass, since the structural mass had been reduced as much as possible to lower iner-

tia. In any case, futher attempts should start with an even more basic model and "build-up" to the final arm in order to provide better insight into the presence of any modeling errors.

7.3.5 Counterweight

It is essential that the toolarm be driven through its center of mass, to prevent linear accelerative disturbance forces from being transferred to the support structure from RFTS motion. If this requirement is met, only rotational torques will be transmitted to the structure, along with linear forces from the cutting, which are impossible to eliminate. As discussed in Section 1.3, the rotational torques, unlike linear forces, will cause very little vibration due to the much larger rotational inertia of the support structure. The clamp which secures the toolarm to the toolshaft should then also function as a counterweight, moving the center of mass to the center of rotation.

It is important to realize that the center of mass can be moved without doubling the inertia of the arm. The counterweight can place more mass at a smaller radius, moving the center of mass the same amount as a small mass at a large radius, but with lower inertia. This is due to the radius squared effect in the calculation of the inertia. Since the counterweight is solid, it can place much more mass at smaller radii. The optimal radius on the back of the counterweight was established iteratively, using the Pro/ENGINEER solid modeling software. This software can easily determine the center of mass of the toolarm assembly. The radius on the back of the counterweight was simply adjusted until the axis of rotation and center of mass coincided. A full constrained optimization problem could likely improve upon the amount of added inertia while maintaining the center of mass, but preliminary work indicated such a benefit would be small, while adding to the manufacturing difficulty. This is primarily due to the constraint of being forced to clamp around the shaft; if free to simply chose the optimum balancing shape for the toolarm, greater improvement could be realized.

The clamp added another 223 kg-mm^2 of inertia to the toolarm, for a final rotational inertia of 580 kg-mm^2, including the tool.

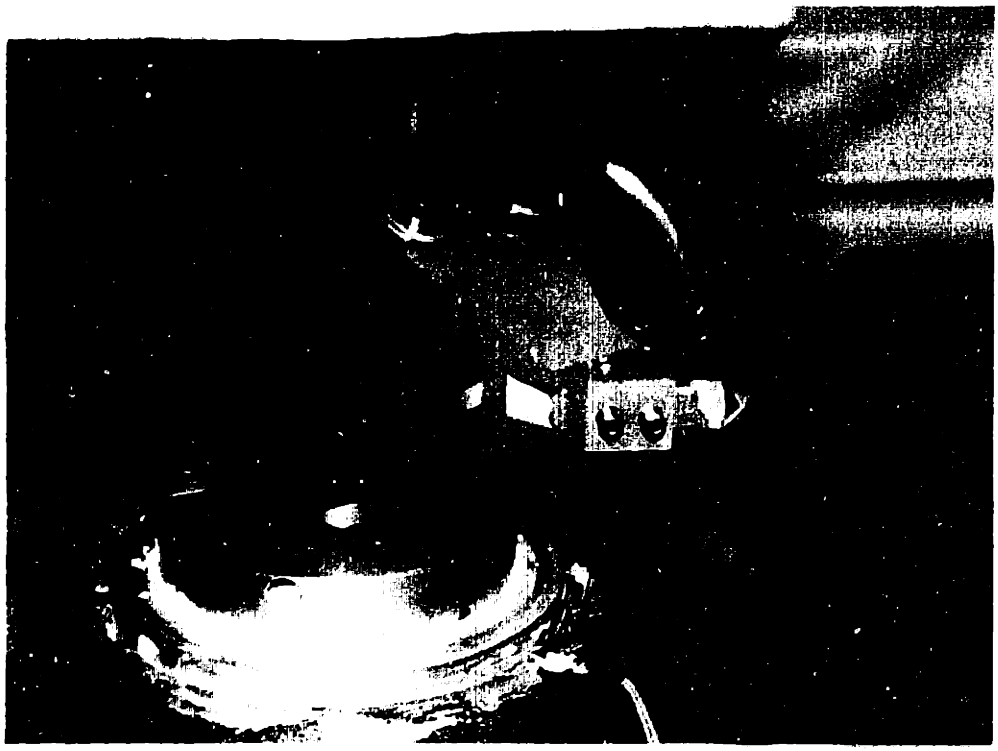

Figure 7-17: Final manufactured toolarm.

7.3.6 Experimental Results

The cost of production of this toolarm was high, with estimates ranging up to $4000. The lowest estimate was $1000, but this shop did not have the capability of manufacturing the tapered hole. Fortunately, DEKA Research & Development graciously offered to produce the tapered-hole arm for free, and we are thankful for their generosity. The Wire-EDM machined arm they produced is pictured in Figure 7-17. To guard against unforseen manufacturing problems, or an accident during testing, an order was sent to another shop for a second arm. The lowest-cost vendor was selected. As they did not have the ability to produce a tapered hole, only a straight through design, the counterweight was redesigned to compensate for the added mass. This design increased the rotational inertia by more than 10%, to 646 kg-mm^2.

Once the manufactured toolarm arrived at MIT, some testing was performed to examine how the finished product compared with the computer simulations. The arm was bolted to an aluminum plate, which was then bolted to the top of an optical table, in order to enable stiffness testing to be performed. This was done by simply

measuring deflection due to applied weights. However, the tests did not work as well as expected. There appeared to be some unknown sources of hysteresis and compliance in the test setup. The deflections did not completely reverse after the loading was removed, and the measured stiffness (44.5 N/mm) came only within 20% of the nearest estimate from the finite element analysis of the toolarm, and may be in error by as much as 50%. (This is due to the slope at the tip of the toolarm. Stiffness will vary depending on exactly where the measurement is taken). This is in sharp contrast to the tests on the prototype unit, which agreed with the computational results up to the limit of the resolution of the instruments. Since the toolarm needed to be pressed into service on the machine, further stiffness tests were not conducted with this setup, and it is believed they were in error.

The torsional resonance of the machine with the toolarm installed was found to be 870 Hz. The agreement with the theoretical models is quite good and allows a high bandwidth control system to be implemented. See Ludwick[12] for details of the control system implementation.

The fine height adjustment was tested on the optical bench and verified with a Starrett electronic indicator with 1 μm resolution. The adjustment was verified to work well to ± 25 μm. Since this particular arm was not hardened to the desired specification (10 Rockwell C vs. the 30 Rockwell C design), larger adjustments would cause some yielding of the material. However, even if hardened, additional travel would be difficult to obtain due to the large actuating forces necessary from the screws.

Coarse adjustment of the toolarm height was provided by a $\frac{1}{4}$-20 adjustment screw clamped to the side of the toolarm. With the clamping bolts loosened, this permits the height of the whole toolarm to be adjusted along the tool mounting shaft. This worked much better than was expected. The good finish of the EDM on the bore of the toolarm, along with the finish on the shaft, allowed the arm to be moved with the resolution of the screw, $\sim$ 5 μm. Since a pitch error in the toolarm of 0.005° can causes errors greater than 5 μm in the tool height, it had been thought that tightening the clamping screws could cause significant errors after the height had

been set. However, the linear bearing characteristics of the arm on the shaft proved to be very good, allowing the tool height to be set to within 5 μm of what was set with the screw. Unfortunately, this is not a desirable means to set the tool height, since loosening the clamping screws allows the toolarm to rotate on the shaft as well, *losing the rotational index of the arm and forcing recalibration.*

The tool height was set on the arm by cutting machinable wax flats. The size of the hump in the center of the flat, due to tool height error, was measured to be 70 μm in diameter with a 30× optical microscope. Accordingly, the toolarm was adjusted down 35 μm with the coarse adjustment. After this adjustment, the center hump was not visible with the microscope, which should be able to allow measurement down to the 5 μm range. Deliberate misadjustment of the fine tool height, however, produced no noticeable hump in the center of the part with the 30× microscope. However, the finish of the PCD tooling made the center defect difficult to distinguish. At the time of this writing, preliminary tests with single crystal diamond tooling indicate that improved surface finish may reveal a center defect more easily, and enable more precise adjustment of the center height with the fine adjustment. Figure 7-18 illustrates the center defect in a single crystal cut part. A better assessment needs to be made of the exact requirements of the tool height in this machine, in light of the needs of the post polishing process. Currently, it appears that a height adjustment this fine may not be necessary, and a tradeoff of travel range at the expense of resolution may be appropriate.

7.3.7 "Double-Ended" Toolarm

Once testing began with single crystal tooling, the advantages of having an automatic tool changer became obvious. Single crystal diamond tools are primarily finishing tools, not designed for heavy cutting. Thus we were reluctant to test the tools without forming a good surface first. However, swapping tools would not allow calibration to be maintained. If the tools could be changed automatically while maintaining calibration, this would provide an enormous advantage.

The RFTS lends itself naturally to having multiple tools installed simultaneously.

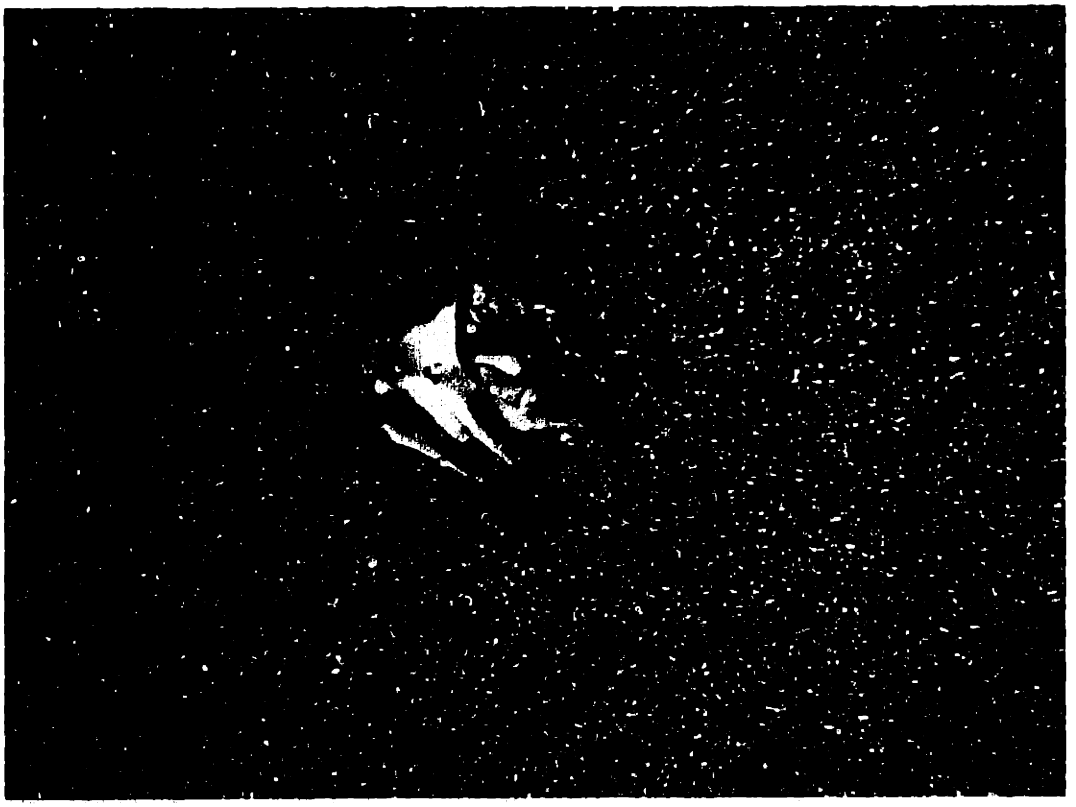

Figure 7-18: Center defect in lens cut with single crystal tooling. This is actually a recess, likely formed after the defect was fractured off. Defect is $\sim$ 125 μm in diameter.

Since only a portion of the rotational stroke is used, and arms can swing without interference through a full 360° rotation within the support casting, it is possible to mount other tools on different arms facing away from the arm that is in use. When a different tool is desired, the shaft simply rotates to bring that tool into action.

Since we already had two toolarms, a "quick and dirty" approach to the tool changer was implemented. The two arms were bolted back-to-back on the shaft, so that two tools could be mounted 180° to each other. Unfortunately, the arms were not originally designed to meet this functional requirement; the clamping bolt holes on both arm were threaded, and there was no convenient way to make the arms bolt directly to each other.

Instead, a seperate clamp was fabricated to hold the two arms together. Since the clamp only needs to provide force, not stiffness (which is provided by the toolshaft), it can easily be fabricated from aluminum, which minimizes the added inertia. Some inertia increase is still noticed with the two arm configuration, however, since the inertia minimizing clamps of Section 7.3.5 are not used. In addition, the arms are slightly out of balance, since one arm contains the tapered hole, while the other does not. This configuration is illustrated in Figure 7-19.

The "double-ended" toolarm is currently being employed on the machine to use single crystal tools. One arm holds a PCD roughing tool, while the other holds a single crystal finishing tool. The torsional resonance has been lowered to approximately 770 Hz by the added inertia, which is still high for mechanical system. Adjustment of the tool height is more complicated, since it is difficult to adjust the coarse differential height between the two arms. Fortunately, only the tool height of the finishing tool is critical.

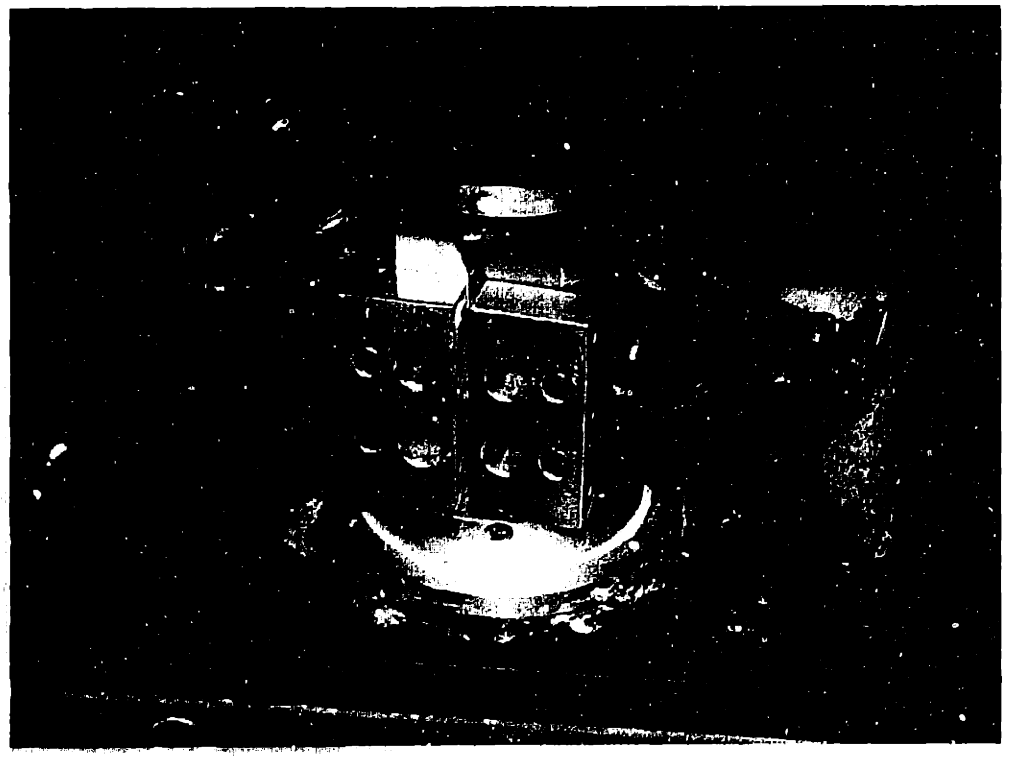

Figure 7-19: Doubled-ended toolarm installed on machine. Note aluminum clamp.

Chapter 8

Conclusions and Recommendations for Future Work

This thesis focuses on the design, development, and integration of several components into a rotary fast tool servo (RFTS) system. The success of these elements is essential in producing a functional machine. The importance of the toolarm and feedback sensor are obvious, but even lowly elements like bearing seals are needed. The elements have all performed well and contributed to allowing this diamond turning machine to achieve unprecedented performance. Not only is it of much higher precision and accuracy than conventional eyeglass manufacturing machines, it also moves a cutting tool on 50-g, 1 cm peak-to-peak toolpaths! This combination of accuracy, acceleration, and large amplitude movement is unequaled.

The selection and integration of the MicroE sensor into the RFTS control system was very successful. A new sensor was absolutely critical to achieve the design goals of the machine, and the MicroE sensor was the best choice. The striking improvement in performance after the adoption of the new sensor illustrates how limited the machine was by the previous analog sensor. The MicroE encoder line seems to be one of the best choices for high resolution sensors available and has few equals in the market. For those used to conventional optical encoders, it is truly an experience to be able to rotate the shaft one revolution by hand, and see the position increment to 63,000,000!

I learned valuable lessons in the construction of the interface electronics. Even

though the concept and design of the circuit were correct, the implementation led to unmodeled behavior. The abstraction of the design process away from the implementation is supposed to be one benefit of the digital interface, but the problems encountered here show there is no substitute for proper circuit construction techniques, where the analog elements are considered.

For a production machine, further work could be undertaken in conjunction with MicroE to ease the alignment procedure of the encoder, with accurately machined hubs carrying the gratings, so that they need only be pressed over and clamped to the ends of the shafts. If done to a sufficient level of precision, this could increase the accuracy of the encoder. Another possibility is the use of two sensors, where the outputs are averaged for better accuracy. Such electronics are already available from MicroE. MicroE has also switched to a new line of standard gratings. Unfortunately, the grating used here is not in this new line, nor are there any 20 μm pitch gratings of reasonable size, using the selection procedure developed in Chapter 2. A new DSP Interpolator board, however, has improved electronics, with faster 350,000 $\frac{cycles}{sec}$ counting speed, which may enable a smaller diameter 5 μm grating to meet the requirements. Smaller diameter gratings will require some increased design effort to place the sensor, since the closer spacing will cause interference with the shaft.

The bearing seal design is one of the more straightforward pieces of this work, yet it also shows very interesting future potential. I was motivated in my choice of the labyrinth seal design by the need for a split design which could be coupled about the prototype shaft, but production machines would likely dispense with this requirement. The labyrinth remains the best choice, however, due to its damping capability. Rolling element bearings have traditionally suffered from the lack of damping they offer at their interface. Adding viscous fluid to the labyrinth seal appears to be an excellent way to obtain some of the damping offered by a hydrostatic bearing, but eliminates the expense and difficulty of a hydraulic pump system. Future work could attempt to make this effect much more significant in the design, by increasing the number and working diameter of the ridges, and by using improved manufacturing to decrease the gap size.

Seal performance could be further improved by switching to a straight viscous fluid, as opposed to the grease approximation. The thickeners present in the grease may prevent the full damping potential from being realized, as not all sections of the wall may be in contact with the grease and full flow may not be developed. The cleanliness and integrity of the seal may then be enhanced by flowing the fluid through the seal, into gutters, with a small, inexpensive pump. The combination of rolling element bearings and "damping seals" may offer better damping at a far lower cost than a complete fluid bearing system. This idea not only could greatly aid efforts to control the RFTS at high bandwidths by significantly reducing the torsional resonance, but also has broader applicability to other rotary devices which benefit from damping.

This thesis emphasizes proper process during the design of the toolarm. The conflicting requirements of the machine led to careful consideration of the functional requirements early in the design process. In fact, this work illustrates the success of the process versus an unstructured approach. For the initial set of functional requirements, the final design performed very well, meeting all of the requirements at least adequately. Once an additional functional requirement was added to the machine, to hold a roughing and a finishing tool in the "double-ended" design, problems arose since this was not considered early in the process. As a result, the performance of the final double-ended toolarm was less than ideal from an ease-of-use standpoint, but was sufficient to show the promise of the multi-tool capability of our new RFTS.

The novel actuator developed here led to much of the success of the toolarm, but also introduced the limitations to be addressed in future work. The "double-diaphragm" design produces exceptionally high resolution movement, while retaining the low inertia and high stiffness required by a RFTS toolarm. Compared with the previous, nonadjustable toolarm used on the machine, only a slight penalty was paid in terms of a lower torsional resonance, but stiffness was greatly increased. The change to shanked tooling added greatly to the flexibility of the machine and also added more support to the cutting tool. These increases in stiffness likely contributed to the noticeable improvement in surface finish after installation of the toolarm. Un-

fortunately, directly comparable profilometer results are not yet available to quantify the improvement.

The "double-diaphragm" actuator is chiefly limited by its small range of adjustment. Given the original functional requirements, the "slide-on-shaft" coarse adjust coupled with the fine adjustment proved functional for the single arm. However, the ease of the adjustment procedure could be greatly enhanced with a larger range of travel. This lack of range becomes more critical in the "double-ended" design. Simply bolting the two arms back-to-back did not provide any provision for locating their height relative to each other. Attempting to adjust the relative heights of the two toolarms was very difficult, since not only was there was a strong tendency for the two to slide together on the shaft, but the relative heights also needed to be within the $\pm 20\mu$m adjustment of the fine actuator for both tools to be on center. A larger range of travel would enable this to be set much more roughly.

By documenting the design process thoroughly, this thesis contains all the "building blocks" necessary to develop a new, doubled-ended arm with greater functionality. In fact, the design techniques presented in Chapter 6 are broadly applicable to the design of high precision actuation systems. The tapered beam theory in Section 6.4 should prove particularly useful in optimizing the stiffness and bending requirements of an arm suitable for production by casting methods. An automated arm adjustment system, using a piezoclectric actuator, may represent the best solution for a production machine since operator skill is negligible. Such a device would require a feedback sensor to overcome the hysteresis in the actuator under changing loads, which would add to the cost of the machine. Some analysis would be required to see if that is an acceptable tradeoff in the market.

In any case, our machine has demonstrated unprecedented levels of performance. The RFTS can follow high-acceleration 50 g toolpaths while cutting toric lenses. The design goals for form error and surface finish have been realized, as we have successfully cut lenses with a form error of 1 μm in 10 mm, and surface finishes of less than 0.2 μm using PCD tooling and 0.1 μm using single-crystal tooling. The components designed in this thesis contributed to this success.

Appendix A

CAD Drawings

These are the drawings used to create the final toolarm.

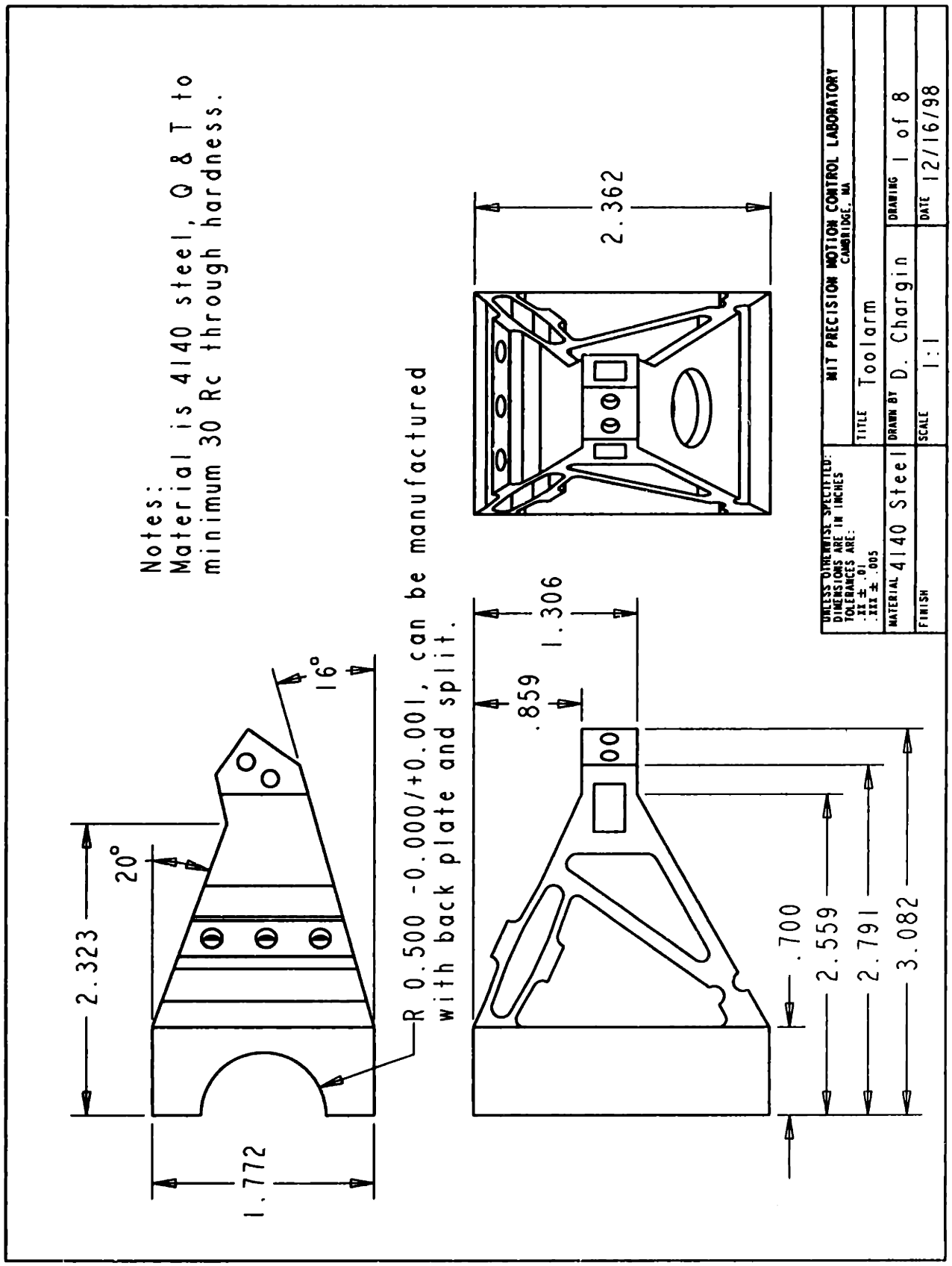
Notes:
Material is 4140 steel, Q & T to
minimum 30 Rc through hardness.
R 0.500 -0.000/+0.001, can be manufactured
with back plate and split.
2.362
1.306
.859
16°
20°
2.323
1.772
.700
2.559
2.791
3.082
UNLESS OTHERWISE SPECIFIED:
DIMENSIONS ARE IN INCHES
TOLERANCES ARE:
.XX ± .01
.XXX ± .005
MIT PRECISION MOTION CONTROL LABORATORY
CAMBRIDGE, MA
TITLE Toolarm
MATERIAL 4140 Steel
DRAWN BY D. Chargin
DRAWING 1 of 8
SCALE 1:1
DATE 12/16/98
FINISH

Figure A-1:

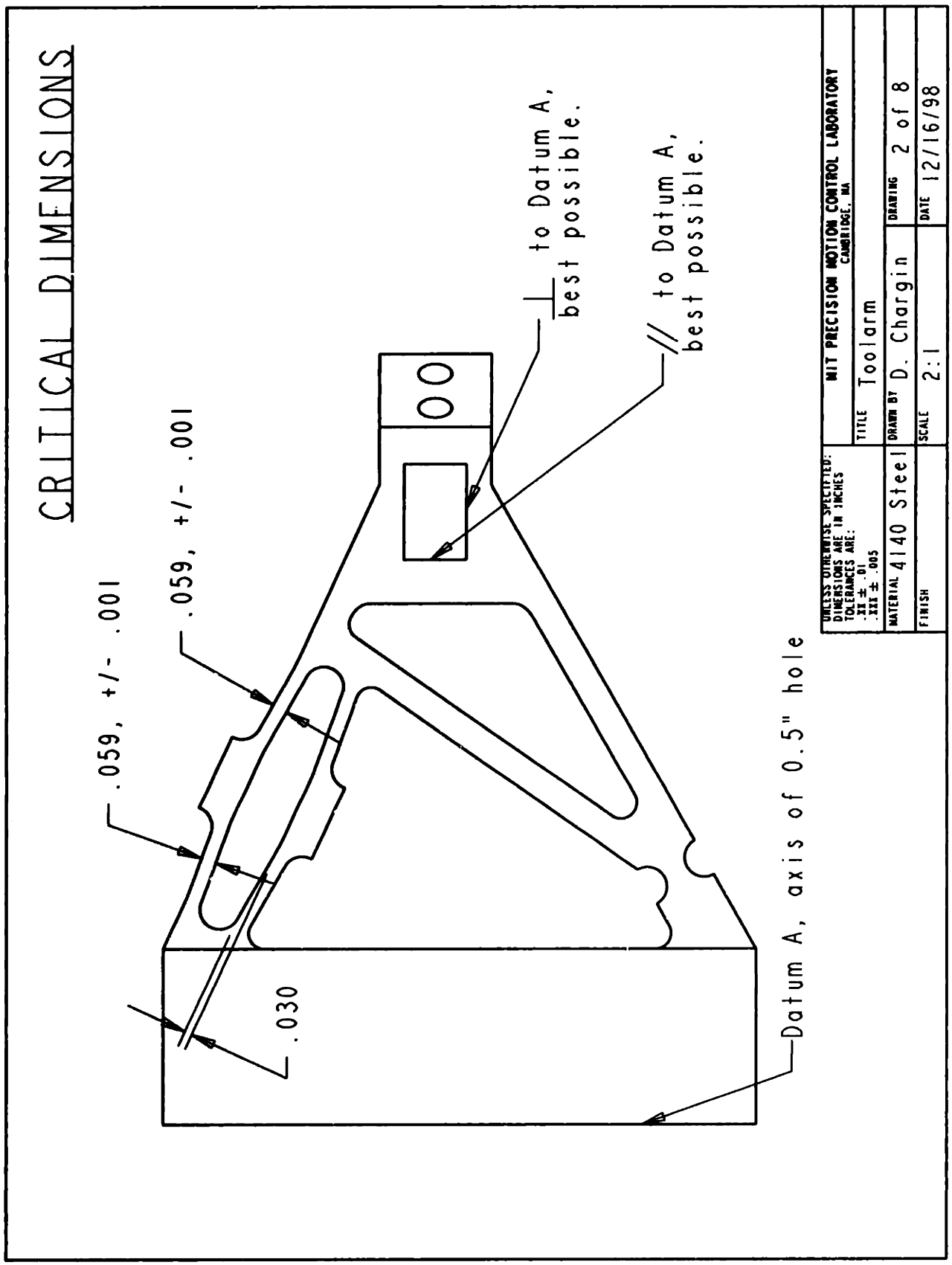
CRITICAL DIMENSIONS
.059, +/- .001
.059, +/- .001
.030
Datum A, axis of 0.5" hole
⊥ to Datum A, best possible.
// to Datum A, best possible.
UNLESS OTHERWISE SPECIFIED: DIMENSIONS ARE IN INCHES TOLERANCES ARE: .XX ± .01 .XXX ± .005
MIT PRECISION MOTION CONTROL LABORATORY CAMBRIDGE, MA
TITLE Toolarm
MATERIAL 4140 Steel
DRAWN BY D. Chargin
DRAWING 2 of 8
FINISH
SCALE 2:1
DATE 12/16/98

Figure A-2:

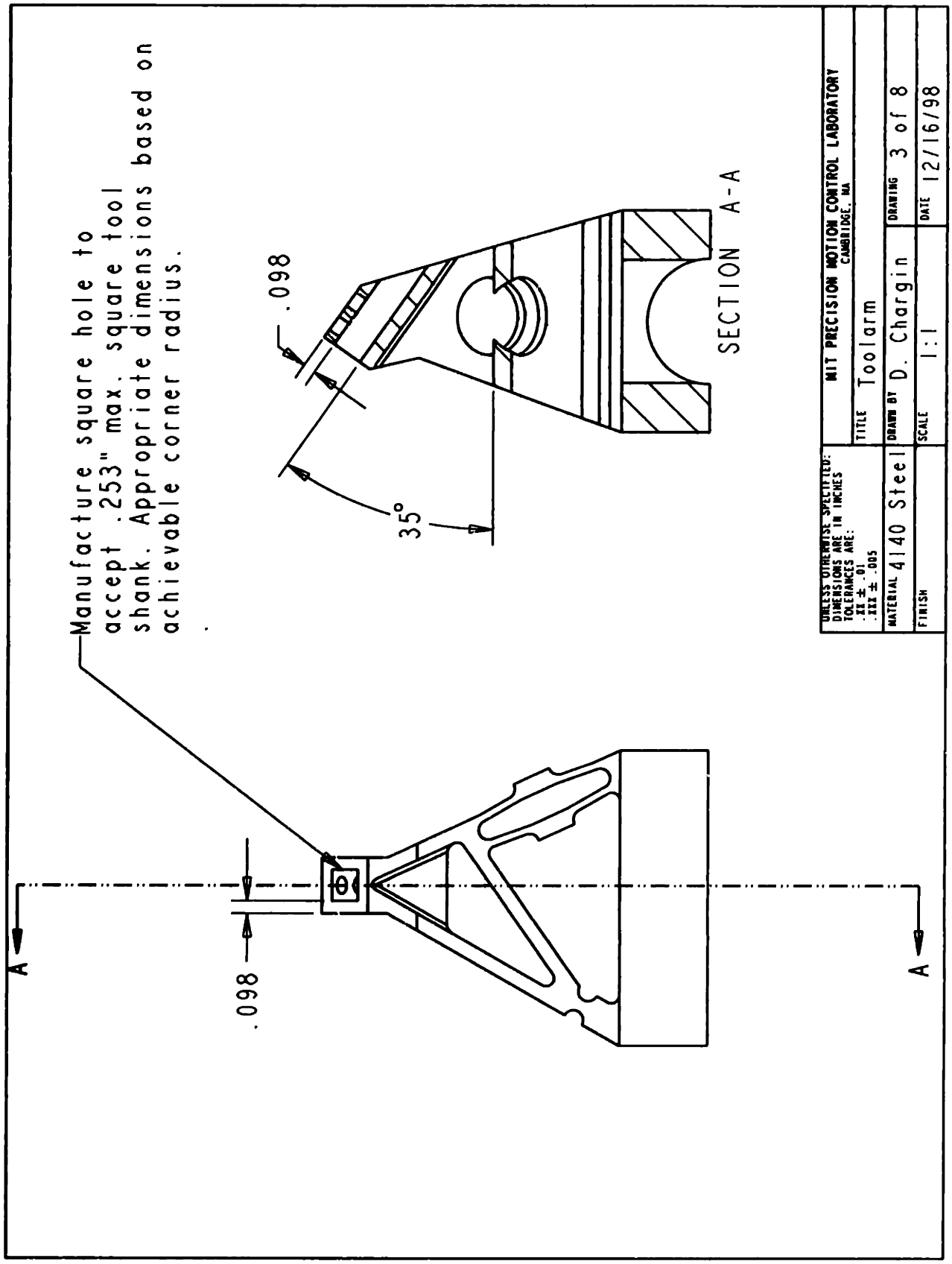
Manufacture square hole to accept .253" max. square tool shank. Appropriate dimensions based on achievable corner radius.
.098
35°
SECTION A-A
.098
A
A
UNLESS OTHERWISE SPECIFIED: DIMENSIONS ARE IN INCHES TOLERANCES ARE: .XX ± .01 .XXX ± .005
MIT PRECISION MOTION CONTROL LABORATORY CAMBRIDGE, MA
TITLE Toolarm
MATERIAL 4140 Steel
DRAWN BY D. Chargin
DRAWING 3 of 8
FINISH
SCALE 1:1
DATE 12/16/98

Figure A-3:

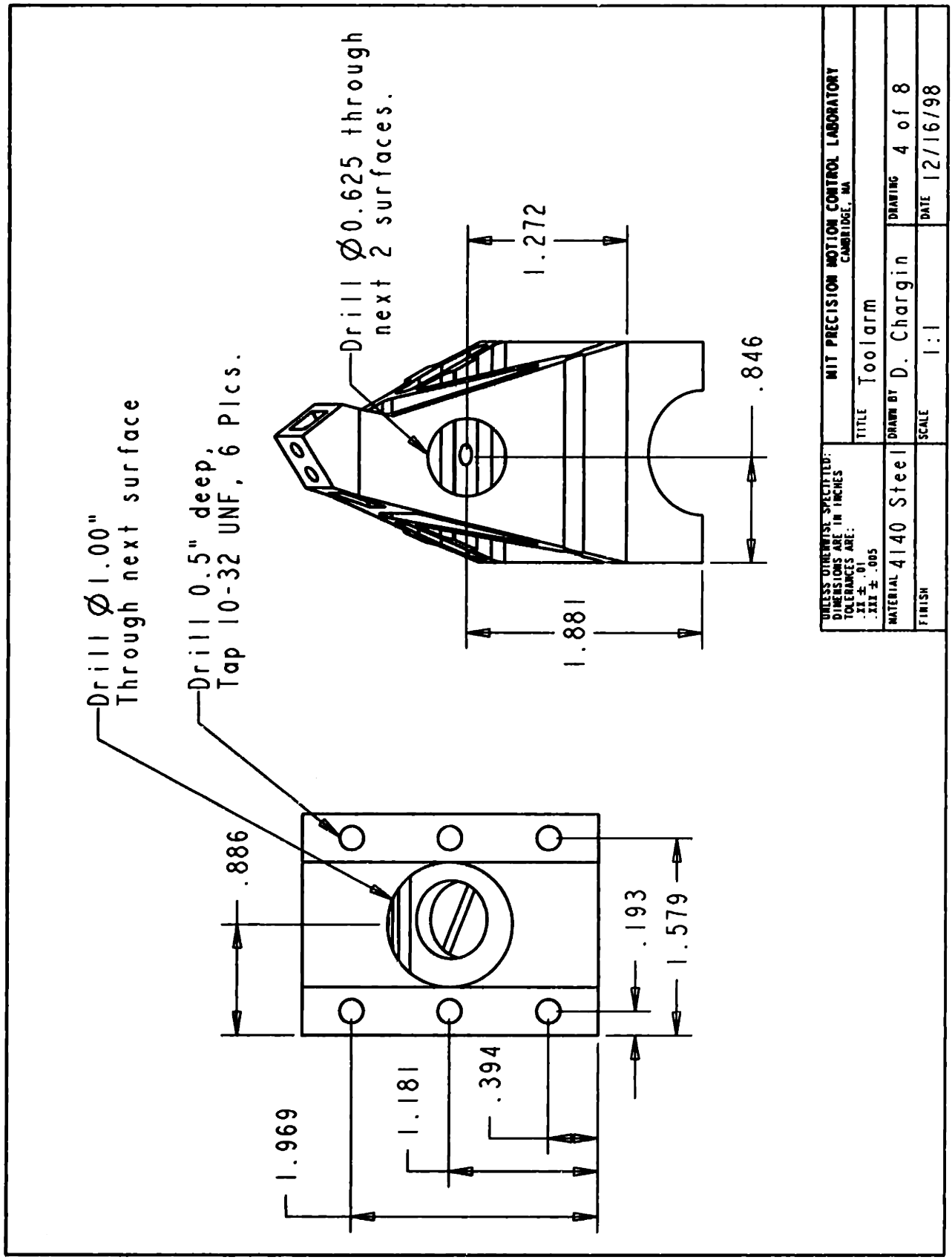
Drill Ø1.00"
Through next surface
Drill 0.5" deep,
Tap 10-32 UNF, 6 Plcs.
Drill Ø0.625 through
next 2 surfaces.
1.272
.846
1.881
.886
.193
1.579
1.969
1.181
.394
MIT PRECISION MOTION CONTROL LABORATORY
CAMBRIDGE, MA
TITLE Toolarm
DRAWN BY D. Chargin
DRAWING 4 of 8
MATERIAL 4140 Steel
SCALE 1:1
DATE 12/16/98
FINISH
UNLESS OTHERWISE SPECIFIED:
DIMENSIONS ARE IN INCHES
TOLERANCES ARE:
.XX ± .01
.XXX ± .005

Figure A-4:

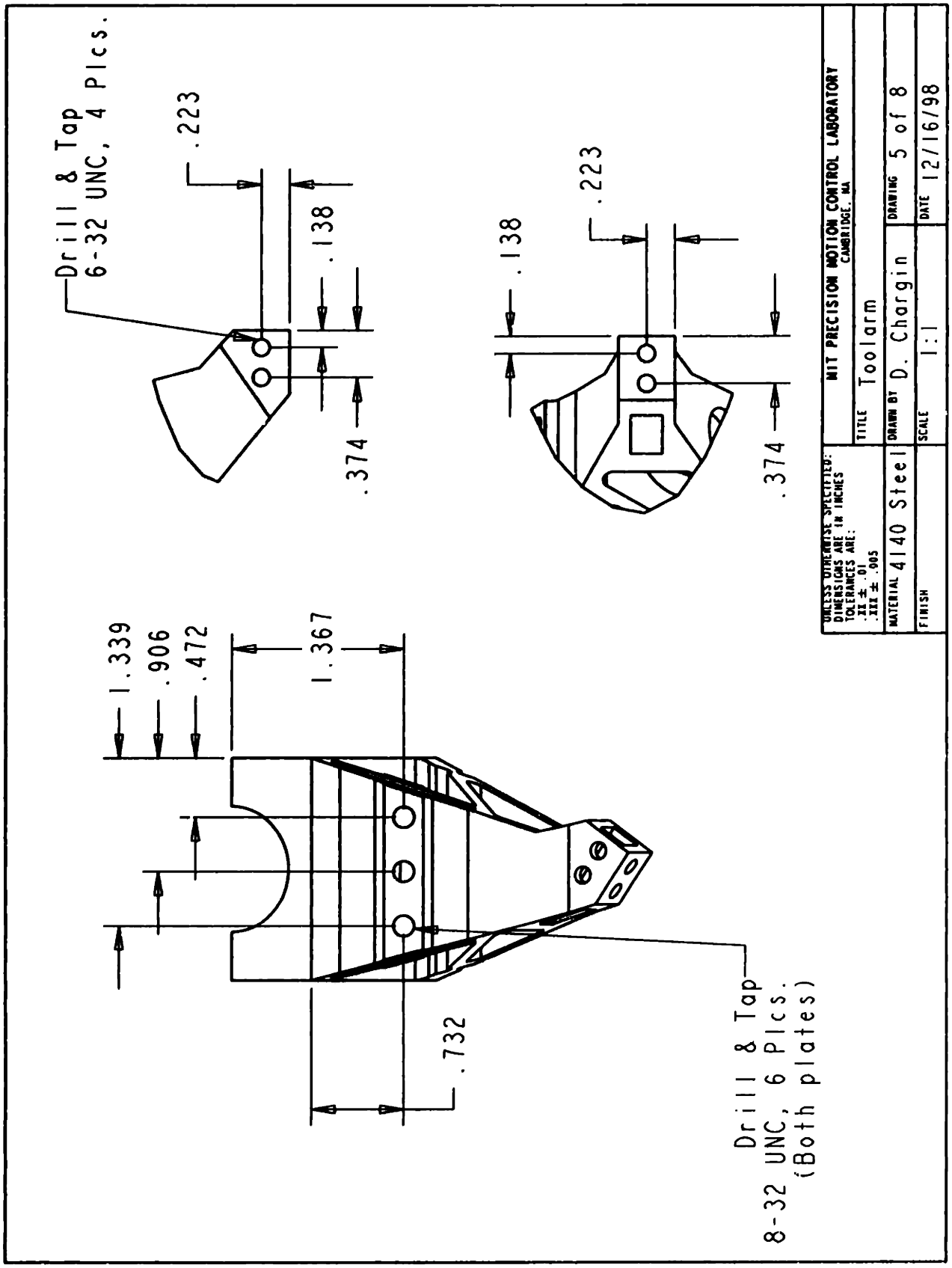
Drill & Tap
6-32 UNC, 4 Plcs.
.223
.138
.374
.223
.138
.374
1.339
.906
.472
1.367
.732
Drill & Tap
8-32 UNC, 6 Plcs.
(Both plates)
UNLESS OTHERWISE SPECIFIED:
DIMENSIONS ARE IN INCHES
TOLERANCES ARE:
.XX ± .01
.XXX ± .005
MIT PRECISION MOTION CONTROL LABORATORY
CAMBRIDGE, MA
TITLE Toolarm
MATERIAL 4140 Steel
DRAWN BY D. Chargin
DRAWING 5 of 8
FINISH
SCALE 1:1
DATE 12/16/98

Figure A-5:

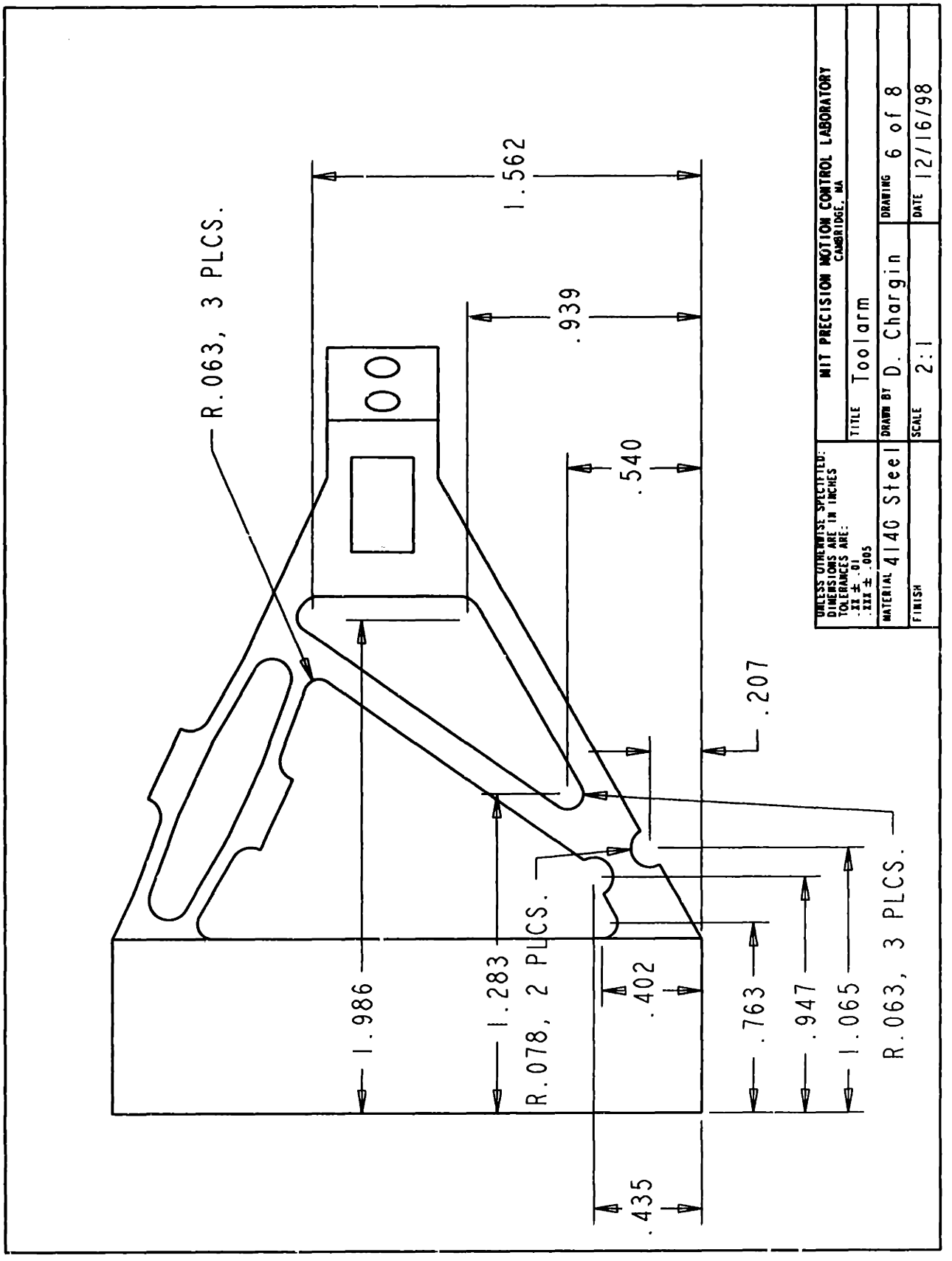
R.063, 3 PLCS.
1.562
.939
.540
.207
1.986
1.283
R.078, 2 PLCS.
.402
.763
.947
1.065
R.063, 3 PLCS.
.435
UNLESS OTHERWISE SPECIFIED:
DIMENSIONS ARE IN INCHES
TOLERANCES ARE:
.XX ± .01
.XXX ± .005
MIT PRECISION MOTION CONTROL LABORATORY
CAMBRIDGE, MA
TITLE Toolarm
MATERIAL 4140 Steel
DRAWN BY D. Chargin
DRAWING 6 of 8
FINISH
SCALE 2:1
DATE 12/16/98

Figure A-6:

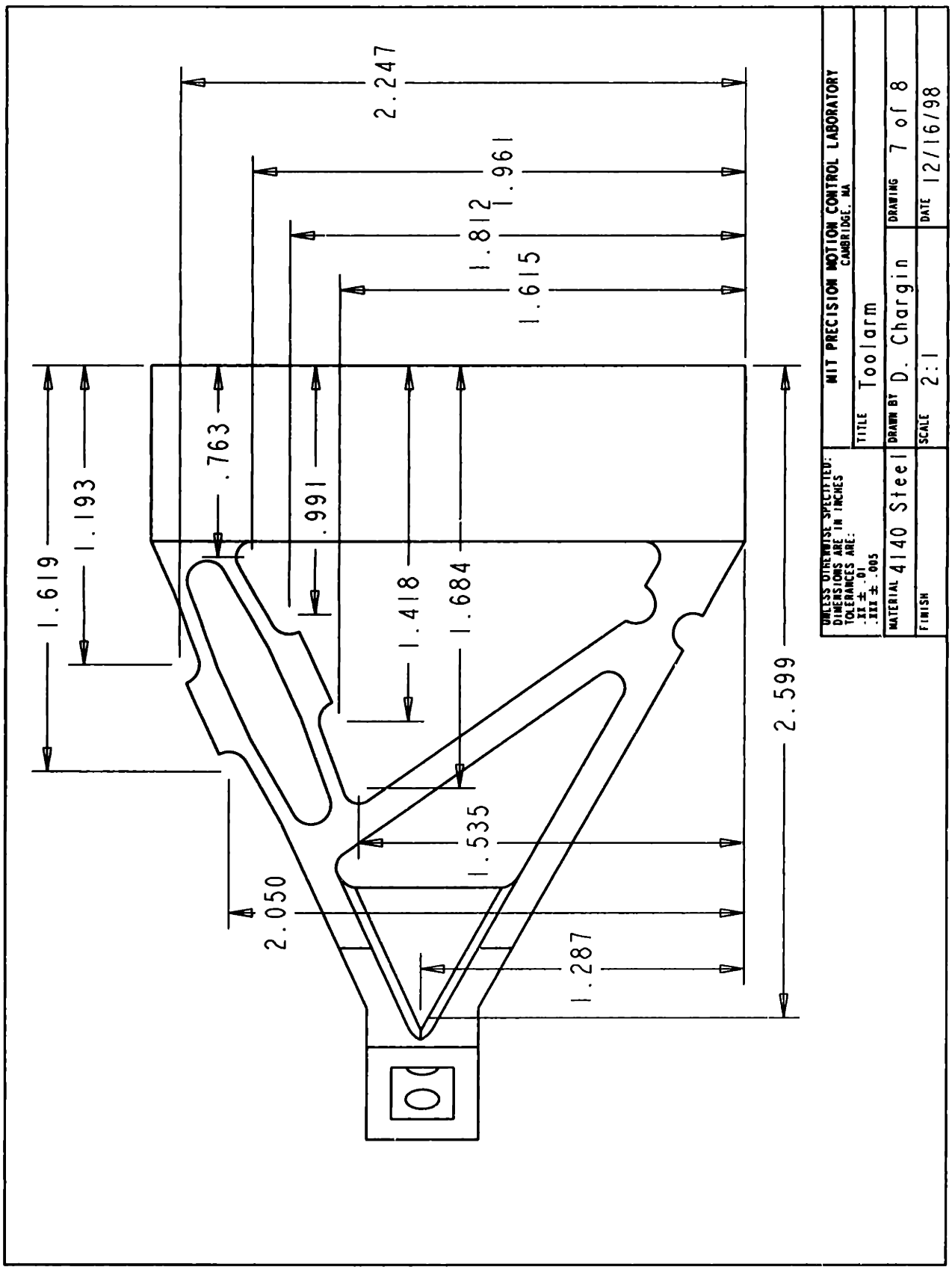
2.247
1.961
1.812
1.615
.763
.991
1.619
1.193
1.418
1.684
2.599
1.535
2.050
1.287
MIT PRECISION MOTION CONTROL LABORATORY
CAMBRIDGE, MA
UNLESS OTHERWISE SPECIFIED:
DIMENSIONS ARE IN INCHES
TOLERANCES ARE:
.XX ± .01
.XXX ± .005
TITLE Toolarm
MATERIAL 4140 Steel
DRAWN BY D. Chargin
DRAWING 7 of 8
FINISH
SCALE 2:1
DATE 12/16/98

Figure A-7:

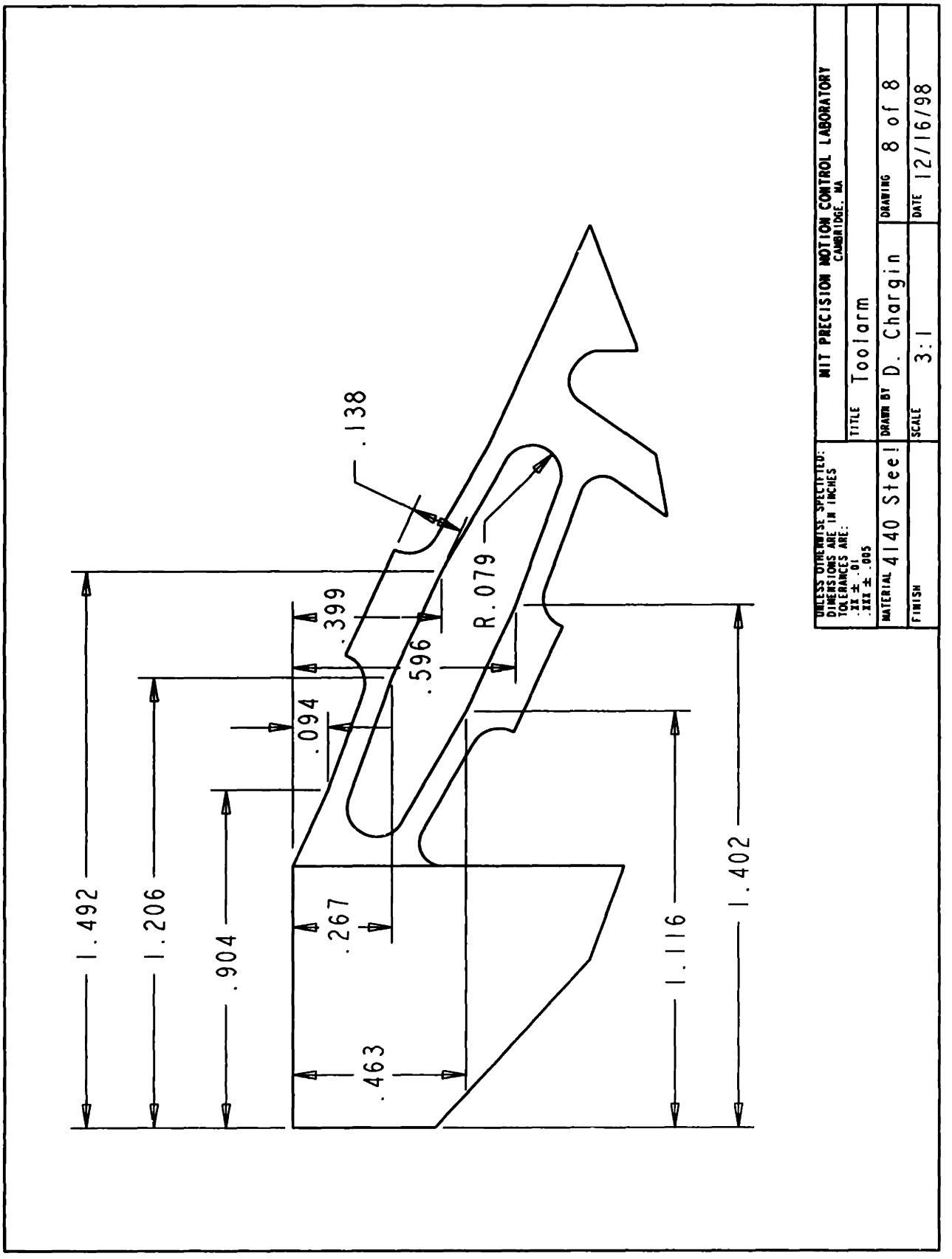
.138
R.079
.399
.596
.094
.267
.463
1.492
1.206
.904
1.116
1.402
UNLESS OTHERWISE SPECIFIED:
DIMENSIONS ARE IN INCHES
TOLERANCES ARE:
.XX ± .01
.XXX ± .005
MIT PRECISION MOTION CONTROL LABORATORY
CAMBRIDGE, MA
TITLE Toolarm
MATERIAL 4140 Steel
DRAWN BY D. Chargin
DRAWING 8 of 8
FINISH
SCALE 3:1
DATE 12/16/98

Figure A-8:

Bibliography

[1] Aerotech, Inc. 101 Zeta Drive, Pittsburgh, PA. 15238 Tel: 412-963-7470, http://www.aerotechinc.com.

[2] Klaus-Juergen Bathe. *Finite Element Procedures.* Prentice Hall, New Jersey, 1996.

[3] James B. Bryan. The design and construction of an 84-inch diameter diamond turning machine - a case study, October 1995. Annual Meeting of ASPE Tutorial Notes.

[4] ASM International Handbook Committee. *Properties and Selection: Irons, Steels and High-Performance Alloys*, volume 1 of *Metals Handbook.* ASM International, Materials Park, Ohio, 10th ed. edition, 1990.

[5] Contour Fine Tooling, Inc. 143 Jaffrey Road, Marlborough, NH 03455 Tel: 1-603-876-4908, http://www.contour-diamonds.com.

[6] Devitt Machinery Co., Suite G, 4009 Market St., Aston, PA 19014 Tel: 610-494-2900.

[7] DSP Research, Inc. 1095 E. Duane Ave., Ste. 203, Sunnyvale, CA 94086, Tel: 408-773-1042, http://www.dspr.com.

[8] EDN. Grounding...facts and fallacies. *EDN*, pages 69–74, January 20 1994.

[9] Institute for Astronomy. Gemini near infrared imager: Project overview. http://kupono.ifa.hawaii.edu/WEB/NIRI/CDR/mechanics.html.

[10] Gerber Coburn Optical, South Windsor, CT 06074 Tel: 1-800-843-1479, http://www.gerbercoburn.com.

[11] Paul Horowitz and Winfield Hill. *The Art of Electronics.* Cambridge University Press, New York, 2nd edition, 1989.

[12] Stephen Joseph Ludwick Jr. *A Rotary Fast Tool Servo for Diamond Turning of Asymmetric Optics.* Ph.D. Thesis,Department of Mechanical Engineering, Massachusetts Instituite of Technology, Cambridge, MA, 1999.

[13] Kistler Instrument Corporation, 75 John Glenn Drive, Amherst, NY 14228 Tel:716-691-5100, http://www.kistler.com.

[14] Krytox #240AB, E. I. du Pont de Nemours and Company, Tel: 800-424-7502.

[15] NSK Ltd. Nsk rolling bearings, 1989. Pr.No.A140A.

[16] Lucas Aerospace Power Transmission, 211 Seward Avenue, Utica, NY 13501 Tel:315-793-1200, http://www.lucasutica.com.

[17] David Chih-Yan Ma. Design and implementation of a rotary fast tool servo for a turning machine. S.M. Thesis, Department of Mechanical Engineering, Massachusetts Institute of Technology, Cambridge, MA, 1998.

[18] MicroE, Inc. 8 Erie Drive, Natick, MA 01760-1313, Tel: 508-903-5000, http://www.micro-e.com.

[19] Wayne R. Moore. *Foundations of Mechanial Accuracy.* The Moore Special Tool Company, Bridgeport, Connecticut, 1970.

[20] Motorola Semiconductor technical data, online at http://mot-sps.com.

[21] Samir Ali Nayfeh. *Design and Application of Damped Machine Elements.* Ph.D. Thesis,Department of Mechanical Engineering, Massachusetts Instituite of Technology, Cambridge, MA, 1998.

[22] New Focus, Inc., 2630 Walsh Avenue, Santa Clara, CA 95051 Tel:408-980-8088, http://www.newfocus.com.

[23] Newport Corporation, 1791 Deere Ave., Irvine, CA 92606 Tel:800-222-6440, http://www.newport.com.

[24] J.M. Paros and L. Weisbord. How to design flexure hinges. *Machine Design*, pages 151–156, November 15, 1965.

[25] Professional Instruments Co., 4601 Highway 7, Minneapolis, MN 55416, Tel: 612-933-1222.

[26] Thomas L. Saaty. *The Analytic Hierarchy Process.* McGraw-Hill, Inc., New York, 1980.

[27] Joseph E. Shigley and Charles R. Mischke. *Mechanical Engineering Design.* McGraw-Hill, Inc., New York, 5th edition, 1989.

[28] SKF. *SKF Bearing Maintenance Handbook.* Linde Information AB, Lerum, Sweden, 1991.

[29] Alexander H. Slocum. *Precision Machine Design.* Society of Manufacturing Engineers, Dearborn, Michigan, 1992.

[30] S.T. Smith and D.G. Chetwynd. *Foundations of Ultraprecision Mechanism Design*, volume 2 of *Developments in Nanotechnology.* Gordon and Breach Science Publishers, Canada, 1992.

[31] Jr. Stephen Joseph Ludwick. Modeling and control of a six degree of freedom magnetic / fluidic motion control stage. S.M. Thesis, Department of Mechanical Engineering, Massachusetts Institute of Technology, Cambridge, MA, 1996.

[32] Nam P. Suh. *The Principles of Design.* Oxford University Press, New York, 1990.

[33] Thorlabs, Inc., 435 Route 206 North, P.O. Box 366, Newton, NJ 07860 Tel:973-579-7227, http://www.thorlabs.com.

[34] Waterloo Maple, 57 Erb St. W., Waterloo, Ontario, N2L 6C2, Canada, Tel:519-747-2373, http://www.maplesoft.com.

[35] Warren D. Weinstein. Flexure-pivot bearings, part 1. *Machine Design*, pages 150–157, June 10, 1965.

[36] Warren D. Weinstein. Flexure-pivot bearings, part 2. *Machine Design*, pages 136–145, July 8, 1965.

[37] Frank M. White. *Fluid Mechanics.* McGraw-Hill, Inc., New York, 3rd. edition, 1994.

[38] Warren C. Young and Raymond J. Roark. *Roark's Formulas for Stress and Strain.* McGraw-Hill, Inc., New York, 6th edition, 1989.